Dissertation
submitted to the
Combined Faculty for the Natural Sciences and for Mathematics
of the Ruperto-Carola University of Heidelberg, Germany
for the degree of
Doctor of Natural Sciences

presented by
Martin Andreas Eibach
born in Waldbröl

Date of oral examination: 04.12.2013

High-precision mass measurements in the realm of the deformed shell closure N=152

Referees: Prof. Dr. Klaus Blaum
PD Dr. Yuri Litvinov

High-precision mass measurements in the realm of the deformed shell closure N=152:
The nuclear masses reflect the sum of all interactions inside a nucleus. Their precise knowledge can be used to benchmark nuclear mass models and to gain nuclear structure information. Penning-trap mass spectrometers have proven their potential to obtain lowest uncertainties. Uniquely located at a nuclear reactor, the double Penning-trap mass spectrometer TRIGA-TRAP is dedicated to measurements in the neutron-rich region. For a gain in sensitivity a non-destructive detection system for single ion mass measurements was adopted. This includes the implementation of a narrow band-pass filter tuned to the heavy ion cyclotron frequency as well as a cryogenic low-noise amplifier. For off-line mass measurements, the laser ablation ion source was equipped with a newly developed miniature radiofrequency quadrupole trap in order to improve the extraction efficiency. A more economic use of the radioactive material enabled mass measurements using only 10^{15} atoms of target material. New mass measurements were performed within this work in the realm of the deformed shell closure N=152. Their implementation into the atomic-mass evaluation improved the uncertainty of more than 80 nuclides in the heavy mass region and simultaneously shifted the absolute mass of two α decay chains.

Hochpräzisionsmassenmessungen nahe des deformierten Schalenabschlusses bei N=152:
Die Masse eines Atomkerns spiegelt alle Wechselwirkungen in seinem Inneren wider. Es ist möglich, sie zum Test von Kernmassenmodellen zu benutzen und darüber hinaus mit ihrer Hilfe Informationen über die Kernstruktur zu erhalten. Penningfallen-Massenspektrometer haben in der Vergangenheit ihr Potential zum Erreichen höchster Präzision herausgestellt. Durch seine einzigartige Lage an einem Forschungsreaktor, wurde das Doppel-Penningfallen-Massenspektrometer TRIGA-TRAP eingerichtet, um Massenmessungen an neutronenreichen Nukliden durzuführen. Zur Erhöhung der Sensitivität wurde ein zerstörungsfreies Ionennachweissystem zur Durchführung von Massenmessungen an einzelnen Ionen implementiert. Dies umfasst den Aufbau eines schmalbandigen Filters, der auf die Zyklotronfrequenz schwerer Ionen angepasst ist, sowie eines rauscharmen kryogenen Verstärkers. Außerdem wurde die Effizienz der Laserablationsionenquelle durch den Einbau eines neuentwickelten kleinen Radiofrequenzquadrupols deutlich erhöht. Diese effizientere Nutzung des radioaktiven Materials erlaubt nun Massenmessungen mit nur 10^{15} Teilchen Ausgangsmaterial. Im Rahmen dieser Arbeit wurden Massenmessungen nahe des deformierten Schalenabschlusses bei $N = 152$ durchgeführt. Ihre Einbindung in die Atomic-Mass Evaluation verbesserte den Fehler von mehr als 80 Nukliden und verschob die absolute Masse von zwei α-Zerfallsketten.

Ei, die derffe doch gar nemmer gespalt wern.
- Fabian frei nach Badesalz

Contents

List of Figures

Chapter 1

Introduction

Since Einstein it is known, that mass and energy are equivalent, reflected by the formula $E = mc^2$. Thus, the binding energy of the nuclide and thereby its mass is the result of all present interactions. Using this, high-precision mass measurements open up the possibility to gain a unique insight into nuclear effects. For example the shell structure of the nucleus can be illustrated by the calculation of nucleon separation energies. From this, shell closures in the spherical and the deformed regime are visible. These stabilizing shell effects explain the existence of the superheavy elements, which are being searched and investigated by several collaborations worldwide.
These nuclear properties are also part of nuclear mass models, which manage to describe known nuclides rather well, but are not very reliable in making predictions outside the well-known regime. The bane is, that away from stability the majority of nuclide masses is linked via α or β decay chains to absolutely measured masses. As the models rely on this data it is desired to provide more directly measured nuclide masses away from stability as anchor points. These are usually relatively short-lived and do not exist in nature. Thus, they are made available for experimental research at radioactive ion beam facilities [Bla03b]. Longer-lived radionuclides exist especially in the heavy ion regime. Above plutonium, they are produced in specialized breeding reactors, from which they are made available as pure samples for off-line research or industrial applications.
Nowadays, many different experimental approaches allow mass measurements on the atomic scale. In general highest precisions can be reached with techniques based on frequency measurements. Among these, Penning trap experiments yield the highest precision. One of the mass spectrometer experiments is TRIGA-TRAP as part of the TRIGA-SPEC collaboration, located at the research reactor TRIGA Mainz. It is a double Penning-trap mass spectrometer where the mass measurement of the nuclide of interest is based on the determination of the cyclotron frequency ν_c of the stored ion: $\nu_c = qB/(2\pi m)$. The goal of TRIGA-TRAP is the investigation of neutron-rich radionuclides. Their directly measured masses serve the improvement of nuclear mass models and push the border of well-known nuclides further towards the expected r-process part. Since in particular the production rates far away from stability are fairly low, non-destructive detection techniques have to be adopted for these measurements, requiring only one ion for an entire mass measurement.

After an introduction to this technique in Sect. 3.4.2, the results of the commissioning are presented in Chap. 5.
In this work a laser ablation ion source has been equipped with a miniature buffer-gas filled radio-frequency quadrupole trap, allowing for in-situ ion cooling and a rough mass selection. This upgrade was necessary to increase the ion production efficiency in order to perform mass measurements on isotopes with limited availability or limited sample size due to radioactivity.
An order of magnitude in the ion production efficiency could be gained using the upgraded laser ablation ion source. This enabled mass measurements of long-lived nuclides in the transuranium region, opening up the possibility to study shell structure effects in this region with TRIGA-TRAP. The actual mass measurement was carried out with the destructive time of flight-ion cyclotron resonance technique. The experimental setup of the entire TRIGA-SPEC experiment is introduced in Chap. 4 along with the commissioning of the new laser ablation ion source.
First off-line mass measurements using the new ion source were performed, harvesting mass data of transuranium elements. This makes TRIGA-TRAP the second experiment, being able to perform mass measurements in this region. Nevertheless it is unique with the ability to perform an entire mass measurement of such nuclei with relative uncertainties as low as 5×10^{-9} with a sample size of 10^{15} atoms. The mass data is implemented into the Atomic-Mass Evaluation (AME) [Wan12], claiming to be the most complete collection of available mass data.
In total four nuclides of plutonium, americium and californium were directly measured for the first time, extending the knowledge on the deformed shell closure at $N = 152$. A discussion of the results as well as the implementation into the AME2012 is provided in Chap. 6, finalized with a closer look on the $N = 152$ deformed neutron shell gap as function of the proton number Z.

Chapter 2

The Nuclear mass

The mass is a fundamental property of an atom. About 90 years ago it was revealed that the mass of the atomic nucleus differs from the total mass of its constituents, referred to as packing fractions [Ast27]. Due to the equivalence of mass and energy, this is known today as the binding energy, which is essential for nuclear stability. Thus, the binding energy is an important measure since it reflects all interactions acting in the nucleus. In fact the total binding energy

$$B(N,Z) = \left[Nm_n + Zm_p + Zm_e - M(N,Z)\right]c^2 \tag{2.1}$$
$$= B_{nucl}(N,Z) + B_{elec}(N,Z) \tag{2.2}$$

is accessible by means of mass measurements via the mass $M(N,Z)$ of an atom with N neutrons, Z protons and Z electrons having the masses m_n, m_p and m_e, respectively. $B(N,Z)$ is the sum of the nuclear binding energy $B_{nucl}(N,Z)$ and the total binding energy of the electrons $B_{elec}(N,Z)$. With this knowledge, changes of nucleon-nucleon interactions should be represented by binding energy differences. However, experimental data displayed an odd-even staggering in the binding energy being related to the number of protons and neutrons. This was addressed later by the very successful liquid drop model with the Bethe-Weizsäcker mass formula [Wei35]. Since low-energy effects would not be visible in single nucleon separation energies due to the odd-even staggering, the two-neutron as well as two-proton separation energies

$$S_{2n}(N,Z) = B(Z,N) - B(N-2,Z) \tag{2.3}$$
$$S_{2p}(N,Z) = B(Z,N) - B(N,Z-2) \tag{2.4}$$

are well-suited to derive inner-nuclear changes.

Within almost all nuclei the nucleons are bound with an energy of 7 to 9 MeV as displayed in Fig. 2.1. The experimental data [Wan12] shows a strong increase of the binding energy per nucleon $B(N,Z)/A$ with $A = N + Z$ towards a maximum around ^{58}Fe. In addition smaller maxima are visible at ^{140}Ce and ^{208}Pb as well as at lighter nuclei. This is a hint for shell closures of either neutrons or protons in analogy to the electron shells. Displaying $S_{2n}(N,Z)$ and $S_{2p}(N,Z)$ using experimental data reveal shell closures

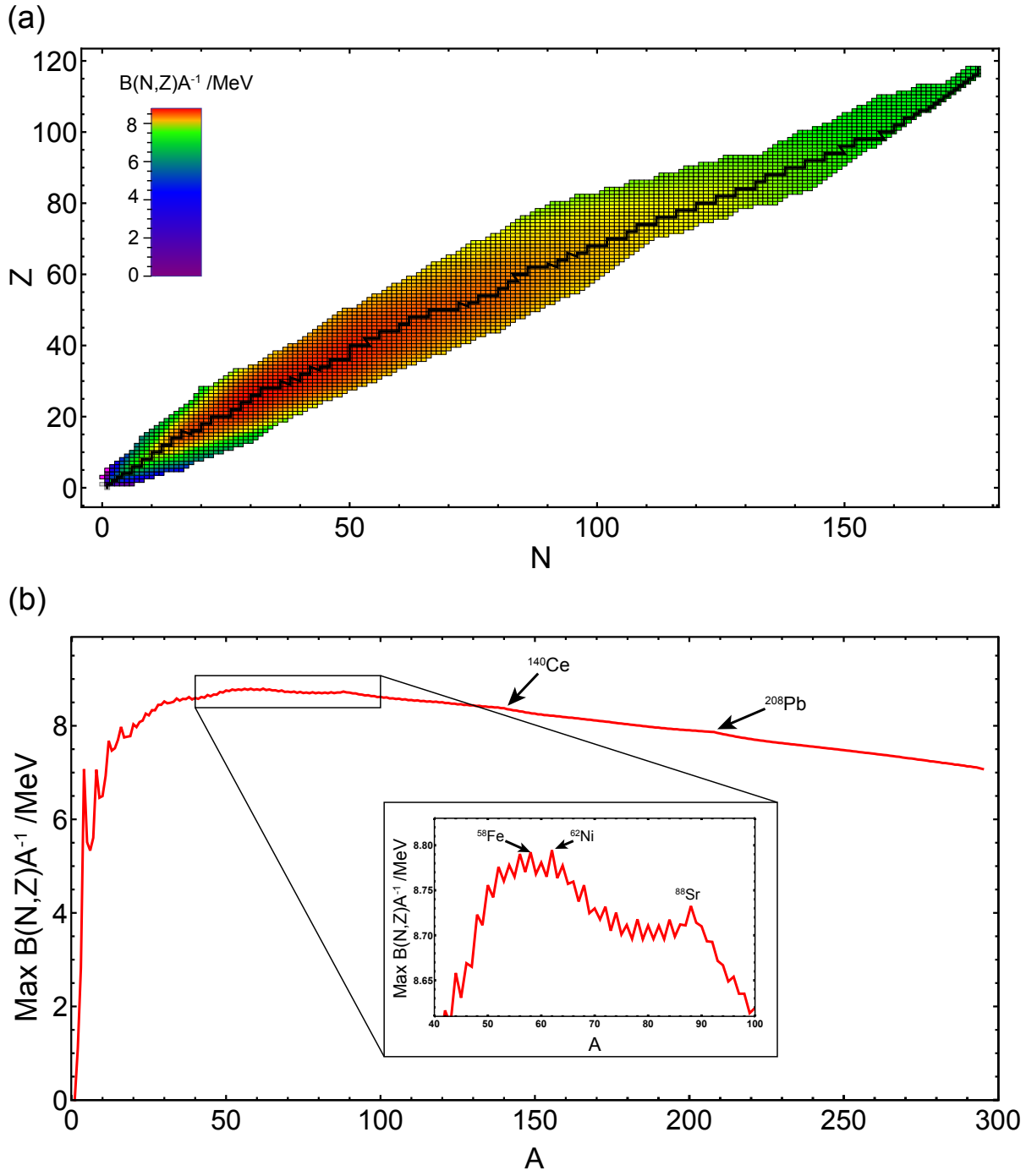

Figure 2.1: Binding energy per nucleon $B(N,Z)/A$ over the complete chart of nuclides. The 2D plot (a) shows that the nucleons in light nuclei are bound weakly, while in the majority the binding energy is between 7 and 9 MeV. The black line marks the nuclides with the strongest bound nucleons for each A. Their binding energy per nucleon is displayed in (b) with an additional focus on the nuclei with the strongest binding.

represented by a sudden decrease of the separation energy at which the nuclei experience higher stability. This happens at the so-called magic numbers $N = 2, 8, 20, 28, 50, 82, 126$ and $Z = 2, 8, 20, 28, 50, 82$. A proton shell closure at $Z = 126$ could not be confirmed yet due to the lack of experimental data. However, various models predict one around Z=114. Additionally to these magic numbers a deformed neutron shell closure at $N = 152$ is confirmed [Ram12]. It is also possible to describe the shell closures directly with the so-called shell gap parameters

$$\Delta_{2n}(N, Z) = S_{2n}(N, Z) - S_{2n}(N + 2, Z) \tag{2.5}$$
$$\Delta_{2p}(N, Z) = S_{2p}(N, Z) - S_{2p}(N, Z + 2) \ , \tag{2.6}$$

with the separation energies from Eqs. (2.3) and (2.4), where pairing effects already cancel out. Thus, with the advent of high-precision mass measurements, it became very useful to perform nuclear structure studies with the help of nuclear masses.
All these features being visible just by the experimental determination of nuclear masses awoke the curiosity as well as the urge to create theoretical models, being capable to explain the masses of existing nuclides. For example the upcoming hunt for elements with higher Z required a prediction of nuclear masses and lifetimes in not yet accessible regions of the chart of nuclides. The mass models which were created with the intention to describe the entire nuclide chart can be categorized into macroscopic-microscopic (mic-mac) (see Sect. 2.1) and purely microscopic (see Sect. 2.2) approaches. The mic-mac models are enhancements of the macroscopic liquid-drop model, which creates an analogy between the nucleus and a drop of incompressible liquid, being described by the Weizsäcker mass formula [Wei35]. Although it describes global trends very well, the introduction of corrections [Möl88] was required to compensate its incapabilities like the description of shell-closures. Also the sheer existence of very heavy nuclides can not be explained by the liquid drop model since the high Coulomb repulsion of the protons would result in a disruption of the nucleus [Boh39, Mye66].
Purely microscopic mass models attempt the description of the nucleus based on a solution of the Schrödinger equation. The complexity of many-body systems requires the use of effective potentials treating the nucleons as independent particles. This approach does not allow calculations on heavy nuclei but only up to ^{12}C [Nav00]. However, certain parameters are adopted from experimental results as input data [Lun03].
Both types of mass models have in common that their free parameters are adjusted to the experimental data to reach maximum agreement. Other approaches, like the Garvey-Kelson relations [Gar66] are purely phenomenological and account only for local trends fixed by experimental data of neighboring nuclei. Their predictions are in general more precise than global mass models but only reliable close to regions of very well-known masses. Lately it was demonstrated that they can be used as well for the prediction of nuclear charge radii [Pie10]. In the following sections different mass models are introduced based on the more detailed discussion in [Lun03].

2.1 Macroscopic mass models and their microscopic extension

From the constant nuclear density, manifested by measurements of nuclear radii and the relatively constant binding energy per nucleon, the concept of the saturation of nuclear forces arose. This implies that nucleons only interact with their next neighbors due to a short-range force, which is accounted for by a contribution to the binding energy, proportional to A. However, a correction proportional to the liquid drop surface and thus to $A^{2/3}$ has to be introduced since the nucleons being at the surface of the liquid drop have less neighbors than the inner ones. Due to the proton charge, a repulsive Coulomb force reduces the binding energy as well. With the assumption that the Z protons with charge e are uniformly distributed in the nucleus with the radius $r_0 A^{1/3}$ one gets

$$\frac{1}{4\pi\varepsilon_0}\frac{3e^2}{5r_0}Z^2A^{-1/3} \ . \tag{2.7}$$

Here r_0 denotes the charge-radius constant. In addition the fermion nature of both, protons and neutrons has to be taken into account. Therefore, each quantum state in the nucleus can only be populated once. Since the Fermi energy is defined by the last proton and neutron, a lowest order series expansion results in a proportionality to $(N-Z)^2/A$. This implies a binding energy reduction for asymmetric nuclei with $N \neq Z$. Such a correction has to be introduced as well for the nucleons at the surface [Mye66] leading to the Weizsäcker formula [Lun03]:

$$\begin{aligned} B(N,Z) = {} & a_{vol}A + a_{sf}A^{2/3} + \frac{1}{4\pi\varepsilon_0}\frac{3e^2}{5r_0}Z^2A^{-1/3} \\ & + (a_{sym}A + a_{ss}A^{2/3})\frac{(N-Z)^2}{A^2} - \delta a_p A^{-1/2} \ . \end{aligned} \tag{2.8}$$

The last term, although being part of Weizsäckers original concept, is not mentioned in [Lun03] since it is not a purely macroscopic part but was picked up in [Mye66]. It takes into account an empirically determined dependance on even and odd Z and N, resulting

Parameter	Value
a_{vol}	15.37 MeV
a_{sf}	-17.77 MeV
a_{sym}	-26.46 MeV
a_{ss}	17.7 MeV
a_p	11.2 MeV
r_0	1.2185 fm

Table 2.1: Parameters used in the Weizsäcker mass formula in Eq. (2.8). The values are taken from [Mye66] and [Lun03] .

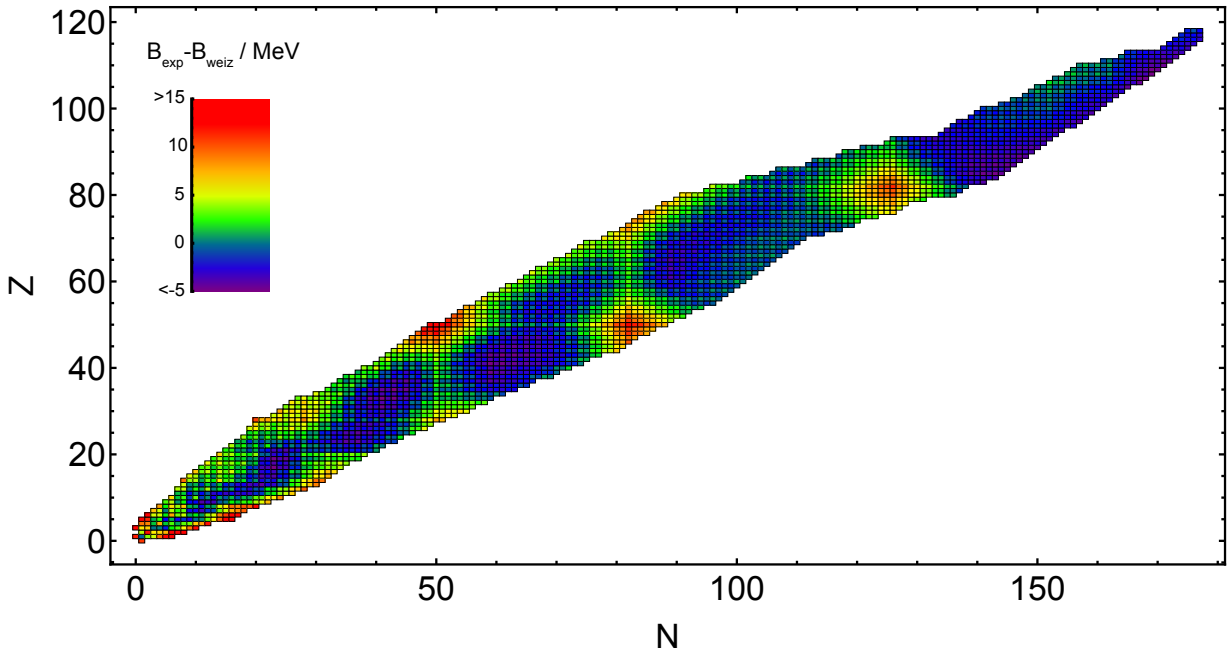

Figure 2.2: Plot of the difference between experimentally determined binding energies B_{exp} [Wan12] and the binding energies calculated from Eq. (2.8) B_{weiz} with the parameters given in Tab. 2.1. Strong deviations are visible at doubly magic nuclei.

in the so-called staggering. Thus, δ is +1 for nuclei with even numbers of protons and neutrons, -1 for nuclei with odd numbers of protons and neutrons and otherwise 0. Together with the surface symmetry correction this term is the first step towards the mac-mic mass models.

Fig. 2.2 displays the difference of the binding energy B_{exp}, which was determined experimentally and calculated with the Weizsäcker mass formula Eq. (2.8) with the parameter values given in Tab. 2.1. In the region of doubly magic nuclei the liquid-drop model tremendously underestimates the actual binding energy, in some cases by more than 15 MeV. The reason is that the consideration of shell effects is not implemented in this model. Also the effects of deformation are not accounted for, resulting in an overestimation of the binding energy. It also shows that this mass formula already calculates bound nuclei in the region of superheavy elements.

Nevertheless, to improve the model, mic-mac approaches were introduced, including microscopic shell corrections as they are used in the finite range droplet model (FRDM). For a better understanding the macroscopic term is represented as a sum of volume, surface and Coulomb energies, being similar to Eq. (2.8). First the volume energy is modified by an additional term displaying the compressibility of the nucleus with the parameter K_{vol}. This is, analogous to a liquid drop, a squeezing of the nucleus due to its surface tension while it is enlarged due to the repulsive Coulomb interactions between the protons. The modified surface term takes into account a certain surface stiffness Q_s [Mye69] as well

as a possible separation of protons and neutrons. Thus, their surfaces are treated independently. Expanding this result in powers of $A^{-1/3}$ two purely phenomenological terms $a_{cv}A^{1/3}$ and a_0A^0 are added. Nevertheless, their coefficients were equal to 0 [Möl95]. This results in the expression for the macroscopic energy [Lun03]:

$$\begin{aligned} E_{mac} = &- \left(a_{vol} + a_{sym}\delta^2 - \frac{1}{2}K_{vol}\varepsilon^2\right) A \\ &- \left(a_{sf} + \frac{9a_{sym}^2}{4Q_s}\delta^2\right) A^{2/3} \\ &- a_{cv}A^{1/3} - a_0A^0 \\ &- \frac{3e^2}{5r_0}\frac{Z^2}{4\pi\varepsilon_0}A^{-1/3} \\ &- \frac{9e^4}{400r_0^2Q_s}\frac{Z^4}{16\pi\varepsilon_0}A^{-2} \ . \end{aligned} \tag{2.9}$$

The parameters δ and ε are determined by minimizing E_{mac} and only hold for an equilibrium state. For the limit of large A it should be noted that Eq. (2.9) takes the form of the modified Weizsäcker formula given in Eq. (2.8). In addition to the already mentioned corrections, Eq. (2.9) was generalized to account for deformations: This was considered by the multiplication of correction factors to every term except the ones scaling with A [Mye74]. Furthermore, the surface correction was modified with an additional factor, which considers now the effect of the finite range of the nucleon-nucleon interactions [Möl81]. Finally an exponential correction was implemented, motivated by the tendency of the model to overestimate the calculated binding energies.
These corrections, either macroscopic in nature or purely phenomenological, may improve the overall theoretical modeling of the nuclear masses but they still do not have the ability to describe the binding energies properly around magic numbers.
One of the first attempts for their implementation was the approach of Strutinsky, proposing doubly humped fission barriers [Str67, Str68]. His approach was the introduction of microscopic effects to the macroscopic liquid drop model by simply adding a sum of correction energies to the binding energy, which originate from shell (E_s) and pairing effects (E_p). Here, the shell corrections are calculated as the difference between a realistic nuclear level-scheme with discrete energy levels

$$E_s = \sum_i n_i\epsilon_i \tag{2.10}$$

with occupation numbers n_i of the energy eigenvalues ϵ_i of the single particle Schrödinger equation, and a smoothed level distribution being represented by

$$\widetilde{E}_s = \int_{-\infty}^{\infty} \epsilon\widetilde{g}(\epsilon)\mathrm{d}\epsilon \ . \tag{2.11}$$

The smoothing function is chosen as a normalized Gaussian-like function

$$\widetilde{g}(\epsilon) = \frac{1}{\gamma\sqrt{\pi}} \sum_i n_i e^{-\frac{(\epsilon-\epsilon_i)^2}{\gamma^2}} \ , \tag{2.12}$$

which has a maximum at a properly defined value for ϵ. The smoothing parameter γ has to fulfill the conditions to be as large as the difference between the major shells. In addition it is chosen so that $\widetilde{E}_s$ is stable against variations in γ. These requirements can only be fulfilled for nuclei close to the valley of stability.
The development of the pairing corrections E_p is carried out by the Bardeen-Cooper-Schrieffer (BCS) model and addressed in more detail in Sect. 2.2.

In the FRDM model by Myers and Swiatecki first a single-particle field Φ needs to be specified, which fulfills the single-particle Schrödinger equation with eigenvalues ϵ_i. In the implementation of Strutinsky's approach the single-particle field is the sum of a spin independent nuclear part Φ_1, a spin-orbit and a Coulomb contribution $\Phi_{s.o.}$ and Φ_{coul} expressed as

$$\Phi = \Phi_1 + \Phi_{s.o.} + \Phi_{coul} \ . \tag{2.13}$$

The term describing the spin-independent part is a volume integral over a sphere with sharp radius R_{pot} written as

$$\Phi_1 = -\frac{V_0^q}{4\pi a_{pot}^3} \int \frac{e^{-|r-r'|/a_{pot}}}{|r-r'|/a_{pot}} \mathrm{d}^3 r' \tag{2.14}$$

with the potential V_0^q and the potential well a_{pot} being fitted parameters for protons and neutrons ($q = p, n$). The spin-orbit part of the single particle field is given as

$$\Phi_{s.o.}(r,p) = -\lambda^q \frac{\hbar}{4M^2c^2} \vec{\sigma}\vec{\nabla}\Phi_1(r) \times p \tag{2.15}$$

where $\lambda^q = k_q A + l_q$ is purely consisting of fit parameters except for the nucleon number A.
The Coulomb part of the field is also expressed as a volume integral over a solid sphere. Its radius r_0 is the same as in the macroscopic part of the FRDM model. It is written as

$$\Phi_{coul}(r) = \frac{Z^2e^2}{16/3\pi^2\epsilon_0 r_0^3 A} \int \frac{\mathrm{d}^3 r'}{|r-r'|} \ . \tag{2.16}$$

The implementation of these shell corrections as well as pairing as function of N and Z and charge-asymmetry effects being proportional to $(Z-N)$ are discussed in detail in [Möl95]. Finally the so-called Wigner term is introduced describing the already experimentally found effects due to odd or even N, Z. It adds an selective binding for neutrons/protons in the same shell orbital.

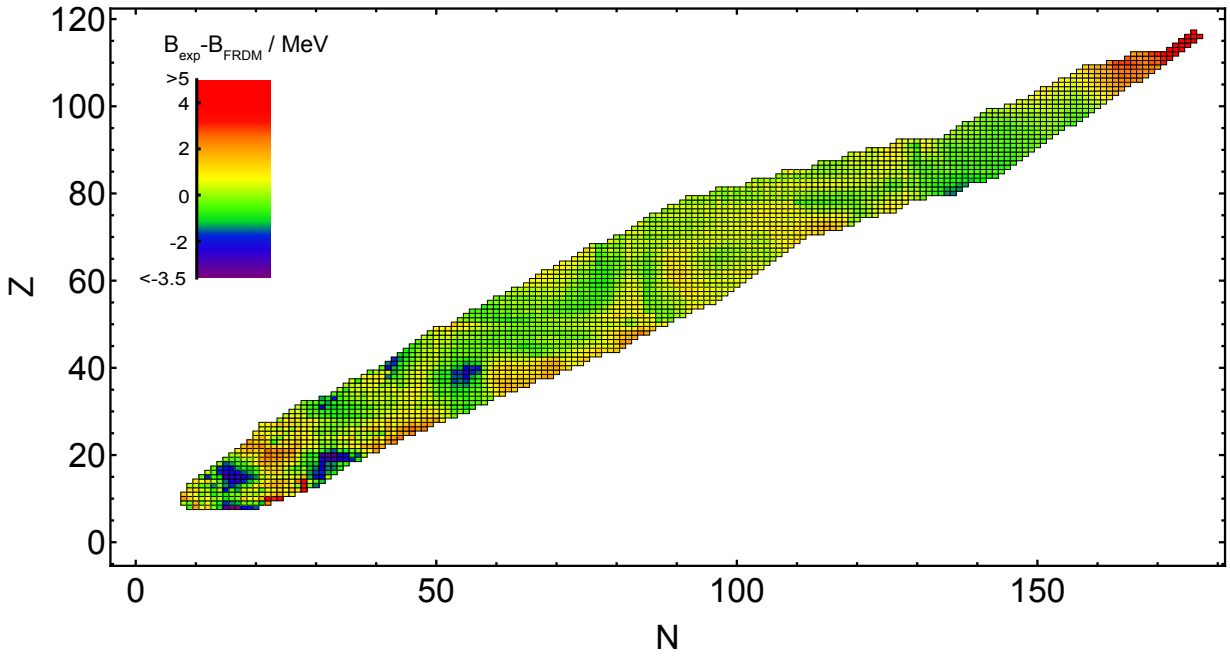

Figure 2.3: Plot of the difference between experimentally determined binding energies B_{exp} [Wan12] and the binding energies from the FRDM B_{FRDM} as published in [Möl95].

As displayed in Fig. 2.2 for the liquid drop model, the deviation of the binding energy obtained from the FRDM [Möl95] from the experimental data [Wan12] is displayed in Fig. 2.3. As a result from the introduced shell-corrections the FRDM reproduces the experimentally determined binding energies around doubly magic nuclei significantly better. Additionally the overall deviation from the AME2012 is also smaller compared to the liquid drop model. Also in comparison to other variations of the mic-mac approaches the FRDM is still the most accurate model.
Apart from these, other models, like the Extended Thomas Fermi plus Strutinsky Integral (ETFSI) [Gor00], which is related to the Hartree-Fock method due to its use of an effective force, as well as the Thomas-Fermi-Finite Range Droplet Model [Mye66] have to be mentioned for completeness as representatives of the mic-mac models.

2.2 Microscopic mass models

All mass models introduced in Sect. 2.1 were based on the macroscopic liquid-drop model. Another class of models, the purely microscopic ones, are discussed within this section. They all have in common to treat the nucleus as a many-body system of nucleons each of which is described by a single particle wave function. Then all interactions in the nucleus are described by the Schrödinger equation

$$H\Psi = E\Psi \tag{2.17}$$

with the non-relativistic Hamiltonian containing the interactions between all nucleons:

$$H = -\frac{\hbar}{2m}\sum_i \nabla_i^2 + \sum_{i>j} V_{i,j} + \sum_{i>j>k} V_{i,j,k} + \cdots \ . \tag{2.18}$$

The potentials V represent in this approach the two, three and more nucleon interactions. This many-body problems in combination with the short range of the strong interaction make it challenging to solve the Schrödinger equation since ordinary perturbation theory can not be applied in a practical way. Thus, it is not surprising that these ab initio calculations are not feasible to describe the entire nuclear chart. However, this changes, when the realistic nucleon-nucleon interaction is abandoned and replaced by an effective force, the so-called Hartree-Fock technique. Input for this model could also be phenomenological parameters [Lun03]. In general the Hartree-Fock methods can be classified into two different parametrization: One that uses a Gogny force [Dec80] and one that uses Skyrme forces [Vau72]. Although the Gogny forces are explicitly of finite range, and regarded as more realistic [Lun03], most calculations were performed employing the Skyrme parametrization, which is also discussed here.
For the introduction of an effective force, the Hamiltonian is changed to

$$H^{eff} = -\frac{\hbar}{2m}\sum_i \nabla_i^2 + \sum_i V_i^{eff} \tag{2.19}$$

with the effective force V_i^{eff}. It does not necessarily have to be in agreement with the data obtained from nucleon-nucleon scattering. With the introduction of this effective potential the interactions between nucleons are not explicitly considered any more. For practical reasons this description implies that the single particles interact with the effective field created by the other particles, which can be now regarded to be independent.
The multi particle wave function from Eq. (2.17) remains unknown. It is replaced by a trial wave function $\Phi = \det[\phi_i(x_i)]$, which is a completely antisymmetric product of normalized single particle wave functions $\phi_i(x_i)$. The only drawback is that Φ can not be identical with Ψ of Eq. (2.17). This has the effect that

$$E = \langle\Psi|H|\Psi\rangle < \langle\Phi|H|\Phi\rangle \ . \tag{2.20}$$

Hence, with the effective Hamiltonian and the single-particle wave functions the relation between the total energy and the energy density functional $\mathcal{E}$ is given by

$$E_{HF} = \langle\Phi|H^{eff}|\Phi\rangle \equiv \int \mathrm{d}^3r\, \mathcal{E}(r) \ . \tag{2.21}$$

For reasons of consistency the energy is required to be stable under variations of individual single particle states ϕ_i, which is taken into account by the relation

$$\frac{\delta}{\delta\phi_i}\left[E_{HF} - \sum_i \epsilon_i \int \mathrm{d}^3r |\phi_i(r)|^2\right] = 0 \ . \tag{2.22}$$

With this knowledge E_{HF} can be determined in several iterations by variations of ϕ_i in the single particle Schrödinger equation with the goal to find a minimum energy. The effective interaction used for these calculations is written with ten parameters [Ben03,Lun03,Vau72]:

$$\begin{aligned} v_{ij} =& t_0(1+x_0P_\sigma)\delta(\vec{r}_{ij}) + \frac{t_1}{2\hbar^2}(1+x_1P_\sigma)\left[p_{ij}^2\delta(\vec{r}_{ij}) + p_{ij}^{\dagger 2}\delta(\vec{r}_{ij})\right] \\ &+ \frac{t_2}{\hbar}(1+x_2P_\sigma)\vec{p}_{ij}^{\dagger}\delta(\vec{r}_{ij})\vec{p}_{ij} + \frac{i}{\hbar}W_0(\vec{\sigma}_i+\vec{\sigma}_j)\cdot\vec{p}_{ij}^{\dagger}\times\delta(\vec{r}_{ij})\vec{p}_{ij} \\ &+ \frac{t_3}{6}(1+x_3P_\sigma)\delta(\vec{r}_{ij})\rho^\gamma\left(\frac{\vec{r}_i+\vec{r}_j}{2}\right) . \end{aligned} \tag{2.23}$$

Here, $\vec{p}_{ij}$ denotes the momentum of the particles at location $\vec{r}_{ij}$ and $P_\sigma = \frac{1+\vec{\sigma}_1\vec{\sigma}_2}{2}$ the spin-exchange operator. Hence, the terms with $t_{0,1,2}$ describe the two-particle interactions. The term with t_3 describes a three-nucleon interaction, which is reduced to a two-nucleon interaction being in fact only valid for nuclei with even Z, N [Vau72]. Thus, it is a function of the local nucleon density $\rho = \rho_p + \rho_n$ being the sum of the local proton ρ_p and neutron ρ_n densities. The remaining term is describing a two-body spin-orbit interaction with the amplitude W_0.
With Eq. (2.23) the single particle Schrödinger equation is changed to

$$\left(-\vec{\nabla}\frac{\hbar^2}{2M_q^*(\vec{r})}\vec{\nabla} + U_q(\vec{r}) + V_q^{coul}(\vec{r}) - i\vec{W}_q(\vec{r})\cdot\vec{\nabla}\times\vec{\sigma}\right)\phi_{i,q} = \epsilon_{i,q}\phi_{i,q} \tag{2.24}$$

for q denoting protons (p) or neutrons (n) and i all their quantum numbers. Furthermore, $M_q^*(\vec{r})$ denotes the mass as function of the nucleon density. The parametrization from Eq. (2.23) determines the single-particle field $U_q(\vec{r})$, which is in general deformed and non-local. $V_q^{coul}(\vec{r})$ describes the Coulomb interaction and the last term is a description of the single-particle spin-orbit potential. Finally, it requires a rearrangement term, which has to be added to the ϵ_i for the calculation of the nuclear ground-state properties like binding energies, being due to the density dependence of the interaction [Vau72]:

$$E_R = -\frac{t_3}{8}\int \mathrm{d}^3r\,\rho_n(\vec{r})\rho_p(\vec{r})\rho(\vec{r}) . \tag{2.25}$$

All calculations up to now do only treat the nucleons as single particles within a field. However, it is known that pairing effects have to be considered with the formation of $p-p$ and $n-n$ pairs. Such pairing mechanisms were examined first in the theory of superconductors by Bardeen, Cooper and Schrieffer [Bar57]. An additional pairing term of the form

$$E_p = -G\left[\sum_{i>0}\sqrt{n_i(1-n_i)}\right]^2 \tag{2.26}$$

is added to the total energy [Vau73]. It is determined by the pairing strength G and the probability n_i that a certain eigenstate ϕ_i is occupied by the nucleons. However, the

results are only acceptable for nucleons close to stability but not close to the neutron drip line, which is due to the pairing matrix elements being treated as constants [Dob84]. In the Bogolyubov method this is avoided since single-particle as well as pairing effects are treated simultaneously [Ben03, Lun03]. According to the technique being used for the pairing treatment, the models are named either Hartree-Fock Bardeen-Cooper-Schrieffer (HF-BCS) or Hartree-Fock-Bogolyubov (HFB).
With this treatment, it was found that the Hartree-Fock models underbind the nuclei with $N - Z$ systematically. Thus, the Wigner term, proposed for mic-mac models [Mye66] is integrated into this models as well.
Limitations of the Hartree-Fock models lie in the regions around doubly magic nuclei. There, they fail to reproduce the well-established data of the shell gaps, which is called mutually enhanced magicity.

2.3 The Duflo-Zuker mass formula

The approach by Duflo and Zuker [Duf94, Duf95, Zuk94] sticks out of the variety of mass models since it is able to reproduce the masses of the existing nuclei with the highest precision (for a comparison to other models, see Sect. 2.5) and it is very powerful in the prediction of unknown masses [Men08]. It is a functional of orbital occupation [Zuk08], based on the assumption that smooth pseudopotentials exist within the nucleus allowing Hartree-Fock calculations. This allows to split the Hamiltonian H_D into a monopole H_m and a multipole term H_M [Lun03]:

$$H_D = H_m + H_M \ . \tag{2.27}$$

The monopole term can be regarded as the Hartree-Fock part of the model, as it is taking care of single-particle properties and saturation effects while the multipole term, acting as a residual interaction, is fully determined by nucleon-nucleon potentials. Thus, it is parameter-free [Duf95]. However, it is not given explicitly in the calculations. H_m is treated phenomenologically given explicitly as

$$H_m = \sum_{k,l} a_{kl} m_k (m_l - \delta_{kl}) + b_{kl} \left(T_k \cdot T_l - \frac{3m_k}{4} \delta_{kl} \right) \tag{2.28}$$

containing only quadratic terms of the number m_k and the isospin operators T_k. Its dominant terms were identified due to geometric parallels to realistic forces but also scaling of amplitudes was required. The first result was a set of 28 parameters in the first version [Duf95]. Recently, two standard versions exist, a 31 parameter variant and a 10 parameter version [Zuk08]. The model exists also with an extension to 33 parameters [Men08].
Fits to the Atomic Nass Evaluation from 2003 [Aud03] show a very good agreement with the data and demonstrate the reproduction of the shell gaps. Only around $N = 50$ the Duflo-Zuker model does not agree with the experimental data. Further tests of this model performed in [Men08] were carried out by fits to several subsets of the AME2003 ranging

from $1 \leq A \leq 160$ to $1 \leq A \leq 200$ and prediction of the remaining nuclides above this threshold. Remarkably, the deviations of the predicted nuclides from the experimental data was the largest for the fit to $A \leq 200$ nuclides although no extreme deviations were observed in the fit errors for all different subsets. However, even with the largest error the prediction of the Duflo-Zuker mass model is superior to all other global mass models in the heavy region of the nuclide chart.

2.4 Local mass formulas

All mass models introduced up to now had in common that they tried to reproduce the entire nuclide chart with a global approach. With the treatment of the mass as a three-dimensional surface as function of N, Z, the so-called mass-surface, it is observed that local trends are relatively smooth. Excluded from this statement are trends in the vicinity of magic and especially doubly magic nuclei. This behavior is easily visible by the calculation of derivatives of the mass surface along constant N, Z, A, $(N - Z)$ being equal to, two-neutron and two-proton separation energies as well as Q_β and Q_α energies. Nevertheless, dents in the derivatives are also present in neighboring chains. They vanish only in some cases in the S_{2n} and S_{2p}, which is known as the so-called shell-quenching.
These properties are used in the AME for the extrapolation to nuclides which are not discovered yet. In order to keep the mass surface as smooth as possible, known separation energies of neighboring nuclide pairs are considered. Interpolations are performed with the same technique [Aud12b]. Previous issues of the AME demonstrated a very high predictive power of this procedure [Lun03].
Clear algebraic relations between neighboring nuclides were introduced by Garvey and Kelson. They proposed that, as long as it is not possible to determine the exact form of the Hamiltonian and calculate $M(Z, N)$, at least mass differences of neighboring nuclides could be understood. This includes the assumption that the single-particle energies as well as the effective interactions vary smoothly and slowly with A. The general form of their approach

$$\sum_{i=1}^{\alpha} C_i M(N_i, Z_i) = 0 \tag{2.29}$$

with $|C_i| = 1$ is chosen so that in a linear combination the interactions between nucleons would vanish in first order. Thus, α is required to be an even integer, as then all neutron-neutron and proton-proton interactions cancel out. The vanishing of the neutron-proton interaction is secured by the additional constraint

$$\sum_{i=1}^{\alpha} C_i N_i Z_i = 0 \ . \tag{2.30}$$

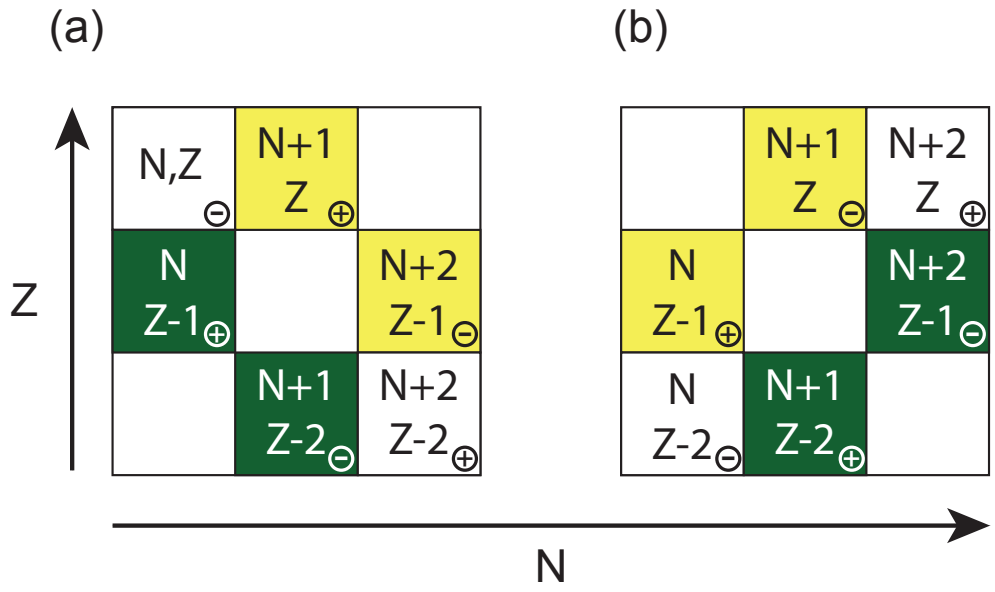

Figure 2.4: Illustration of the most simple Garvey-Kelson relations listed in Eqs. (2.31) (a) and (2.32)(b). The masses of nuclides are summed with the sign given in the bottom right corner of each box.

The simplest choice for such an equation is obviously with $\alpha = 6$ yielding two different equations:

$$\begin{aligned} &M(N+2,Z-2) - M(N,Z) \\ &+M(N,Z-1) - M(N+1,Z-2) \\ &+M(N+1,Z) - M(N+2,Z-1) = 0 \ , \end{aligned} \tag{2.31}$$

$$\begin{aligned} &M(N+2,Z) - M(N,Z-2) \\ &+M(N+1,Z-2) - M(N+2,Z-1) \\ &+M(N,Z-1) - M(N+1,Z) = 0 \ . \end{aligned} \tag{2.32}$$

While Eq. (2.31) was already mentioned in [Gar66], Eq. (2.32) was discovered a few years later with this further developed approach. An illustration of both equations is shown in Fig. 2.4. The masses of nuclides are summed with the sign given in the bottom right corner of each box. A closer look reveals in Eq. (2.31) that three nuclide pairs with the mass numbers $A-1, A, A+1$ are involved with the pair members differing in the isospin projection $\propto (N-Z)$ and vice versa in Eq. (2.32). The former equation is more interesting as it provides the possibility to predict a mass for nuclides further away from stability calculating the mass of the nuclide with $(N+2, Z-2)$ on the neutron-rich and with (N, Z) on the neutron-deficient side, respectively.

This approach was developed further by the interpretation of Eq. (2.31) as a third-order partial difference equation with the most general solution [Jän88]

$$M(N,Z) = G_1(N) + G_2(Z) + G_3(N+Z) \ . \tag{2.33}$$

The point functions G_i are determined by a fit to a subset of experimental data. Here, it was important to use relatively small subsets, which are limited to either neutron-rich or neutron-deficient nuclides to avoid long-range extrapolations.
For completeness it should be mentioned that the isobaric-multiplet mass equation (IMME) was developed in a different approach with the result that the mass of nuclides in an isospin multiplet follow the parabolic relation [Wei59, Gar69]

$$m(T,T_z) = \alpha + \beta T_z + \gamma T_z^2 \tag{2.34}$$

with the coefficients α, β, γ being unique for each multiplet with isospin T and its projection T_z. This requires the assumption that in first order the nuclear interactions are charge-independent within an isospin multiplet. The charge dependence is treated as a perturbation linked to two-body interactions being responsible for the separation of the members of the multiplet.

2.5 Quality tests of mass models

After the description of several different types of mass models the question arises, how precisely they reproduce the experimentally determined data including the experimental values to which they were fitted. General comparability is usually reached by the determination of the root-mean-square (rms) error

$$\sigma_{rms} = \sqrt{\frac{1}{N}\sum_{i=1}^{N}\left(M_i^{exp} - M_i^{theo}\right)^2} \ , \tag{2.35}$$

returning a mean deviation of model-based masses M_i^{theo} from experimental values M_i^{exp} for N nuclides. A slightly different approach takes the uncertainties of the experimental

Mass Model	σ_{rms} /MeV	Publication
Liquid drop	2.97	[Lun03]
FRDM95	0.676	[Möl95]
FRDM12	0.570	[Möl12]
HFB2	0.702	[Lun03]
HFB25	0.58	[Gor13]
DZ	0.297-0.372	[Men08]

Table 2.2: Overview of the root mean square error σ_{rms} of fits of several global mass models to the AME2003 [Aud03].

data into account as well. By applying the method of maximum likelihood σ_{rms} is modified to a model standard deviation

$$\sigma_{mod} = \sqrt{\frac{1}{\sum w_i} \sum_{i=1}^{N} w_i \left[\left(M_i^{exp} - M_i^{theo} \right)^2 \right] - \sigma_i^2} \tag{2.36}$$

with the weighting factors

$$w_i = \frac{1}{(\sigma_i^2 + \sigma_{mod}^2)^2} \tag{2.37}$$

introduced in [Möl88] requiring several iterations. σ_{mod} was determined for the 382 nuclides appearing in the AME2003 version for the first time. However, since both, σ_{rms} and σ_{mod}, usually don't differ more than 10 % only the former is reported here. An overview of σ_{rms} obtained by fits of several global mass models is given in Tab. 2.2. As demonstrated in Fig. 2.2 the liquid drop model is not able to reproduce nuclide masses in the vicinity of doubly magic nuclei as it does not account for shell effects. This is represented by a σ_{rms} of 2.97 MeV [Lun03] being about one order of magnitude larger than the rms error of the modern models.The FRDM from [Möl95] already reproduces the data a lot better with $\sigma_{rms} = 0.676\,\text{MeV}$. The latest version, also fitted to [Aud03] was improved significantly ($\sigma_{rms} = 0.570\,\text{MeV}$) [Möl12]. Slightly larger errors were obtained from the HFB approaches in 2003 ($\sigma_{rms} = 0.702\,\text{MeV}$) [Lun03] but were improved significantly ($\sigma_{rms} = 0.580\,\text{MeV}$ with respect to the AME2003 and $\sigma_{rms} = 0.54\,\text{MeV}$ with respect to the AME2012) [Gor13]. Nevertheless, the global approach reproducing the experimental data with the smallest error is the model developed by Duflo and Zuker ($\sigma_{rms} = 0.373\,\text{MeV}$). Investigations from 2008 yielded an rms error, between 0.372 MeV and 0.297 MeV depending on the fit range. It was also observed that the predictive power decreases with an increased set of input data: In the cases where the fit was only limited to nuclides with $A \leq 200$, the errors in the prediction of the remaining nuclides were larger than 1.3 MeV [Men08].
Local mass formulas used to be unbeatable as they are of course only applicable to limited regions, like the one from Garvey and Kelson. Applied at only small areas of the nuclide chart they could reproduce 242 of the nuclides added to the AME2003 with an error less than 0.232 MeV. They were also employed for tests in which rms deviations between 0.1 MeV and 0.2 MeV could be obtained, depending on the mass regime. In the case that the nuclide can be predicted by the maximum number of twelve different relations, the rms deviation is around 87 keV [Bar08]. Further improvements might be possible since a systematic deviation of Eqs. (2.31) and (2.32) from 0 were found, which could be taken into account for further optimizations of predictions [He13]. The isobaric-multiplet mass equation (see Eq. (2.34)) is more limited in its application. Its predictive power was tested intensively in [Bla03a] where deviations of less than 500 eV between theory and experiment were reported.

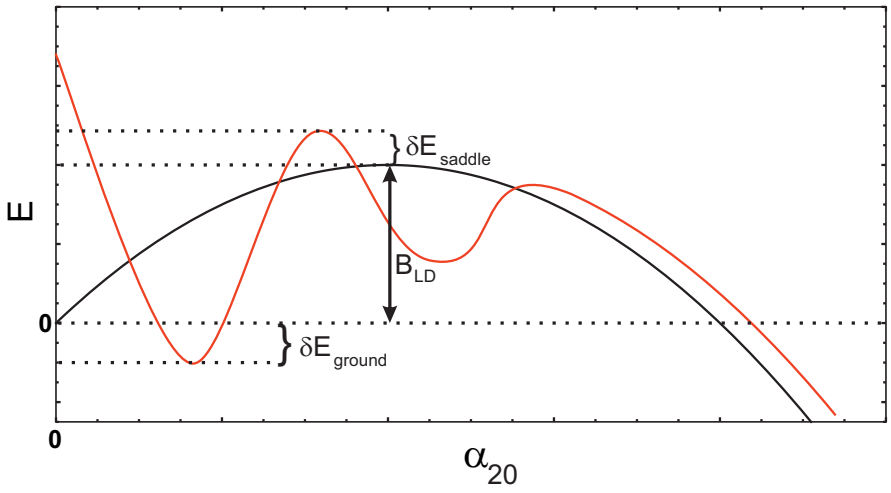

Figure 2.5: Sketch of the sum of Coulomb and surface energy of the liquid drop model with (red) and without (black) shell corrections as function of the quadrupolar deformation α_{20}. Due to the shell corrections a saddle point is introduced, enhancing the fission barrier with δE_{saddle}. This also results in a deformed ground state.

2.6 Shell effects for heavy and superheavy elements

In the previous sections it was already depicted that all mass models fail to reproduce the nuclear masses with the experimentally reached precision. Nevertheless, they are an important factor in the general understanding of heavy and the sheer existence of superheavy elements. Moreover, the global models can also help to make predictions about the positions of the next magic numbers for higher Z and N.

Especially experiments on superheavy elements are nowadays performed with great effort due to very low production rates in the required reaction channels. However, elements up to $Z = 117$ and 118 have been observed and identified by α-decay chains linking them to well-known nuclei [Oga12]. The existence of such heavy nuclides can not be explained at all with the pure liquid drop model approach since in a certain region the repulsive effect of the Coulomb energy is dominating over the attractive surface term. As a rule of thumb, $Z^2/A > 41$ nuclides can not exist in the liquid drop model [Boh39]. Thus, it is not surprising that the liquid drop model is also not very successful in the prediction of masses in the transuranium region. Only the introduction of shell effects explains the existence of higher Z elements. Their influence is pointed out in Fig. 2.5. This sketch demonstrates the changes of the sum of Coulomb and surface energy as function of quadrupolar deformation α_{20} (black line). B_{LD} marks the fission barrier in the liquid drop model. Due to the influence of the Coulomb energy it falls below 0 for nuclides with $Z^2/A > 41$. The red line denotes the potential created by the mic-mac models. The microscopic contributions change the potential significantly as function of α_{20} creating a potential minimum for a deformed nucleus. More important is the saddle point, being higher than the liquid drop fission barrier. This allows the existence of nuclei beyond $Z^2/A = 41$, which are stable

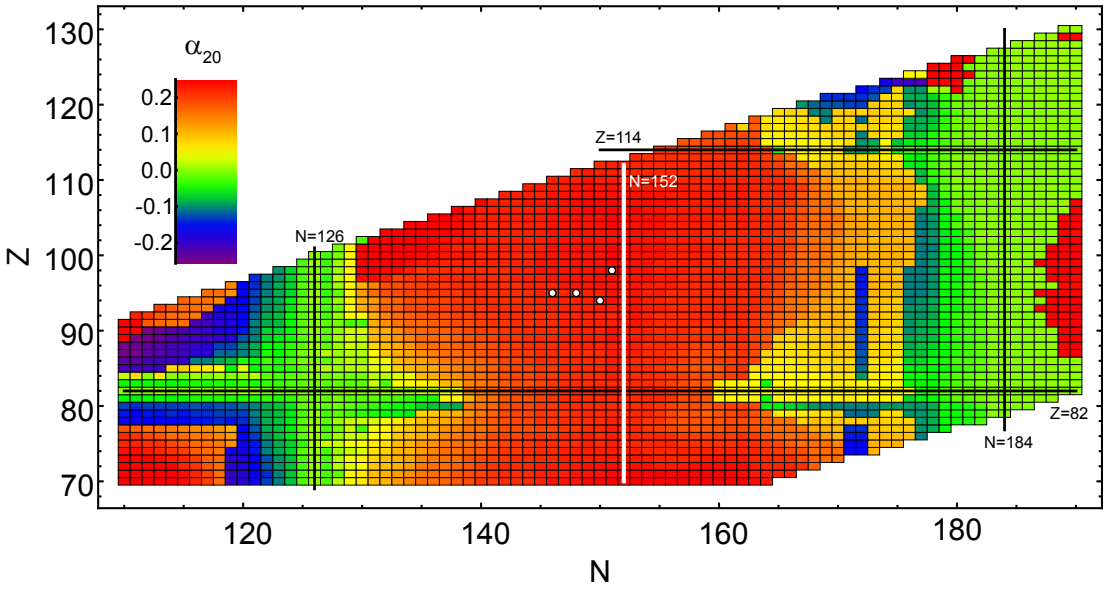

Figure 2.6: Calculated quadrupole deformation α_{20} from the FRDM in the realm of heavy and superheavy elements [Möl95]. The four white circles mark the four transuranium nuclides measured at TRIGA-TRAP. Nuclides with positive/negative α_{20} are prolate/oblate, respectively. Around doubly magic numbers the nuclei are spherical.

against spontaneous fission. The potential shown in Fig. 2.5 is characteristic for a prolate nucleus. For an oblate shape the α_{20} is negative. Exemplarily the deformation from the FRDM [Möl95] is shown in Fig. 2.6 for the vicinity of the heavy elements. The white circles in the plot are the four transuranium nuclides investigated within this thesis at TRIGA-TRAP.

Due to the shell effects it was found that apart from the spherical doubly magic nuclei like ^{208}Pb, regions of enhanced stability at $Z = 100$ and $N = 152$ exist being referred to as deformed shell closure. More deformed shell-closures are predicted for $N = 162$ and $Z = 108$ [Möl94, Möl95]. No consensus could be reached up to now on the position of the next magic numbers, while mic-mac models are favoring $Z = 114, N = 184$, Skyrme-Hartree-Fock models predict them further out at $Z = 124, N = 184$. Other approaches even prefer $Z = 120, N = 172$ [Ben03].

The impact of the microscopic corrections in the strongly deformed transuranium region, being mainly due to shell corrections, is displayed in Fig. 2.7. Around the deformed shell-gap the binding is enhanced by a few MeV. It should also be noted that the magic numbers in Fig. 2.7 differ slightly from the predictions of up-to-date mic-mac approaches. Apart from the nuclides investigated within this work, further mass measurements are planned at TRIGA-TRAP to help mapping the shell gap at $N = 152$ for a better understanding of the models. In addition direct mass measurements of No and Lr were already performed at SHIPTRAP, GSI [Dwo09, Blo10, Dwo10, Ram12]. The main binding energy contributions in this region originate from shell-effects, providing stability against spontaneous fission.

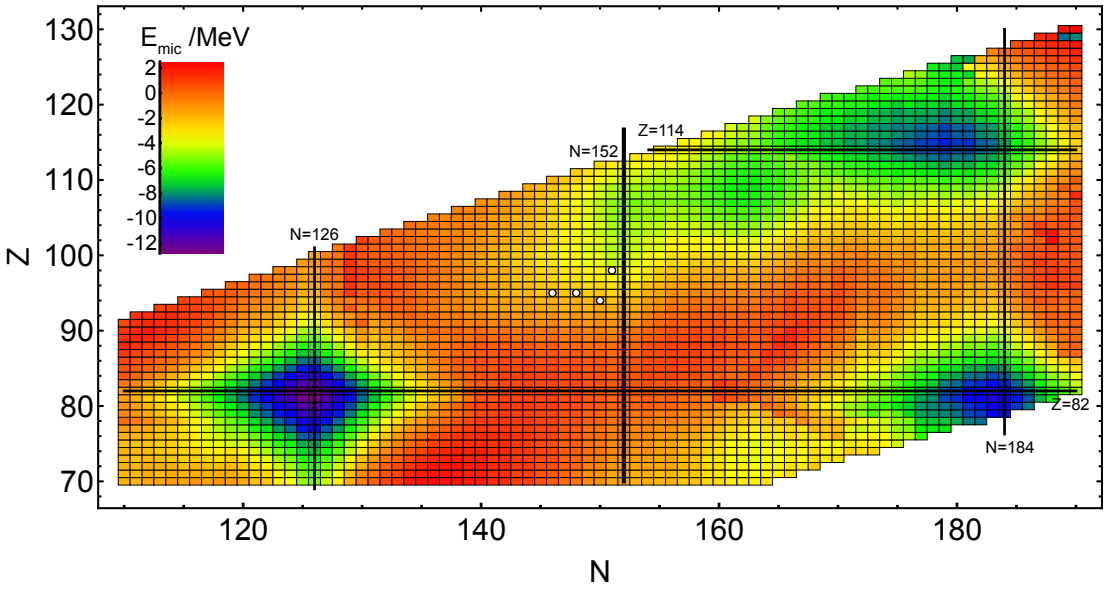

Figure 2.7: Calculated microscopic corrections from the FRDM in the realm of heavy and superheavy elements. The large energy corrections illustrate the impact of the microscopic model with respect to the finite range liquid droplet model [Möl95]. In the region of the TRIGA-TRAP measurements (white dots), the microscopic effects enhance the binding by a few MeV.

However, other nuclear transitions, here mainly α decays, limit their lifetime. Since these transitions are always a function of their Q-value, mass models allow predictions on nuclear lifetimes as well.

Chapter 3

Mass measurements with Penning traps

The first mass spectrometric experiments, beginning with Thomson and the discovery of two neon isotopes [Tho13] and continuing with Aston and Dempster, were based on the precise knowledge of electric and magnetic fields. However, the observable that can be measured with highest precision is nowadays a frequency. Thus, mass measurements have been converted into frequency measurements, for example into the comparison of rotational frequencies in a magnetic field of a Penning trap. Ions are stored in a superposition of a strong homogeneous magnetic field for radial and a weak electrostatic quadrupole potential for axial confinement. For the development of the ion trap technique the Nobel Prize in physics was partially awarded to Dehmelt [Deh90] being inspired by the previous work of Penning [Pen36] and Pierce [Pie49]. Instead of storage inside a magnetic field, an oscillating electric field can be used. For this concept of the Paul trap Paul received the Nobel Prize as well [Pau90].
The ion motion is well understood including analytically solved equations of motion. This is described briefly in Sect. 3.1. While ions with large mass difference do not even reach the trap due to time-of-flight selection by a beam gate, isobaric contaminants have to be cleaned away by other techniques. Presently reachable precisions $\frac{\delta\nu}{\nu}$ of 10^{-9} for stable as well as exotic species at experiments like TRIGA-TRAP demand a careful preparation of the ions in the trap. Thus, the motional amplitudes should be small to minimize the effect of electric or magnetic field imperfections. Since imperfections can not be vanished entirely their effects are discussed in Sect. 3.2. The possibilities of ion motion manipulation are discussed in Sect. 3.3. For further information beyond this chapter the reader is referred to [Bro86, Maj05, Kre07].
The actual mass measurement is performed by exciting certain ion motions and a subsequent ion detection, which can be non-destructive while the ion is kept inside the trap or destructive, requiring an ejection to a detector outside the magnetic field. These techniques are described in detail in Sect. 3.4 focusing on the detection methods used at TRIGA-TRAP.
Today several Penning traps are set up around the world providing high-precision mass

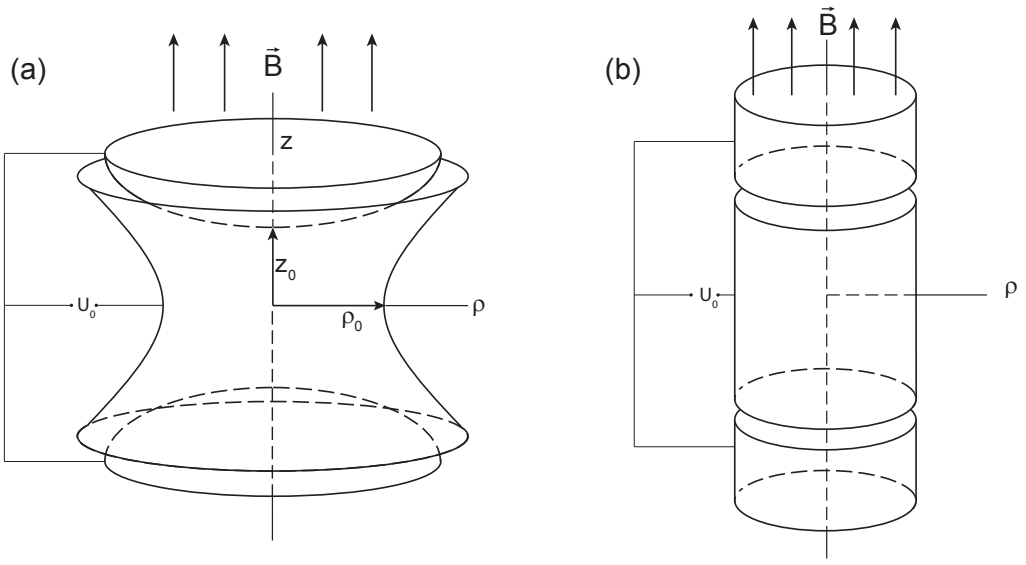

Figure 3.1: Electrode configuration of a Penning trap with hyperbolic (a) or cylindrical (b) shape. Particles are trapped by applying an electric voltage U_0 between the ring electrode and end caps depending on the sign of the ion charge.

data on almost the entire nuclear chart [Bla06]. Apart from masses other fundamental properties like g-factors can be determined with Penning traps, which can even be used to derive fundamental constants like the electron mass [Stu13].

3.1 The ideal Penning trap

When a particle with charge q and mass m enters a homogeneous magnetic field $\vec{B} = B\vec{e}_z$ with a velocity $\vec{v} = (v_x, v_y, v_z)$ it is deflected with a force perpendicular to the field lines, the Lorentz force $\vec{F}_L = q\vec{v} \times \vec{B}$. By equating Lorentz and centrifugal forces, one obtains the free cyclotron frequency

$$\omega_c = \frac{q}{m}B \tag{3.1}$$

for the helical motion around the magnetic field lines. This illustrates that a magnetic field provides only a confinement in two dimensions. Storage inside a finite three-dimensional volume is achieved by adding a weak electric quadrupole potential.

Fig. 3.1 displays the configuration of a Penning trap. The equipotential surfaces of an ideal quadrupole potential are hyperboloids, being approached by the hyperbolic Penning trap (see Fig. 3.1(a)). However, the drawback in experimental reality is the very closed structure, which is avoided by cylindrical electrodes (Fig. 3.1(b)). Depending on the sign of the particle charge a voltage U_0 is applied between the ring electrode and end caps. With the z-axis being defined by the direction of the magnetic field and the origin in the

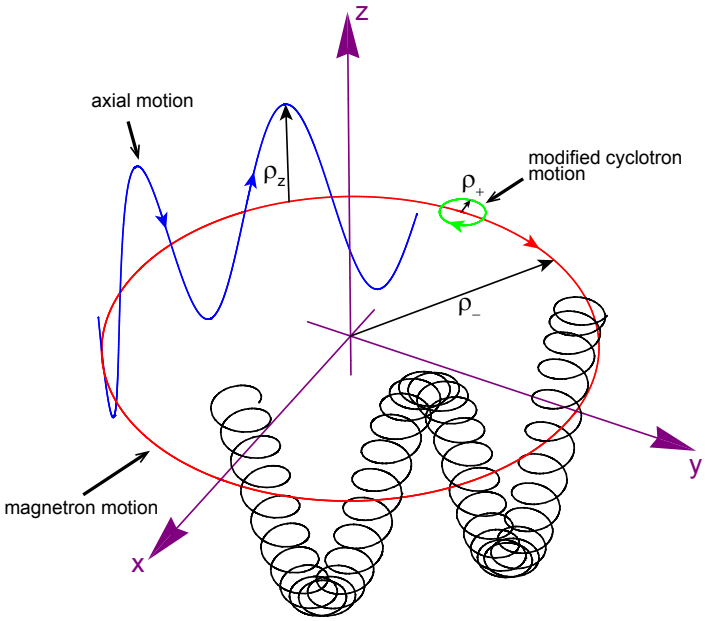

Figure 3.2: Sketch of the ion motion in a Penning trap with the magnetic field being aligned to the z-axis (not to scale). The ion motion can be resolved into three independent eigenmotions: Modified cyclotron (green), magnetron (red) and axial motion (blue). The black line displays the superposition of all three eigenmotions.

center of the trap one obtains the electric potential

$$U(z,r) = \frac{U_0}{2d^2}\left(z^2 - \frac{\rho^2}{2}\right) \ . \tag{3.2}$$

Here, d is the so-called trap parameter determined by the minimal distance between the center of the trap to the ring electrode ρ_0, and to the end caps z_0 (see Fig. 3.1):

$$d^2 = \frac{1}{2}\left(z_0^2 + \frac{\rho_0^2}{2}\right) \ . \tag{3.3}$$

From the force a particle experiences in this superposition of electric and magnetic fields

$$m\ddot{\vec{\rho}} = -q\nabla U + \dot{\vec{q}}\vec{\rho} \times \vec{B} \ , \tag{3.4}$$

the equations of motion are easily transformed to Cartesian coordinates indicating three independent eigenmotions [Kre91]

Nuclide	mass / u	ν_c / kHz	ν_+ / kHz	ν_z / kHz	ν_- / kHz
$^{1}H^{+}$	1	107492.83	107489.68	822.30	3.15
$^{12}C^{+}$	12	8957.74	8954.59	237.38	3.15
$^{12}C_{8}^{+}$	96	1119.72	1116.56	83.93	3.15
$^{12}C_{15}^{+}$	180	597.18	594.02	61.29	3.16
$^{241}Am^{+}$	241	446.03	442.86	52.97	3.17
$^{249}Cf^{16}O^{+}$	265	405.63	402.46	50.51	3.17

Table 3.1: Calculated free cyclotron frequency and eigenfrequencies $\nu_i = \omega_i/(2\pi)$ for some nuclides of interest in the precision trap of TRIGA-TRAP (see Sect. 4.2) using the experimental parameters $d = 5.03$ mm, $B = 7$ T, $U_0 = 7$ V. The magnetron frequency ν_- is almost mass independent.

$$\begin{aligned} \ddot{x} &= \frac{\omega_z^2}{2}x + \omega_c B\dot{y} \\ \ddot{y} &= \frac{\omega_z^2}{2}y - \omega_c B\dot{x} \\ \ddot{z} &= -\omega_Z^2 z \end{aligned} \tag{3.5}$$

with the cyclotron frequency ω_c and the axial frequency

$$\omega_z = \sqrt{\frac{qU_0}{md^2}} \ . \tag{3.6}$$

The radial motion is characterized by a repulsive electrostatic and a restraining magnetic force. It can be treated easier with the complex ansatz $u = x + iy$, which yields the differential equation

$$\ddot{u} + i\omega_c\dot{u} - \frac{\omega_z^2}{2}u = 0 \ . \tag{3.7}$$

Using the exponential representation of a complex number $u = u_0 e^{-i\omega t}$ one obtains the relation

$$\omega^2 - \omega_c\omega + \frac{\omega_z^2}{2} = 0 \tag{3.8}$$

with the eigenfrequencies of the radial motion

$$\omega_\pm = \frac{1}{2}\left(\omega_c \pm \sqrt{\omega_c^2 - 2\omega_z^2}\right) \ , \tag{3.9}$$

where ω_+ is the reduced cyclotron frequency and ω_- the magnetron frequency. Fig. 3.2 illustrates the ion motion in the trap composed of the three eigenmotions. Typical eigenfrequencies as well as the cyclotron frequency of certain singly charged ions at TRIGA-TRAP are presented in Tab. 3.1.

A series expansion of $\omega_\pm$ obtaining

$$\omega_- \approx \frac{U_0}{2d^2B} \tag{3.10}$$

$$\omega_+ \approx \omega_c - \frac{U_0}{2d^2B} \tag{3.11}$$

clearly shows that ω_- is in lowest order mass independent while ω_+ is ω_c modified by the contribution of the electric and magnetic field.
Eqs. (3.6) and (3.9) reveal two constraints. Due to the decoupling of the motion in z-direction (see Eq. (3.5)) it is obvious that the sign of the particle charge and the polarity of the potential difference have to be identical for axial confinement. The requirement $\sqrt{\omega_c^2 - 2\omega_z^2} > 0$ from Eq. (3.9) is more general. By using Eqs. (3.1) and (3.6) it illustrates the need of a minimum magnetic field strength to counter the repulsion by the electric field:

$$\frac{|q|}{m}B^2 > \frac{4|U_0|}{d^2} \tag{3.12}$$

$$qU_0 > 0\ . \tag{3.13}$$

Furthermore, Eq. (3.9) reveals the useful relations

$$\omega_+ + \omega_- = \omega_c \tag{3.14}$$

$$2\omega_+\omega_- = \omega_z^2\ , \tag{3.15}$$

which are routinely used in Penning-trap mass spectrometry [Gab09]. In case of a real Penning trap where field inhomogeneities, unharmonicities or a tilting angle between trap axis and magnetic field are present and modify the eigenfrequencies to $\widetilde{\omega}_+$, $\widetilde{\omega}_-$ and $\widetilde{\omega}_z$. For these modified frequencies the so called invariance theorem [Bro86]

$$\omega_c^2 = \omega_+^2 + \omega_-^2 + \omega_z^2 \tag{3.16}$$

$$= \widetilde{\omega}_+^2 + \widetilde{\omega}_-^2 + \widetilde{\omega}_z^2 \tag{3.17}$$

has to be used.
In order to learn something more about the ions energy inside the trap one needs the solution of Eq. (3.5) being

$$\begin{aligned} x(t) &= \rho_+ \cos(\omega_+ t + \phi_+) + \rho_- \cos(\omega_- t + \phi_-) \\ y(t) &= -\rho_+ \sin(\omega_+ t + \phi_+) - \rho_- \sin(\omega_- t + \phi_-) \\ z(t) &= \rho_z \cos(\omega_z t + \phi_z)\ . \end{aligned} \tag{3.18}$$

From these equations one can easily obtain the instantaneous and finally the time-averaged kinetic and potential energies (see [Maj05]):

$$\begin{aligned} \bar{E} &= \bar{E}_{\text{kin}} + \bar{E}_{\text{pot}} \\ &= \frac{1}{2}m\left(\rho_+^2\omega_+^2 + \rho_-^2\omega_-^2 + \rho_z^2\omega_z^2\right) + \frac{1}{4}m\omega_z^2(\rho_z^2 - \rho_+^2 - \rho_-^2) \\ &= \frac{m}{2}\left(\rho_+^2\left(\omega_+^2 - \omega_+\omega_-\right) + \rho_-^2\left(\omega_-^2 - \omega_+\omega_-\right) + \rho_z^2\left(\omega_z^2 + \omega_+\omega_-\right)\right)\ . \end{aligned} \tag{3.19}$$

For the last step Eq. (3.15) was used. Considering $\omega_+ \gg \omega_-$ the contribution of the magnetron motion to the total energy is always negative. Therefore, a charged particle in a Penning trap is asymptotically free as its energy is minimized by an increase of the magnetron radius, which is relevant for the mass selective buffer gas cooling method, emphasized in Sect. 3.3.2.
Apart from this classical description a quantum mechanical Hamiltonian can be introduced. To this end ladder operators are used to describe the three eigenmotions. This is described in detail in [Bro86, Kre92].

3.2 Consequences of imperfections of a real Penning trap

In the previous discussion of the ion motion in a Penning trap, it was assumed that all conditions are ideal. Deviations from the ideal electric potential originate mainly from the finiteness of the electrodes, tolerances during the machining procedure and imperfections in assembling the trap. Furthermore, some electrodes are segmented to manipulate the ion motion or have holes for ion injection and ejection (see Sect. 3.3). In addition the homogeneity of the magnetic field is not infinite and the overlapping of trap axis and magnetic field lines is not perfect. In presence of these imperfections the eigenfrequencies are shifted. Here only the the most important effects are addressed. More detailed discussions are given in [Bro86, Bol96, Maj05].

Electric field imperfections

Introducing a multipolar expansion of the quadrupole potential presented in Eq. 3.2 one obtains [Gab83, Maj05]

$$U = U_0 \sum_{n=0}^{\infty} c_{2n} \left(\frac{\rho}{d}\right)^{2n} P_{2n}\cos(\theta) \tag{3.20}$$

with the coefficients c_{2n} and the Legendre Polynomials P_{2n}. Odd orders are neglected as it is assumed that they have no effect due to a radial symmetry in the mid-plane of the trap. The solution of the equations of motion results in a frequency shift as function of the motional amplitudes. Most interesting for Penning-trap mass spectrometry is the shift of the free cyclotron frequency, which is available via $\omega_c = \omega_+ + \omega_-$:

$$\begin{aligned}\Delta\omega_c^{\text{elec}} = &\frac{3\omega_z^2}{4d^2(\omega_+ - \omega_-)}(\rho_-^2 - \rho_+^2)[C_4 + \frac{5}{2d^2}C_6(\rho_+^2 + \rho_-^2 - 3\rho_z^2) \\ &+ \frac{35}{8d^2}C_8(\rho_+^4 + 3\rho_+^2\rho_-^2 - 8\rho_+^2\rho_z^2 - 8\rho_-^2\rho_z^2 + 6\rho_z^4)]\end{aligned} \tag{3.21}$$

With Eq. (3.15), $\omega_+ \gg \omega_-$ and

$$\frac{\omega_z^2}{2(\omega_+ - \omega_-)} = \frac{\omega_-}{1 - \omega_-/\omega_+} \approx \omega_- \approx \frac{U_0}{2d^2 B} \tag{3.22}$$

it is shown that the frequency shift is almost mass independent. The dependence of the amplitudes ρ in Eq. (3.21) is the result of an increased influence of the electrodes if the ion is close to them, disappearing in the trap center. Therefore, the shift can be decreased by using a larger electrode distance or a stronger magnetic field. This frequency shift is usually minimized by additional correction electrodes to make the potential more harmonic.

Magnetic field imperfections

Magnetic fields with a strength of several Tesla can only be created with a strong current flowing in superconducting coils. However, the magnetic field strength slowly decreases due to the flux-creep-effect [And62]. Apart from this effect all materials inside the field, like trap structures, insulators, vacuum chambers and even the magnet itself, induce inhomogeneities due to their non-zero magnetic susceptibility. This effect is minimized by the use of purified materials like oxygen-free copper. The additional temperature dependance of the susceptibility requires temperature stabilization of every part inside the magnetic field.
At TRIGA-TRAP this is realized with two different systems. Since the majority of the material is located in the magnet bore containing the vacuum chamber for the Penning trap structure, a temperature stabilization of this is achieved by heating up the trap tube to 30°C by a constant temperature stabilized air flow using a fuzzy logic algorithm [Mar69] that achieves a temperature stability of ±0.25°C during a day [Smo12, Wag12, Vie13].
The superconducting coils are cooled down by liquid helium. Since a change in the gas pressure inside the helium reservoir changes the boiling temperature, it has to be stabilized as well. Due to the environment in the experimental hall this is of special interest as the air pressure is kept 30 mbar below the atmospheric pressure. Thus, on top of the natural fluctuations, the experiment is sensitive on pressure drops when doors to the experimental area are opened. Stabilization is realized by a commercial system using a regulation valve and a PID controller (MKS 250E-1-D), which reduces the pressure fluctuations to less than ±0.5 mbar [Smo12, Vie13].

Similar to the electric field the magnetic field can be expressed as a multipolar expansion [Maj05]:

$$B = B_0 \sum_{n=0}^{\infty} \beta_{2n} \left(\frac{\rho}{d}\right)^{2n} P_{2n} \cos(\theta) \ . \tag{3.23}$$

Since the determined frequency in a measurement is the one-period average frequency, the dipole term vanishes. Thus the frequency shift can be expressed with the quadrupole term

as

$$\Delta\omega_c^{\text{magn}} = \frac{\omega_c \beta_2}{2(\omega_+ - \omega_-)}[(\omega_+ + \omega_-)\rho_z^2 + \omega_-\rho_+^2 - \omega_+\rho_-^2] \ . \tag{3.24}$$

Here the frequency shift is proportional to the cyclotron frequency, which requires to have the magnetic field as homogeneous as possible. At TRIGA-TRAP the magnetic field inside the trap has a homogeneity within a volume of 1 cm^3 of $\Delta B/B \leq 10^{-6}$ [Rep08]. With the present stabilization systems the magnetic field decrease is well compensated by the built-in compensation coils [Vie13] to:

$$\frac{\Delta B}{B}\frac{1}{\Delta t} = -5.36(6.94) \times 10^{-11}\,/\text{h} \ . \tag{3.25}$$

Misalignment and ellipticity of the trap

It is very important to align the trap very carefully with the magnetic field lines. The misalignment can be described by a rotation of the magnetic field with respect to the z-axis [Maj05, Kre08b]

$$\vec{B}^{\text{tilt}} = B(\sin\theta\cos\varphi, \sin\theta\sin\varphi, \cos\theta) \tag{3.26}$$

with the two polar angles $0 < \varphi \leq 2\pi$ and $0 < \theta \leq \pi$ resulting in a frequency shift. Additionally the electric potential can be distorted due to imperfections during machining the electrodes or assembling the trap. In this case the projection of the equipotential lines on the xy-plane is deformed to an ellipse. As characteristic measure for the distortion the difference of major and minor axes divided by the length of the major axis is used, called the ellipticity ε [Bro86]. In realistic experiments small tilts and tiny ellipticities can be assumed, expressed by $|\sin\theta \ll 1|$ and $\varepsilon \ll 1$. As stressed in the previous sections the major interest is in the shift of the cyclotron frequency

$$\Delta\omega_c^{\text{tilt,ellip}} \approx \omega_- \sin^2\theta(3 + \varepsilon\cos(2\varphi)) \ . \tag{3.27}$$

Even in this situation the invariance theorem Eq. (3.16) still holds due to the balancing of the radial frequency shift by the axial frequency [Bro86].

Ion-Ion interaction

So far it was always implicitly assumed that only one single ion is in the trap. If multiple ions enter the trap they interact via the Coulomb force. In the case of two different species with similar q/A ratios and the resolving power of the Penning trap being high enough, two separate resonances[1] can be observed at two distinct cyclotron frequencies ω_{c1} and ω_{c2}, which are shifted to lower frequencies. The size of the shift is proportional to the number of contaminant ions. If the resolving power is too low, the two peaks observed in the previous

[1] A resonance is the measurement of the flight time of an ion from the trap to a detector as function of the excitation frequency. This destructive time-of-flight measurement is described in detail in Sect. 3.4.2.

case merge to one broadened peak at the center-of-mass frequency. When all ions being in the trap are of the same species, no change in the cyclotron frequency is observable, but the resonance might broaden due to electric potential changes [Bol92a].
Ideally, ion-ion interaction is avoided by loading only one ion at a time into the trap for cyclotron frequency measurements or at least neglect all data points containing more than one ion at a time.
Relativistic effects occurring for ions with a high q/A ratio are not considered here since only singly-charged heavy ions are in use at TRIGA-TRAP. Also the influence of mirror charges can be neglected at the present precision level and are not considered [Van89, Por01].

3.3 Ion motion manipulation

As pointed out in Sect. 3.1 the ion motion in a Penning trap consists of three independent eigenmotions allowing to determine the ion mass. These motions can be manipulated by applying an external rf field in resonance with the corresponding eigenfrequency or one of the sidebands. Nowadays dipolar, quadrupolar and octupolar rf fields are applied in Penning traps to transfer energy to the eigenmotions, in order to excite them [Kön95, Rin07]. While the latter is only mentioned for completeness, dipolar and quadrupolar excitations are commonly in use at TRIGA-TRAP. A dipolar rf field affects selectively the eigenmotion in resonance. In contrast, a quadrupolar rf field at the sum of two eigenfrequencies couples the two corresponding eigenmotions continuously converting energy between them (see Sect. 3.3.1). Octupolar rf fields provide the possibility to convert energy between ion motions at twice the sideband frequency increasing the precision of the entire measurement [Rin07, Eli11].
Besides excitation, the cooling of motions is very important. Whenever investigations on ions are performed, large energy spreads of the ion ensemble are unfavored since they can decrease the measurement precision as well as the transport efficiency. Additionally, systematic shifts can originate from large motional amplitudes, i.e. frequency shifts in a Penning trap as discussed in Sect. 3.2. Since most of the known nuclides are short-lived they are produced in hot reactions with energies of several MeV/u and guided towards the experiment with transport energies of some keV/u. Their energy spread is removed in radiofrequency cooler and bunchers being usually on a high voltage platform as well. Most of the energy of these bunches is removed in pulsed drift tubes and finally minimized in the Penning trap.
In addition to cooling, the separation of isobaric contamination is challenging and almost not achievable with dipole magnets. The mass-selective buffer-gas cooling technique [Sav91, Kre08a] (see Sect. 3.3.2), employed at TRIGA-TRAP, offers both, efficient cooling and a high resolving power.
Other techniques for Penning-trap mass spectrometry employed at other experiments are: Evaporative cooling, resistive cooling, electron cooling, laser cooling and sympathetic cooling [Maj05, Bla06].

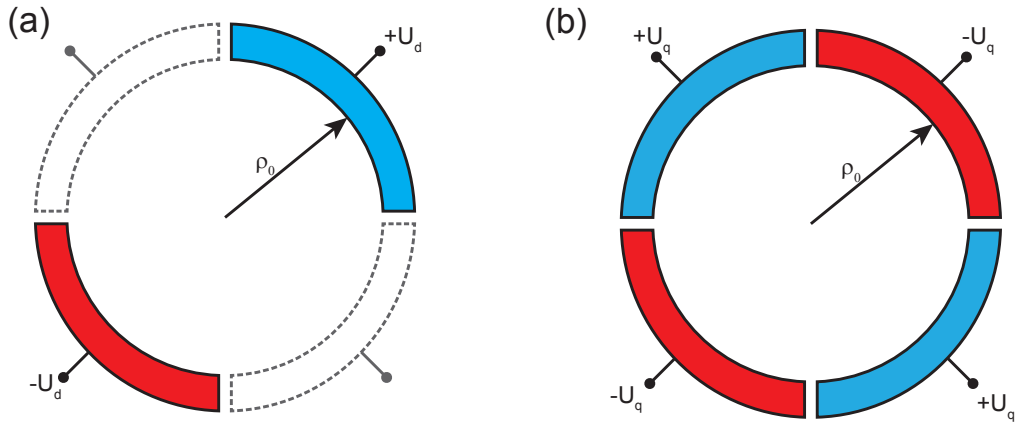

Figure 3.3: Illustration of dipolar (a) and quadrupolar (b) excitation. A radiofrequency with amplitude U_d and frequency ω_d is applied at two (a) or four (b) segments of the ring electrode. The colors indicate a 180° phase shift between rf signals applied to the according electrodes.

3.3.1 Effects of dipolar and quadrupolar excitation

For a dipolar excitation a resonant rf frequency with amplitude U_d, frequency ω_d and a 180° phase shift is applied at two opposite electrode segments as illustrated in Fig. 3.3(a). By selecting a proper frequency a certain eigenmotion can be modified individually. Since ω_+ is mass dependent, unwanted ion species can be cleaned away by exciting their modified cyclotron motion excessively. The axial motion is modified analogously by application of a dipolar field between the end cap electrodes. On the contrary, all ions are addressed in case of a ω_- excitation due to its mass independence. Thus, their magnetron radius increases simultaneously.
The dipolar rf field in x-direction can be expressed as

$$\vec{E}_x = \frac{U_d}{a}\cos(\omega_d t + \varphi_d)\vec{e}_z \ , \tag{3.28}$$

where a is the distance between ion and electrode and ω_d the excitation frequency. Choosing a proper phase the motional amplitude increases with the excitation time [Ger90, Bla03b]. If the phase of the excited motion is different from φ_d the radius of the eigenmotion is affected. For details see [Bla03b].

A quadrupolar rf field can be realized by applying an rf field with frequency ω_q to electrode segments as in Fig. 3.3(b). Between neighboring segments the phase is shifted by 180°. This way, two eigenmotions are coupled if ω_q is their sum or difference frequency. Important for mass measurements is the sideband $\omega_c = \omega_+ + \omega_-$ (Eq. (3.14)) corresponding to a coupling of modified cyclotron and magnetron motions as part of the ToF-ICR method (see Sect. 3.4.1) and the mass selective buffer-gas cooling (Sect. 3.3.2).

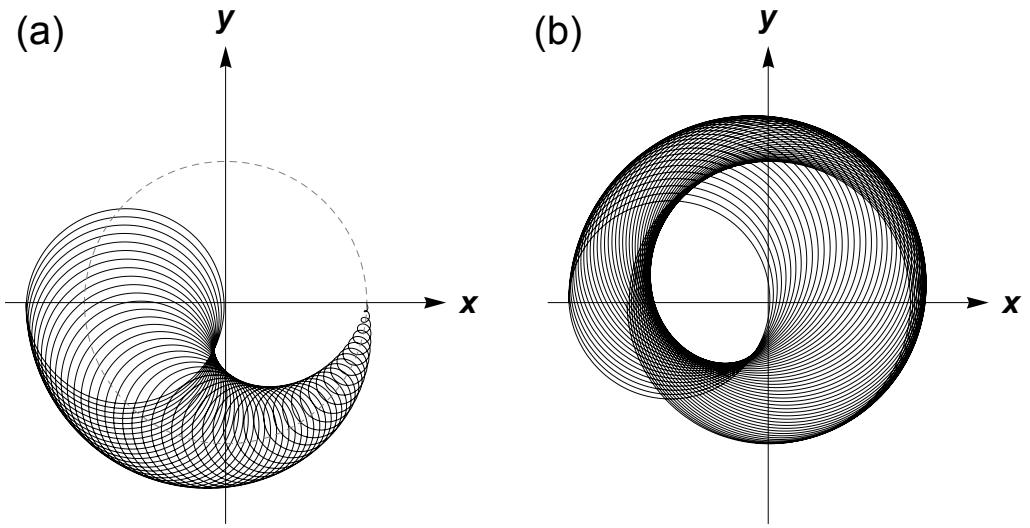

Figure 3.4: Calculated conversion of a pure magnetron to a pure modified cyclotron motion driven by a quadrupolar field with $\omega_q = \omega_c$. For better visibility first (a) and second half (b) of the conversion are drawn separately.

Similar to the dipolar field one can express the quadrupolar rf field as:

$$\vec{E}_x = \frac{2U_q}{a^2}\cos(\omega_q t + \varphi_q) y \vec{e}_x \tag{3.29}$$

$$\vec{E}_y = \frac{2U_q}{a^2}\cos(\omega_q t - \varphi_q) x \vec{e}_y \ . \tag{3.30}$$

In the interesting resonance case $\omega_q = \omega_c$, a full conversion between ρ_- and ρ_+ can be obtained, see Fig. 3.4. If only magnetron motion is present in the beginning, a full conversion to a pure modified cyclotron motion is achieved after

$$T_{\text{conv}} = \frac{2a^2\pi}{U_q}\frac{m}{q}(\omega_+ - \omega_-) \approx 2\pi a^2 \frac{B}{U_q} \tag{3.31}$$

using the relations $\omega_+ \approx \omega_c$ and $\omega_+ \gg \omega_-$. The latter indicates together with $\rho_-(t = 0) = \rho_+(t = T_{\text{conv}})$ that the total ion energy is higher after conversion due to the faster motion [Kön95].

3.3.2 Cooling of the ion motion

In the mass-selective buffer-gas cooling technique the ion motion is reduced by collision with gas, usually helium, leaking into the trap. This is described effectively by a viscous drag force [Kön95]

$$\vec{F} = -\delta m \vec{v} \tag{3.32}$$

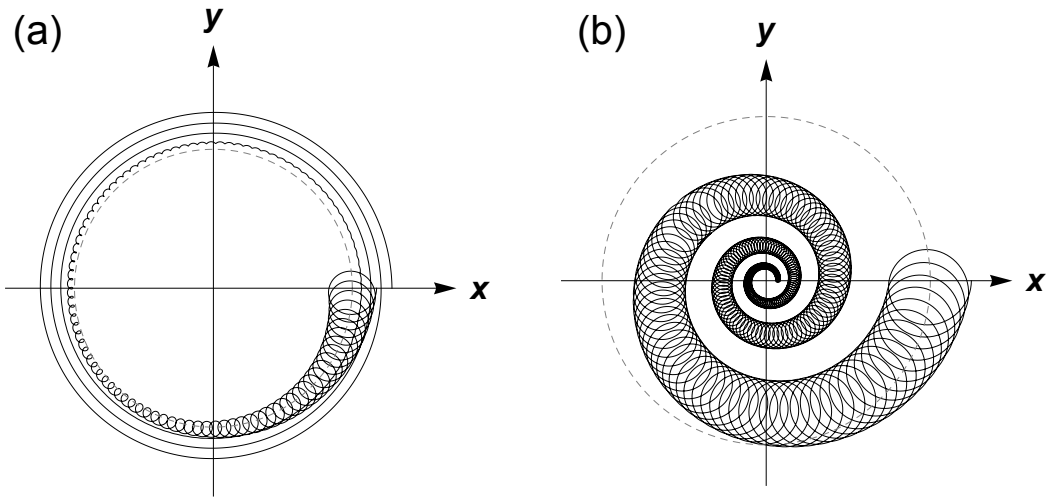

Figure 3.5: Illustration of the time development of the radial ion motions under the influence of buffer gas. Without any excitation (a) the reduced cyclotron motion is cooled very fast while the magnetron radius increases slowly. Supplementary quadrupolar excitation at ω_c (b) couples both motions. Thus, both motions are cooled and the ion is centered in the trap. The dashed line symbolizes the initial magnetron radius. For details see text.

with the momentum $m\vec{v}$ and the damping parameter

$$\delta = \frac{q}{m}\frac{1}{K_{\text{ion}}}\frac{p/p_{\text{N}}}{T/T_{\text{N}}} \ . \tag{3.33}$$

Here K_{ion} denotes the reduced ion mobility in the buffer gas with pressure p and temperature T in units of normal pressure p_{N} and temperature T_{N}. While the axial motion behaves like an ordinary damped oscillator, including exponential damping and frequency shift [Kre08a], the equations of motions are more complex for the radial motions and an exponential behavior is found:

$$\rho_{\pm}(t) = \rho_{\pm}(0)e^{\alpha_{\pm}t} \ , \tag{3.34}$$

with the damping constant [Kön95]:

$$\alpha_{\pm} = \pm\delta\frac{\omega_{\pm}}{\omega_{+} - \omega_{-}} \ . \tag{3.35}$$

The frequency shifts are negligible keeping the relation $\omega_c = \omega_{+} + \omega_{-}$ invariant [Kre08a]. Eqs. (3.34) and (3.35) show an exponential decrease of the reduced cyclotron radius and an increase of the magnetron radius, which is a consequence of its negative energy contribution. The relation $\alpha_{+}/\alpha_{-} = -\omega_{+}/\omega_{-}$ considering $\omega_{+} \gg \omega_{-}$ illustrates that the amplitude of the modified cyclotron motion is cooled faster than the slowly increasing magnetron radius (see Fig 3.5(a)).
It is possible to cool all three motions with buffer gas with the sequence implemented at

TRIGA-TRAP: First a dipolar excitation with ω_- is applied, increasing the magnetron radius of all ions due to its mass independence. After excitation it is secured that the magnetron radius is larger than the radius of an aperture at the trap exit. Subsequently magnetron motion is coupled to the modified cyclotron motion with a quadrupolar rf field of sufficient strength at frequency ω_c. In consequence of the mass dependence of this excitation the centering showed in Fig 3.5(b) only happens to ions of a certain q/A. Aside of this resonance the coupling is too weak to counteract the increasing magnetron motion. Finally the centered ions can be ejected to a second trap for the mass measurement. All unwanted ions are blocked at the aperture.
Usually the high ionization potential of helium does not favor charge exchange when working with singly charged ions. However, cooling of highly charged ions is beyond the limits of buffer gas cooling since charge exchange effects dominate. Some other applications as well disfavor the presence of gas due to damping effects. In these cases other cooling techniques have to be implemented [Bla06, Maj05].

3.4 Cyclotron frequency measurement techniques

In Penning-trap mass spectrometry a mass measurement can be carried out by the determination of an eigenfrequency or the free cyclotron frequency (see Eqs. (3.1), (3.6), (3.9)). Basically two types are foreseen at TRIGA-TRAP: destructive, where the ions are sent to an external detector, and non-destructive, where the ions are stored in the trap for repeated measurement cycles.
At TRIGA-TRAP, at the moment only the Time of Flight-Ion Cyclotron Resonance (ToF-ICR) technique [Grä80] is in use for high-precision mass measurements. It is based on the measurement of the flight time of an ion ejected from the trap to a detector as function of a quadrupolar excitation frequency. If this frequency matches the free cyclotron frequency of an ion, the flight time has a minimum (Sect. 3.4.1).
Another technique being under development is the non-destructive measurement of image currents between ring electrode segments induced by the ion oscillation. In principle it is possible to obtain all eigenfrequencies and perform a mass measurement by using a single ion (Sect. 3.4.2).

3.4.1 Destructive time-of-flight measurement

Analogous to a current oscillating in a circle, a charged oscillating particle has a magnetic moment. Here, the axial magnetic moment of an ion with charge q and mass m oscillating around the magnetic field lines with frequency ν[2] at a radius ρ is described by

$$\vec{\mu} = -q\nu\pi\rho^2\vec{e}_z = -\frac{1}{2}q\omega\rho^2 \cdot \vec{e}_z = -\frac{1}{2}m\omega^2\rho^2\frac{q}{m}\frac{1}{\omega} \cdot \vec{e}_z = -\frac{1}{2}m\omega^2\rho^2\frac{\omega_c}{B}\frac{1}{\omega}\vec{e}_z \ . \tag{3.36}$$

[2] $\omega = 2\pi\nu$

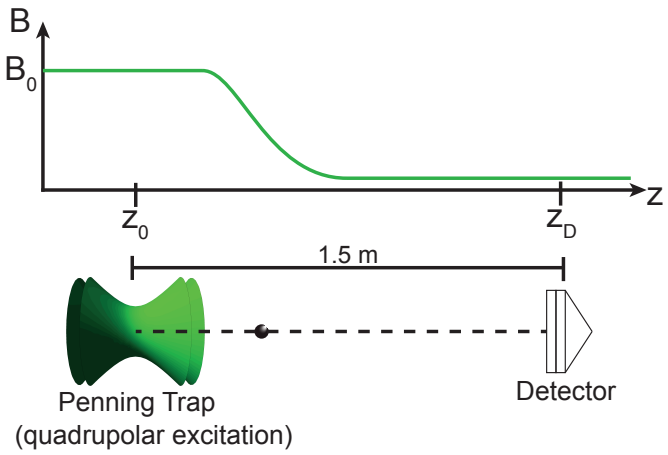

Figure 3.6: Principle of the Time-of-flight Ion-Cyclotron Resonance technique. Inside the trap the ions are prepared with a pure magnetron motion. They are excited with a quadrupolar rf field with a frequency which is varied around ν_c and subsequently sent through the magnetic field gradient to a detector. The calculated mean time of flight as function of the detuning of the frequency shows a minimum for $\nu = \nu_c$.

The relations $\omega_+ \gg \omega_-$ and $\omega_+ \approx \omega_c$ show that the major contributor to the magnetic moment is the modified cyclotron motion. Thus, using Eq. (3.19), the magnetic moment a charged particle in a trap can be approximated with

$$\vec{\mu} = -\frac{E_\mathrm{r}}{B}\vec{e}_z \tag{3.37}$$

where E_r is the radial energy. After the conversion the ions are ejected from the Penning trap to a detector located at position z_D outside the magnetic field. Since the potential energy inside the magnetic field is $E_\mathrm{mag} = -\vec{\mu}\vec{B}$, the force the particle experiences when passing through the magnetic field gradient is

$$\vec{F}_\mathrm{mag} = -\nabla E_\mathrm{mag} = -\vec{\mu}\frac{\partial B}{\partial z} = -\frac{E_\mathrm{r}}{B}\frac{\partial B}{\partial z}\vec{e}_z \tag{3.38}$$

accelerating the particle depending on its magnetic moment. In the non-resonant case $\nu_q \neq \nu_c$ the conversion is not completed and the radial energy will be smaller compared to the case when $\nu_q = \nu_c$. For an initially pure magnetron motion one obtains [Kön95, Kre07]

$$E_\mathrm{r} \propto \frac{\sin^2(\omega_R T_q/2)}{\omega_R^2} \tag{3.39}$$

with the Rabi frequency $\omega_R = \sqrt{\delta^2 + (\pi/T_q)^2}$ where δ is the frequency detuning parameter $\delta = \omega - \omega_c$. T_q denotes the conversion tine from an initially pure magnetron to a pure modified cyclotron motion. Thus, the flight time to the detector, which depends on

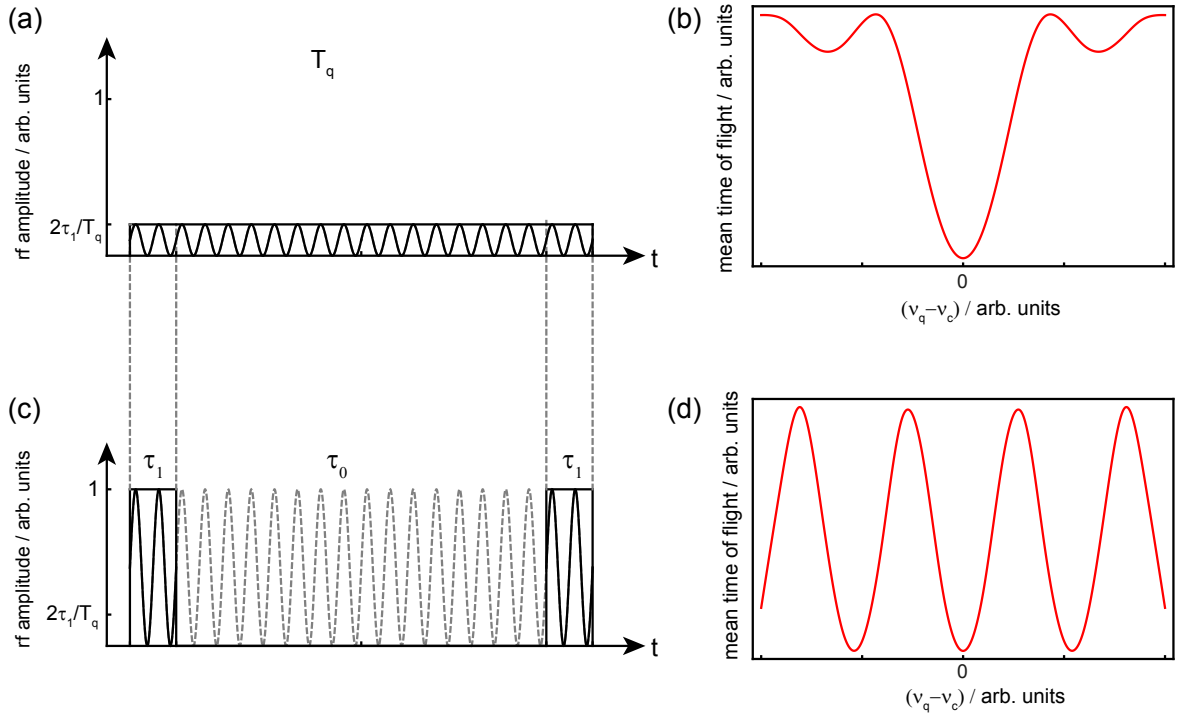

Figure 3.7: Illustration of continuous (a) and Ramsey (c) excitation with the corresponding time-of-flight spectrum (b,d). For the Ramsey excitation (lower panel), the sidebands are more pronounced and the linewidth is decreased, resulting in a higher precision. In (a) and (c) the product of U_q and the total excitation time is kept constant. For details, see text.

the amplitudes of the radial eigenmotions, is a measure for the radial ion energy and the modified cyclotron radius.
This correlation is used in a ToF-ICR measurement (see Fig. 3.6). An ideally mono-isotopic ion bunch coming from the purification trap with completely cooled radial and axial motions is trapped and its magnetron radius ρ_- subsequently increased by a dipolar excitation. Then the modified cyclotron and magnetron motions are coupled by a quadrupolar rf field. The excitation amplitude U_q and time T_q are chosen so that the conversion is completed for the resonant excitation frequency $\nu_q = \nu_c$. Now ν_q is detuned in steps around ν_c and the flight time from the trap at position z_0 to the detector at z_D is given by [Kön95]

$$T(\nu,\chi) = \int_{z_0}^{z_1} \sqrt{\frac{m}{2[E_0 - qV(z) - \mu(\nu,\chi)(B(z) - B(z_0))]}}\,\mathrm{d}z \tag{3.40}$$

with the total initial ion energy E_0, the electric field $V(z)$ and the magnetic field $B(z)$. This adds up to the resonance shape shown in Fig. 3.7(b).
Clearly, a certain number of ions is needed to record a time-of-flight resonance spectrum and to obtain the cyclotron frequency from a fit of Eq. (3.40) to the measurement data.

The statistical uncertainty of this fit is given by [Kel03]

$$s(\nu_c) \propto \frac{1}{\sqrt{N_{\text{ion}}}} \frac{1}{T_q} \tag{3.41}$$

with the number of detected ions N_{ion} and the total conversion time from magnetron to modified cyclotron motion, T_q. Thus, a longer excitation time is desired. The lentgh of the excitation is limited mainly by the pressure inside the trap, since a longer storage time increases the probability of collisions with residual gas atoms. As consequence the modified cyclotron motion is damped decreasing the time of flight difference between excited and non-excited ions and by that the overall uncertainty. For radioactive ions the half-life $T_{1/2}$ limits the time it is available for investigations. In addition the maximum time for the measurement is limited by the uncertainty due to magnetic field fluctuations [Ket10b,Vie13] limiting the product $\sqrt{N_{\text{ion}}}T_q$.
Apart from the continuous excitation, other rf patterns can be applied as well, like the Ramsey excitation [Bol92b]. Fig. 3.7 illustrates the differences between continuous and Ramsey excitation. Thereby, the excitation time is split into two pulses with a waiting time in between and the total cycle time being kept constant. A full conversion in resonance is secured by keeping the integral of the excitation constant. Introduction of the Ramsey scheme decreases the linewidth and pronounces the sidebands. Therefore, the uncertainty of the frequency measurement is decreased, gaining up to a factor of three in precision [Kre07, Geo07].
Using the two-pulse Ramsey excitation the conversion depends additionally on the phase applied between both excitation pulses:

$$\begin{aligned} F_{\text{conv}}(\delta;\tau_0,\tau_1,g,\chi) &= \frac{4g^2}{\omega_R^2}\left\{\cos\left(\frac{\omega_R\tau_0}{2}+\frac{\chi}{2}\right)\sin(\omega_R\tau_1)\right. \\ &+ \left.\frac{\delta}{\omega_R}\sin\left(\frac{\omega_R\tau_0}{2}+\frac{\chi}{2}\right)\left[\cos(\omega_R\tau_1)-1\right]\right\}^2 , \end{aligned} \tag{3.42}$$

with the frequency detuning $\delta = \omega - \omega_c$, the Rabi-frequency $\omega_R = \sqrt{\delta^2 + 4g^2}$ and the conversion factor $g = \pi/(4\tau_1)$. χ denotes the phase shift of the second excitation pulse relative to the first one [Kre07]. According to Eq. (3.42), the phase χ affects the conversion probability F_{conv} and therefore the magnetic moment of the ions. Thus, the fringes of the TOF spectrum move with the phase shift. The time of flight is minimal at the cyclotron frequency ν_c if the phase shift is 0 or an even multiple of π and maximal with odd multiples of π, whereas with a phase shift of odd multiples of $\pi/2$ the resonant frequency is at an inflection point of the spectrum [Eib10b].

At TRIGA-TRAP the Ramsey excitation scheme shown in Fig. 3.7(c) was applied to record the data presented in Chap. 6 with a pulse length $\tau_1 = 0.2\,\text{s}$ and waiting time $\tau_0 = 1.6\,\text{s}$.
Eq. (3.1) shows that after the measurement of ν_c the magnetic field B is still unknown.

Since NMR Probes are too imprecise this is done by measuring the cyclotron frequency $\nu_{c,\mathrm{ref}}$ of a reference ion of well-known mass. Then the atomic mass of a nuclide is

$$m_{\mathrm{atom}} = \frac{\nu_{c,\mathrm{ref}}}{\nu_c}(m_{\mathrm{ref}} - m_e) + m_e \ , \tag{3.43}$$

where m_{ref} denotes the mass of a singly charged reference ion and m_e the electron mass. As already pointed out the electric field imperfections (Eq. (3.21)) and trap misalignment in the magnetic field (Eq. (3.27)) induce a mass independent frequency shift. Including a shift into Eq. (3.43) one obtains for small frequency shifts $\Delta\nu_c$ with

$$\begin{aligned} \Delta m_{\mathrm{atom}} &= \frac{\nu_{c,\mathrm{ref}} + \Delta\nu_c}{\nu_c + \Delta\nu_c}(m_{\mathrm{ref}} - m_e) + \overbrace{m_e - m_{\mathrm{atom}}}^{=-\frac{\nu_{c,\mathrm{ref}}}{\nu_c}(m_{\mathrm{ref}}-m_e)} \\ &= \frac{\Delta\nu_c(\nu_c - \nu_{c,\mathrm{ref}})}{(\nu_c + \Delta\nu_c)\nu_c}(m_{\mathrm{ref}} - m_e) \\ &= \frac{\Delta\nu_c}{\nu_c + \Delta\nu_c}(m_{\mathrm{ref}} - m_{\mathrm{atom}}) \end{aligned} \tag{3.44}$$

the relative mass shift

$$\begin{aligned} \frac{\Delta m_{\mathrm{atom}}}{m_{\mathrm{atom}}} &\approx \frac{\Delta\nu_c}{m_{\mathrm{atom}}\nu_c}(m_{\mathrm{ref}} - m_{\mathrm{atom}}) \\ &\propto (m_{\mathrm{ref}} - m_{\mathrm{atom}}) \ , \end{aligned} \tag{3.45}$$

which is proportional to the difference of the reference mass and the mass of the ion of interest [Bol96]. Thus, it is generally favorable to measure the frequency ratio of mass doublets [Lin91]. Recently carbon clusters $^{12}\mathrm{C}_\mathrm{n}, \mathrm{n} \in \mathbb{N}$ became available at TRIGA-TRAP using a laser ablation ion source [Smo08] being the ideal reference since the atomic mass is defined by $1/12^{\mathrm{th}}$ of the mass of ^{12}C. Moreover, carbon clusters are available as reference mass all over the nuclide chart providing a reference every 12 mass units [Bla02].
Since carbon clusters provide a comb of well-known masses, systematic uncertainties can be investigated by measuring their frequency ratios. The proportional constant from Eq. 3.45 can be determined enabling a consideration of the relative mass-shift as function of the mass difference of reference ion and ion of interest. Applying the method from ISOLTRAP [Kel03] this was extensively studied at TRIGA-TRAP [Ket10b] and will be briefly addressed in Chap. 6.

3.4.2 Non-destructive image current measurement

As already mentioned an ion oscillating inside a Penning trap induces image currents in the surfaces of the electrodes. This perturbes the electric field additionally to the effects discussed in Sect. 3.2. In general they should be considered [Van89, Gro91, Xia93]. However, at TRIGA-TRAP this effect is negligible since it the trap is comparably large and

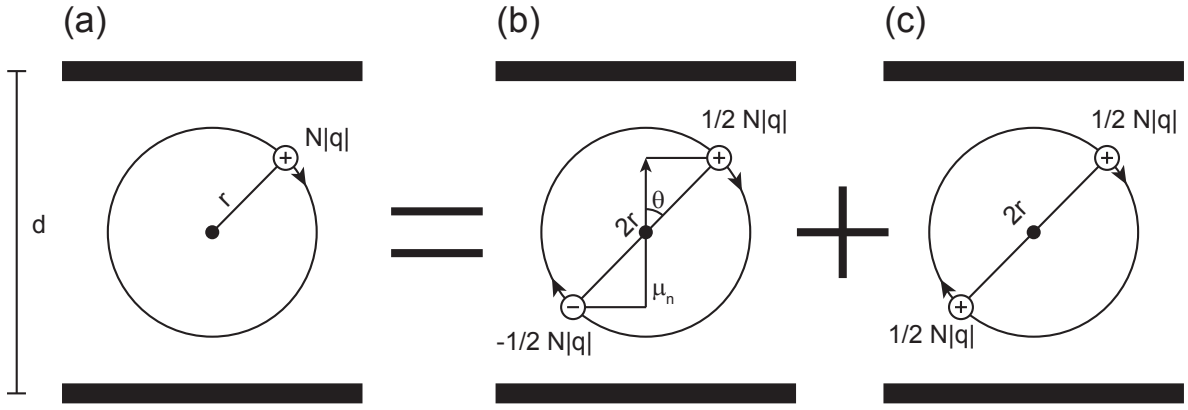

Figure 3.8: Simplified description of an coherently oscillating ion cloud in the trap whose segments are approximated as parallel plates (a). The superposition of electric potentials allows the decomposition into a dipole (b) and two monopoles (c). For further details see text.

additionally only singly charged ions are available. The approach of [Com78] is briefly discussed here.

It is assumed that N ions carrying charge q rotate in the Penning trap with the ring electrode segments being approximated as parallel plates having the surface A separated by distance d. In Fig. 3.8 the magnetic field is directed out of the plain so that positive ions oscillate clockwise. Due to the superposition of electric potentials, it is possible to substitute the rotating monopole in Fig. 3.8(a) by one dipole, Fig. 3.8(b), and two monopoles, Fig. 3.8(c). The latter does not have any differential effect on the plates since their signals cancel each other. The electric dipole is represented by an electric dipole moment normal to the plates

$$\mu_n = Nqr\cos\theta \ . \tag{3.46}$$

Since the ions are oscillating with $\theta(t) = 2\pi\nu t + \varphi$, where ν denotes the oscillation frequency and φ the phase, the charge density σ on the top plate is given by

$$\sigma(t) = -\frac{\mu_n}{V} = -Nq\frac{r}{Ad}\cos\left(2\pi\nu t + \varphi\right) \ . \tag{3.47}$$

The negative sign indicates a negative image charge. This obviously leads to the total charge on the top plate

$$Q(t) = \sigma A = -Nq\frac{r}{d}\cos\left(2\pi\nu t + \varphi\right) \tag{3.48}$$

and further to the image current

$$I(t) = \dot{Q}(t) = 2\pi\nu Nq\frac{r}{d}\sin\left(2\pi\nu t + \varphi\right) \tag{3.49}$$

with the effective value

$$I_{\text{eff}} = \sqrt{2}\pi\nu N q \frac{r}{d} \ . \tag{3.50}$$

The frequency of the ion can now be accessed from Eq. (3.49) as function of q, N and r/d by Fourier transformation. Analogous to hyperbolic and cylindrical Penning traps, the spacing parameter d has to be modified for image current calculations using ring shaped electrodes.
Since the magnetron frequency is not mass-dependent the mass has to be determined via the modified cyclotron frequency. Thus its amplitude is increased by a dipolar excitation at ν_+. Looking at Eq. (3.9) it is clear that two parameters, U_0 and B, hidden in ω_z and ω_c, have to be calibrated, requiring two reference nuclides of different masses. Some simple transformations return

$$\frac{q}{m} = \frac{\nu_+}{a\nu_+ - b} \tag{3.51}$$

with $a = B_0/(2\pi)$ and $b = U_0/(8\pi^2 d^2)$. Analogous to Eq. (3.43) one obtains the atomic mass as function of two reference ions with masses $m_{1,\text{ref}}, m_{2,\text{ref}}$ and their corresponding calibration frequencies $\nu_{1,+}, \nu_{2,+}$ [Ket10a]:

$$m_{\text{atom}} = \left[\frac{\nu_{1,+}^2(\nu_+ - \nu_{2,+})}{\nu_+^2(\nu_{1,+} - \nu_{2,+})}(m_{1,\text{ref}} - m_e) + \frac{\nu_{2,+}^2(\nu_{1,+} - \nu_+)}{\nu_+^2(\nu_{1,+} - \nu_{2,+})}(m_{2,\text{ref}} - m_e)\right] + m_e \ . \tag{3.52}$$

Principle of single ion detection

Ideally Penning-trap mass spectrometry requires only one single ion in the trap. The main reason is to completely avoid ion-ion interaction and resulting frequency shifts as discussed in Sect. 3.2 as well as minimizing the influence of the image charges.
If the ion oscillates in the trap a voltage drop could be measured at a resistor in the connection between two opposing trap segments. According to Ohm's law $U = RI$ a high resistance could make the voltage drop measurable with regular multimeters. However, capacitances C limit the total impedance to $(\omega C)^{-1}$. This limitation can be canceled out by a compensation with a well-chosen inductance creating a tank circuit with the trap.
Real inductances usually have a finite resistance R_s in series with L_s. This can be easily transformed to its parallel equivalent R_p via the parallel and serial impedances with $Z_\text{p} = Z_\text{s}$ by comparison of their real and imaginary parts

$$Z_\text{s} = R_\text{s} + \text{i}\omega L_\text{s} \ , \tag{3.53}$$

$$Z_\text{p}^{-1} = R_\text{p}^{-1} + (\text{i}\omega L_\text{p})^{-1} \tag{3.54}$$

to

$$R_\text{p} = R_\text{s}\left(1 + \left(\frac{\omega L_\text{s}}{R_\text{s}}\right)^2\right) \tag{3.55}$$

$$L_\text{p} = L_\text{s}\left(1 + \left(\frac{R_\text{s}}{\omega L_\text{s}}\right)^2\right) \ . \tag{3.56}$$

All coils used in narrow-band FT-ICR detection systems are designed to have a very high inductance. Therefore, $\left(\frac{\omega L_\mathrm{s}}{R_\mathrm{s}}\right)^2 \gg 1$ is assumed from here on. Thus, with the definition of the quality factor of the coil,

$$Q = \frac{\omega L}{R_\mathrm{s}} \tag{3.57}$$

and Eqs. (3.55) and (3.56) it is found that $L_\mathrm{s} = L_\mathrm{p} \equiv L$ and the coils equivalent parallel resistance is simplified to

$$R_\mathrm{p} = Q \cdot \omega L \ . \tag{3.58}$$

The tank circuit, consisting of the coil and the trap, is tuned to the revolution frequency of the ion. Then the resulting total impedance is

$$Z(\omega) = \left[\frac{1}{R_\mathrm{p}} + \mathrm{i}\left(\omega C_{tot} - \frac{1}{\omega L}\right)\right]^{-1} \ . \tag{3.59}$$

Where C_{tot} is the capacitance of the detection system determined by the capacitance of the trap C_T, parasitic capacitances C_p and the input capacitance of the amplifier C_{amp} being coupled to the tank circuit by C_{coupl}:

$$C_{tot} = C_T + C_p + \frac{C_{amp}}{\zeta} \tag{3.60}$$

with the coupling parameter

$$\zeta = \gamma \frac{C_{coupl} + C_{amp}}{C_{coupl}} \ . \tag{3.61}$$

Here, γ denotes the winding ratio where the first amplifier is coupled to the inductance. At the resonance frequency

$$\omega_{LC} = \frac{1}{\sqrt{LC_{tot}}} \tag{3.62}$$

capacitive and inductive contributions vanish leaving R_p as the only contributor to the total impedance. Simple calculations involving Eq. (3.58) and (3.62) yield the absolute value of the impedance and the resonant parallel resistance

$$R_\mathrm{p} = Q\omega_{LC}L = \frac{Q}{\omega_{LC}C_{tot}} \tag{3.63}$$

$$|Z(\omega)| = \frac{Q\omega L}{\sqrt{1 + Q^2\left(\frac{\omega^2}{\omega_{LC}^2} - 1\right)^2}} \ . \tag{3.64}$$

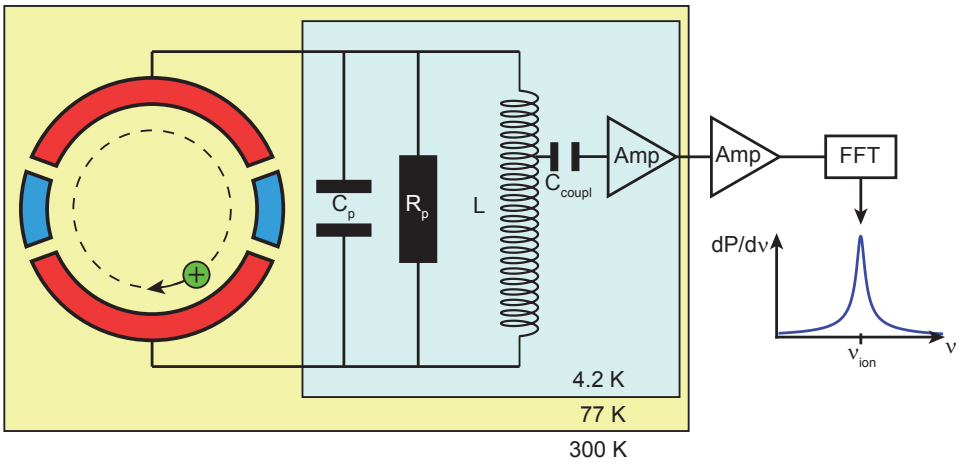

Figure 3.9: Principle of narrow-band FT-ICR detection at TRIGA-TRAP. The oscillating ion induces an image current between two ring electrode segments (red). The tank circuit is tuned to the revolution frequency of the ion acting as a band pass filter for noise suppression. The parasitic capacitance C_p and resistance R_p are no concrete parts. They just exist due to the trap and the coil with inductance L. Additional noise sources are current noise from thermal effects and the first amplifier as well as voltage noise from both amplifiers. Thermal noise is reduced by cooling the trap and the detection circuit to 77 K and 4 K, respectively.

For large Q the width of the resonance $\Delta\omega$ within which the voltage across the tank circuit drops to $1/\sqrt{2}$ of the maximum is

$$\Delta\omega = \frac{\omega_{LC}}{Q}. \tag{3.65}$$

These equations illustrate that a high quality factor of the coil as well as an overall small capacitance are favored to reach high parallel resistances leading to high amplification factors. Noise suppression is especially supported by a high Q resulting in narrow resonances.

The principle of narrow-band FT-ICR detection is displayed in Fig. 3.9. The voltage signal is guided to the first, cryogenic amplifier via a galvanic coupling to the coil (coil tap).

Furthermore, the prior considerations allow an estimation of the signal-to-noise ratio. The voltage drop at the parallel resistance R_p and the effective image current I_eff (see Eq. (3.50)):

$$U = R_\mathrm{p} I_\mathrm{eff} \zeta^2 \tag{3.66}$$

manifests as a peak on top of the noise spectrum of the tank circuit. The total noise after amplification is determined by the thermal noise [Joh28, Nyq28] e_th, voltage e_amp and

current noise i_{amp} of the amplifier [Kra12]:

$$e_{\mathrm{tot}}^2 = e_{\mathrm{th}}^2 + e_{\mathrm{amp}}^2 + i_{\mathrm{amp}}^2 R^2 \zeta^2 \ , \tag{3.67}$$

with

$$e_{\mathrm{th}} = \sqrt{4 k_{\mathrm{B}} T R \zeta^2} \tag{3.68}$$

where k_{B} denotes the Boltzmann constant and T the temperature. Since the current noise is damped by ζ due to the coupling between tank circuit and amplifier, the last summand is neglected, yielding

$$e_{\mathrm{tot}}^2 = e_{\mathrm{th}}^2 + e_{\mathrm{amp}}^2 \ . \tag{3.69}$$

This results in the signal-to-noise ratio

$$\left(\frac{S}{N}\right)^2 = \frac{(R_{\mathrm{p}} I_{\mathrm{eff}} \zeta^2)^2}{4k\mathrm{B}TR\zeta^2 + e_{\mathrm{amp}}^2} \ . \tag{3.70}$$

Due to the Johnson noise the signal-to-noise ratio can be increased by working at lower temperatures, which is realized at TRIGA-TRAP by cooling the amplifier and the trap down with liquid helium and liquid nitrogen, respectively. At TRIGA-TRAP the effect of the temperature is even stronger than Eq. (3.70) implies. Since a superconducting coil is used, the serial resistance decreases and thereby the Q-Value increases significantly when the transition temperature is reached. The effective ion current hides a proportional behavior as function of the ion amplitude. However, an increase of the ion motion is performed at expense of precision since the ion experiences more field imperfections. In addition it is important that the first amplifier provides a high gain combined with a low voltage noise to suppress additional noise sources.
Nevertheless, the here presented signal-to-noise ratio is only an upper limit. Noise created by voltage sources providing the trap potentials can be extremely disturbing and hamper the entire measurement. Equally disturbing are unchielded cables acting as antennas which could couple unwanted signals into the detection systems. Further details on the FT-ICR system as well as latest developments are presented in Sect. 4.5 and Chap. 5.

Chapter 4

The double Penning-trap mass spectrometer TRIGA-TRAP

The double Penning-trap mass spectrometer TRIGA-TRAP was put into operation in 2008 as part of the TRIGA-SPEC experiment, dedicated to the measurements of nuclear ground-state properties of actinoides and short-lived neutron-rich nuclides [Ket08]. They are provided by the research reactor TRIGA Mainz, being produced by thermal neutron-induced fission of actinoid material placed close to the reactor core. Their extraction from the reactor, ionization, mass-separation and bunching is discussed in Sect. 4.1. Subsequently, the ions are guided either to TRIGA-TRAP or to the collinear laser spectroscopy beamline TRIGA-LASER. A detailed floorplan of TRIGA-SPEC is shown in Fig. 4.1.
At TRIGA-LASER the ion beam is overlapped collinearly or anticollinearly with a laser beam. The ions have typically energies of 30 keV. Due to the quadratic scaling of the energy as function of the ion velocity, the velocity spread is compressed at higher energies as the energy spread is conserved. This concept provides the possibility to use fixed-frequency lasers and tune the accelerating voltage to vary the Doppler shift. Thereby ion transitions are tuned to resonance with the laser light. If transitions in the ionic spectrum are disadvantageous, the ions are neutralized in an alkali vapour to perform laser spectroscopy on neutral atoms. The properties that can be studied are nuclear spin, magnetic moment, spectroscopic quadrupolar moment, and the difference of mean-square nuclear charge radii between isotopes, which are available via isotope shifts and hyperfine structure measurements [Ott89, Klu03, Ket08].
At TRIGA-TRAP mass measurements of ions in a Penning trap can be performed with relative uncertainties of typically 10^{-8} (see Chap. 3 and Sect. 4.4). Two different techniques with different limitations enable mass measurements of either short-lived or rarely produced species [Ket08, Ket09a].
Additionally TRIGA-TRAP as well as TRIGA-LASER serve as test benches of MATS and LaSPEC within NUSTAR at FAIR [Rod10], where the border of available radionuclides will be pushed further away from the valley of stability.

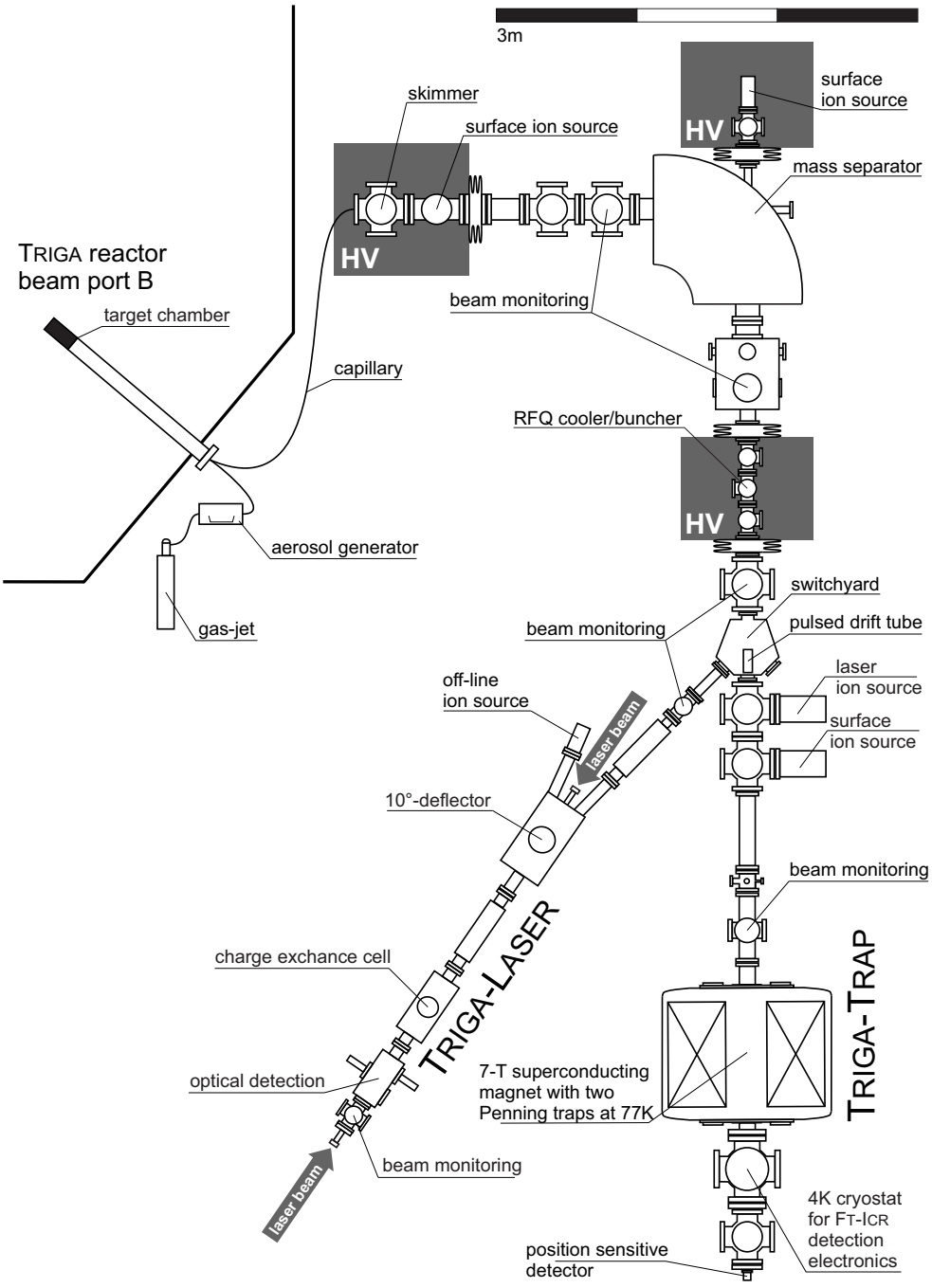

Figure 4.1: TRIGA-SPEC layout. Neutron-rich nuclides are produced close to the reactor core by thermal neutron-induced fission. After ionization, e.g. on a hot surface, they are mass-separated and subsequently cooled and bunched. These bunches are either transported to the mass spectrometer TRIGA-TRAP or to the collinear spectroscopy beamline TRIGA-LASER.

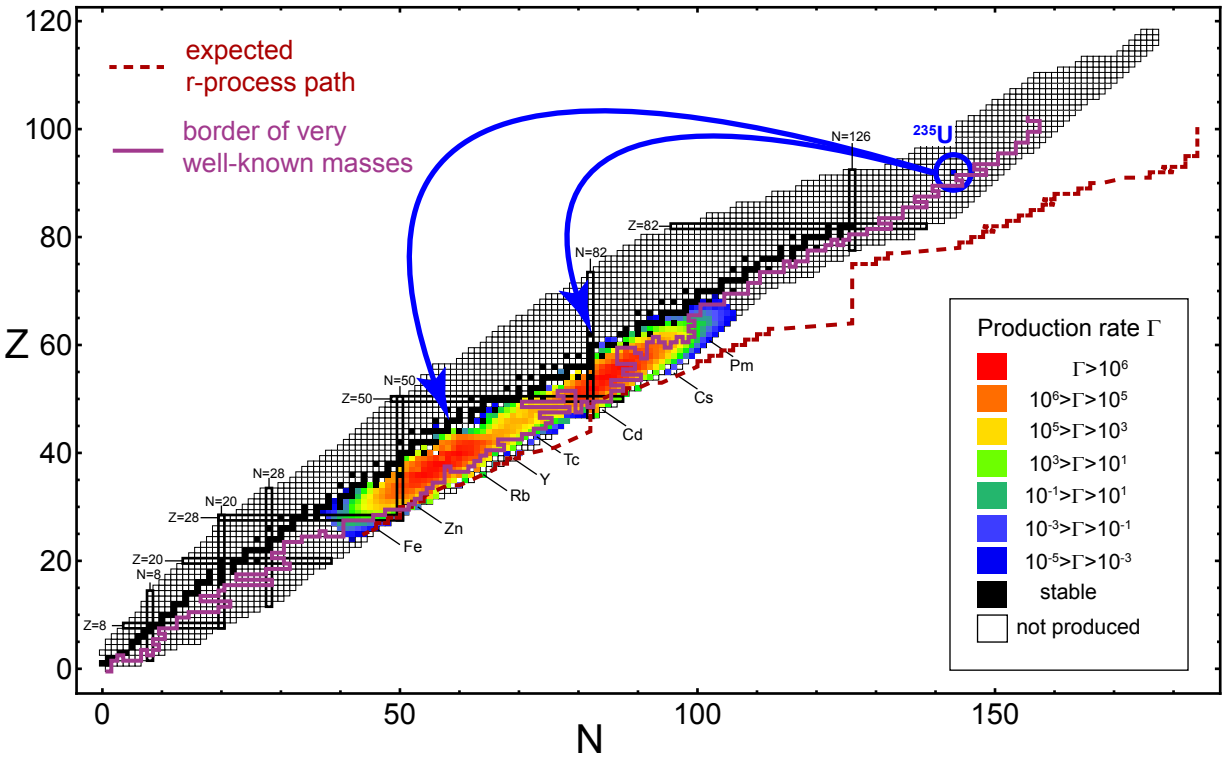

Figure 4.2: Production rates at TRIGA-SPEC. With the experimentally determined fission yields [Eng94, LBN] and the conditions at the TRIGA reactor ($300\,\mu$g ^{235}U, 1.8×10^{11}n/(cm^{2}s)) the production rate is calculated. To illustrate possible contributions of TRIGA-TRAP the border beyond which the mass uncertainty is larger than 10 keV is plotted [Wan12]. However, the expected r-process path is only very limited within reach [Pfe11].

4.1 On-line ion production and beam preparation

The short-lived radionuclides studied at TRIGA-SPEC are produced at the research reactor TRIGA Mainz. Its fuel material uranium, which is enriched to about 20% ^{235}U, is embedded in a ZrH matrix. Here, the majority of neutrons are slowed down by the hydrogen in the fuel elements, having a decreasing moderation ability with increasing temperature. This enables the nifty feature of overcritical operation: When the control rods are removed rapidly the suddenly increased amount of neutrons starts a chain reaction of promptly emitted and moderated neutrons. This is only stopped due to the temperature increase of the fuel elements, stopping the reaction within milliseconds. In these so-called pulsed mode the maximum reachable thermal power is 250 MW with a pulse FWHM of 30 ms, whereas steady state operation provides maximum 100 kW thermal power [Ebe00, Ham06]. Beam tubes in the biological shield of the reactor provide access to a region with high neutron

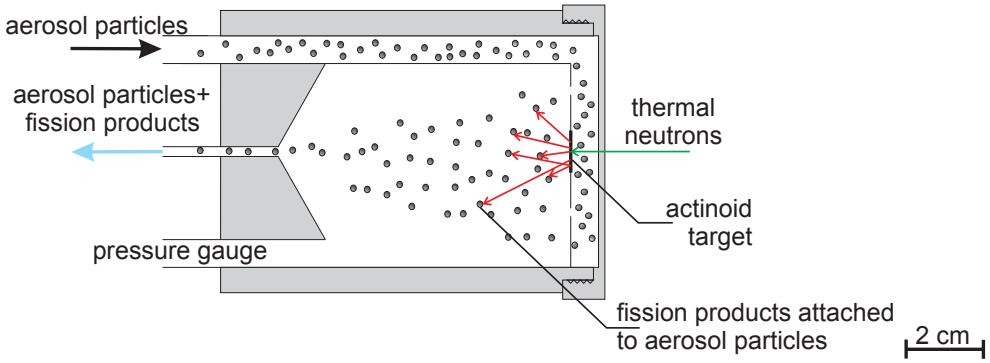

Figure 4.3: Sketch of the target chamber. A carrier gas seeded with aerosol particles is continuously flushed through the target chamber. Fission products are thermalized by the gas. Their mean free path is controlled by the gas pessure. Afterwards the radionuclides attach to the aerosol particles which are flushed out of the chamber.

flux. At beam port B, being reserved for TRIGA-SPEC (see Fig. 4.1) a neutron flux[1] of about $\Phi_n = 1.8 \cdot 10^{11}$ n/(cm^{2}s) is available in steady state and approximately a factor of 2500 more in pulsed operation.
At TRIGA-SPEC usually a sample of ^{235}U, ^{239}Pu or ^{249}Cf is irradiated. The individual fission yields taken from [Eng94, LBN] lead to the production rates $\Gamma(Z, N)$ of radionuclides. Assuming 300 μg material the results presented in Fig. 4.2 are obtained by

$$\Gamma(Z, N) = \sigma_f \Phi_\mathrm{n} N_\mathrm{target} \xi_i(Z, N) \ . \tag{4.1}$$

Here N_target denotes the number of fissionable atoms with the fission cross section σ_f and the individual production probability of each nuclide $\xi_i(Z, N)$ [Eng94, LBN]. It will be possible for TRIGA-TRAP to provide improved mass data in the neutron-rich regime, indicated by the dark red line beyond which no mass is known with an uncertainty below 10 keV [Wan12]. Even the expected r-process path is reachable around the magic numbers [Pfe11]. Obviously the mass distribution is assymmetric for thermal neutron-induced fission [New61]. For the here presented case, the production maxima are around $A = 100$ and $A = 138$, which is around the magic numbers $Z = 50$ and $N = 82$. Fission yields demonstrate that the light fission branch shift towards heavier masses for heavier feed material, while the heavy branch remains in position until symmetric fission is dominating for ^{258}Fm [Eng94].
Extraction of fission products is carried out by a gas-jet system whose principle was well-characterized in radiochemistry experiments [Mac69]: First a carrier gas, typically He, Ar or N_2, is seeded with aerosol particles. Different materials have been investigated so far, whereas carbon and KCl aerosols are commonly in use at TRIGA-SPEC [Eib09, Smo12]. First tests for fission product extraction were performed with carbon aerosol particles. Their production takes place when the carrier gas is guided through a chamber where a

[1] From now on this number is alway used, when TRIGA-TRAP specific neutron fluxes are required.

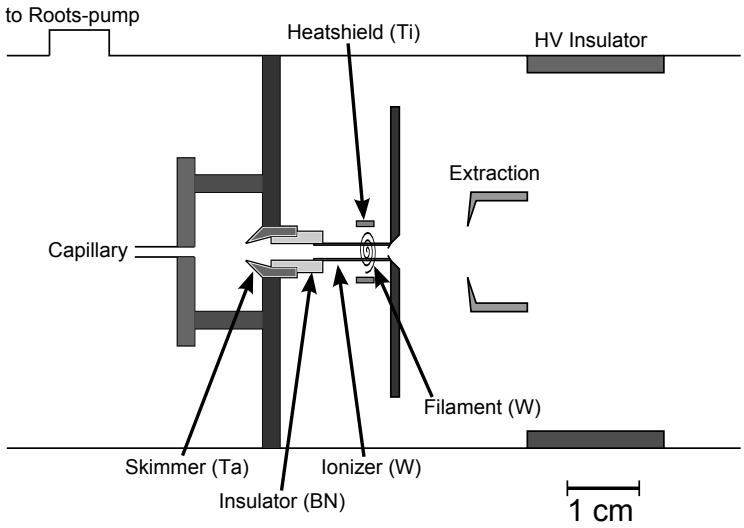

Figure 4.4: Principle of the TRIGA-SPEC on-line ion source. Aerosol particles with attached fission products are separated from the carrier gas by a skimmer. Afterwards they touch a hot tungsten surface where ionization takes place for alkali ions.

voltage of typically 1.5 kV is applied between two graphite tips. The actual formation of carbon aerosol particles with a lognormal size distribution around 100 nm takes place in a spark discharge between the tips. For a more detailed discussion see [Eib09].
Salt aerosol particles, e.g. KCl, are also commonly produced guaranteeing a reliable extraction from the reactor [Gün93] as already used in Mainz at the HELIOS experiment [Maz80]. The salt is heated inside a furnace to about 660 °C, about 100 °C below the melting point. When the carrier gas is guided through the furnace KCl sublimates from the surface clustering to particles with a lognormal distribution around 200 nm by condensation and coagulation [Gün93].
The radionuclide production takes place inside a gas-filled recoil chamber displayed in Fig. 4.3. Its shape has been optimized for a maximum extraction ending up with a conical shape [Brü83]. To be available for extraction the fission products, being created with approximately 100 MeV kinetic energy, have to be thermalized within this small volume. Stopping powers of different gases in the target chamber were studied in [Zud86]. At TRIGA-SPEC, 2.7 bar He and 2 bar Ar or N_2 absolute pressure were used together with the target being covered with a 13 μm thick Al foil, which slows down the light fission branch and completely blocks the heavy one [Fin51].

In a test setup the extraction time, defined as the time between the pulse and the arrival of half of the maximum activity to a γ-detector, was determined in pulsed operation mode to be (390 $\pm$ 90) ms [Eib10a]. Since the pressure in the target chamber depends on length and diameter of the capillary, which change its flow resistance, the extraction time might vary under experimental conditions. This limits mass measurements on radionuclides with half-lives down to 200 ms by the ToF-ICR technique depending on their production rate. Since the FT-ICR technique is anyhow limited to nuclear half-lives of several seconds. It

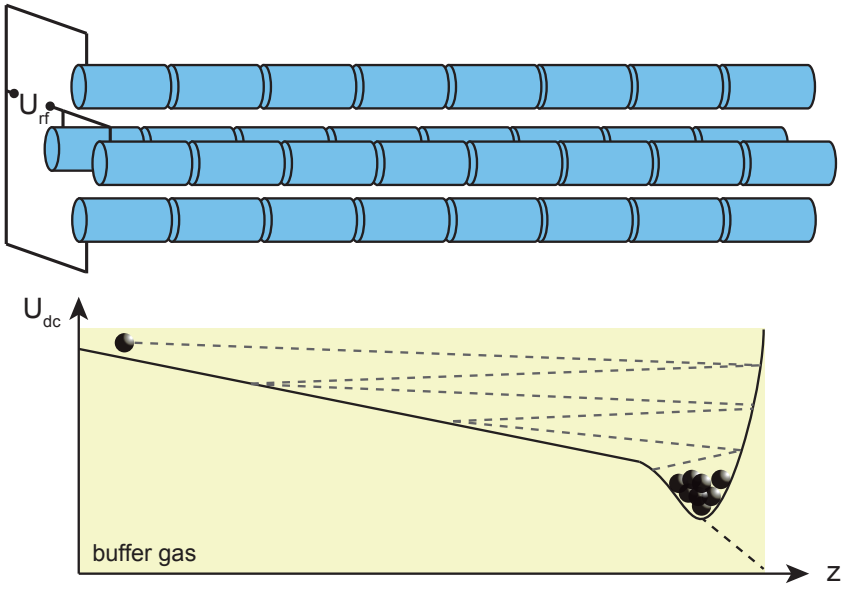

Figure 4.5: Principle of an RFQ cooler and buncher. Ions enter the trapping region, where radial confinement is achieved by an rf potential. The ions are axially trapped by a dc potential guiding the ions to a potential well at the end of the electrode structure, while they loose energy by collisions with the buffer gas. The cooled ions are ejected in a bunch by switching the rear electrodes.

is more crucial to obtain high extraction efficiencies to be able to detect even the least produced nuclides. Here, transport efficiencies between 50 and 80 % were determined with carbon and salt aerosol particles in different gases [Brü79, Brü83, Eib09]. This has been realized by the comparison of specific γ-lines of certain nuclides, which were collected on a filter placed inside the target chamber, and in a subsequent measurement behind the capillary.

The gas-jet is guided from the target chamber directly to a skimmer in front of the ion source, where the heavy aerosol particles are separated from the carrier gas, which is pumped away by a roots pump. When the gas-jet enters the vacuum, it expands rapidly, forming a Mach cone. Inside this the interaction-free so-called zone of silence is formed containing the aerosol particles [Sco89]. A conical skimmer, being placed inside the zone of silence, allows transmission of the aerosol particles while gas atoms are suppressed [Cam84, Smo12]. At TRIGA-SPEC skimmer efficiencies of about 20 % were obtained. Better transmission is expected by using an aerodynamic lens in front of the skimmer for better preparation [Liu95a, Liu95b, Gru14].

Ionization takes place immediately behind the skimmer in an ion source (see Fig. 4.4), which is a further development of the one used at the HELIOS separator [Brü85, Ren14]. A tungsten tube, thermally isolated from the skimmer by a boron nitrite insulator, is heated indirectly by electron bombardment with a power of about 800 W to about 3000 K. All atoms, with a sufficiently low ionization potential Φ_i, which come in contact with the hot

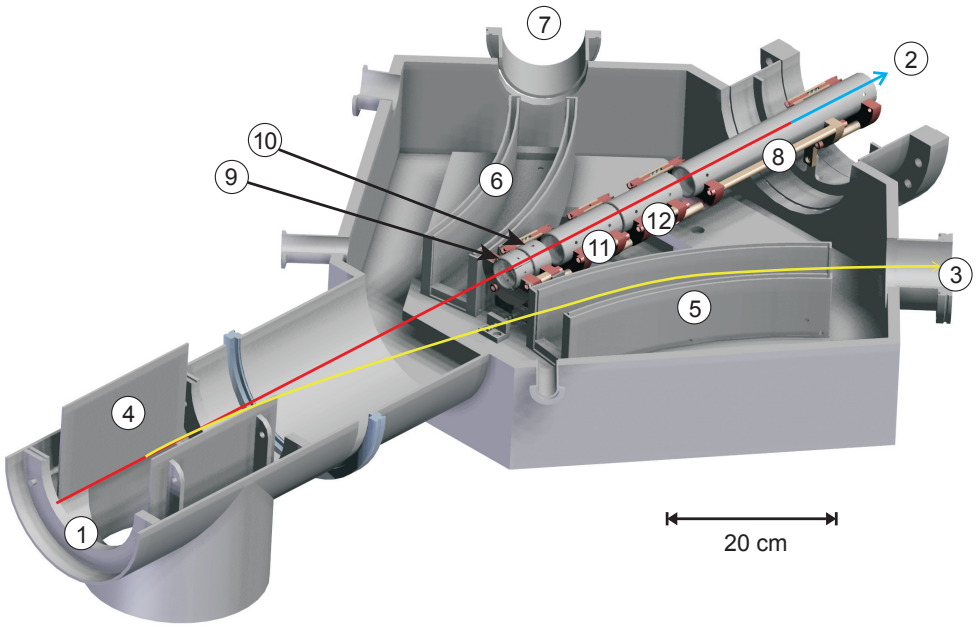

Figure 4.6: Sketch of the TRIGASPEC switchyard taken from [Smo12]. Ion bunches arriving from the buncher at (1) are either bent to TRIGA-LASER (3, yellow) with 30 keV or guided straight towards TRIGA-TRAP (2) with 30 keV (red) or 1.1 keV (blue). Bending towards TRIGA-LASER is achieved by plain (4) and subsequent curved parallel plate deflectors (5). For TRIGA-TRAP the ion beam can be pulsed down to 1.1 keV using a pulsed drift tube (8) preceded by one deflector (9) and drift tube (10).

surface are ionized with a probability p_i. Positive ionization is described by the Langmuir-Saha equation [Lan25]

$$p_i = \frac{n_i}{n_i + n_a} = \left(1 + \frac{g_a}{g_i} \exp\left[-\frac{e\Phi_i - W_s)}{k_B T}\right]\right)^{-1} , \tag{4.2}$$

where n_i and n_a denote the number of ions and atoms leaving the surface at temperature T. The parameters g_i and g_a are the degeneracy of the ionic and atomic state given by $2J + 1$. Preferable for the hot surface is tungsten due to its high work function of about $W_s = 4.6\,\text{eV}$ [Alt93] and the high melting point. However, an ionization efficiency close to 100 % can only be reached for alkali elements, while all other elements are not ionized very efficiently. Also too high temperatures are not favored since the atoms won't reach a thermal equilibrium with the surface before evaporation, thus lowering the efficiency as well. To this end, a second source based on plasma ionization is under development at TRIGA-SPEC [Sch15]. Both ionization techniques provide separation of aerosol particles and fission products.

According to Fig. 4.1 ionization takes place on a high potential platform of typically 30 kV. The created ions are extracted in a continuous beam towards ground potential and mass separated in a 90° bending magnet. Its maximum field strength $B = 1.12\,\text{T}$ and

bending radius of 0.5 m allow for isotopic separation with the help of slits in the focal plane resulting in a resolving power of $m/\Delta m \approx 200$. Subsequently, the ions are stored in a radiofrequency cooler and buncher (for the RFQ principle, see Fig. 4.5), which was previously in use at MISTRAL [Lun09]. Since the ions have kinetic energies of several keV the RFQ is on the same potential as the ion source. Thus, they are completely stopped inside the potential well loosing energy due to interaction with the background gas and are finally stored in an axial potential minimum. Radial confinement is realized by an rf-potential. After sufficient accumulation the ions are released in bunches of 250 ns width by fast switching of the rear electrodes [Her03].
The cooled ion bunches from the RFQ are ejected to the switchyard displayed in Fig. 4.6. Here horizontal deflectors allow guiding the beam either to TRIGA-LASER located at the right port or to TRIGA-TRAP in straight direction. The left port is dedicated to future experiments, e.g. a tape station for decay spectroscopy measurements. While high kinetic energies are favorable for collinear laser spectroscopy, Penning-trap mass spectrometers require slow ions for efficient trapping. Several possibilities were realized at different experiments. For example at SMILETRAP only the preparation trap was floated at high potential to slow down the ions and afterwards pulsed down [Ber02]. Since this is more challenging for higher potentials the entire magnet and detection units can be kept on high potential like at JYFLTRAP [Ero12]. A different approach is followed at TRIGA-TRAP, where the ions are already slowed down in a pulsed drift tube (PDT) and the traps are close to ground potential. The PDT is kept on high potential being only a bit lower than the ion source potential to remove almost the entire kinetic energy and subsequently pulsed down to the transport potential of -1.1 keV [Smo12].

4.2 Off-line ion production at TRIGA-TRAP

Apart from the on-line ion source introduced in Sect. 4.1 several off-line, in majority surface ion sources are included into the TRIGA-SPEC setup. They are mainly used for calibration and test purposes. In the following section the laser ablation ion source at TRIGA-TRAP is introduced. It is used for the production of carbon cluster ions as mass reference but offers as well the possibility to produce ions of various other elements. Recent upgrading improved the ion pulse quality so that it allowed mass measurements on nuclides which were not accessible up to now. Its functionality is described in this section and the results of the measurements in Chap. 6.

For the production of e.g. carbon cluster ions as mass reference, a laser ablation ion source was developed at TRIGA-TRAP [Smo08, Smo09]. Although it was originally only designed for the production of carbon cluster ions, several other species can be ionized as well.

The principle of the further developed laser ablation ion source is shown in Fig. 4.7, for an overview of the old version the reader is referred to [Smo09]. A Nd:YAG laser (Continuum Minilite), which is frequency doubled to a wavelength of 532 nm with a pulse width of 5 ns carrying maximum 50 mJ energy, is used for ablation. By a motorized polarizing

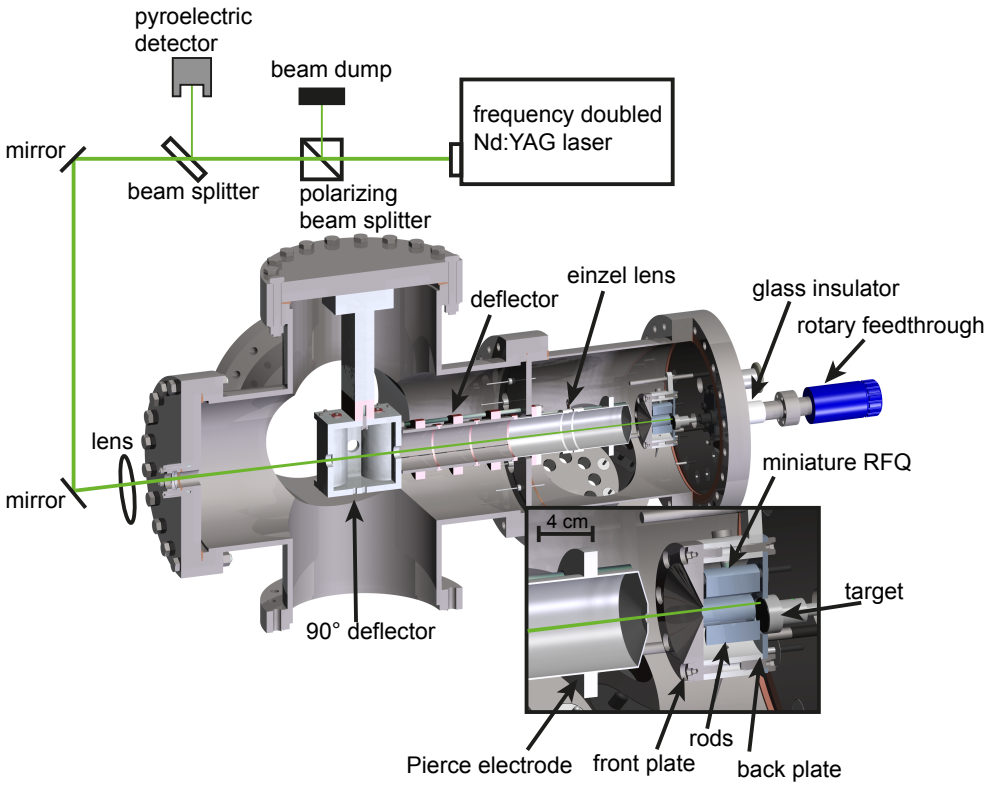

Figure 4.7: 3D sketch of the laser ablation ion source. A frequency doubled Nd:YAG laser pulse at $\lambda = 532\,\mathrm{nm}$ is focused on a target inside the vacuum chamber. The off-axis position of the target allows access to a complete circle on the surface. After production the ions are stored inside a miniature RFQ for about 5 ms where their motions are cooled by collisions with helium. Afterwards the ions are ejected and guided towards the experiment.

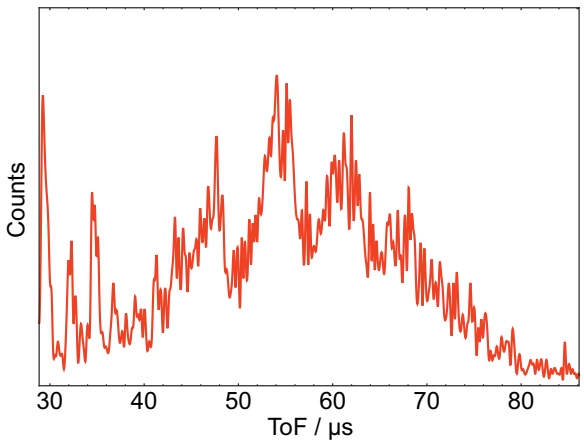

Figure 4.8: Time-of-flight spectrum of carbon cluster ions from the laser ablation ion source to a detector in front of the magnet without cooling.

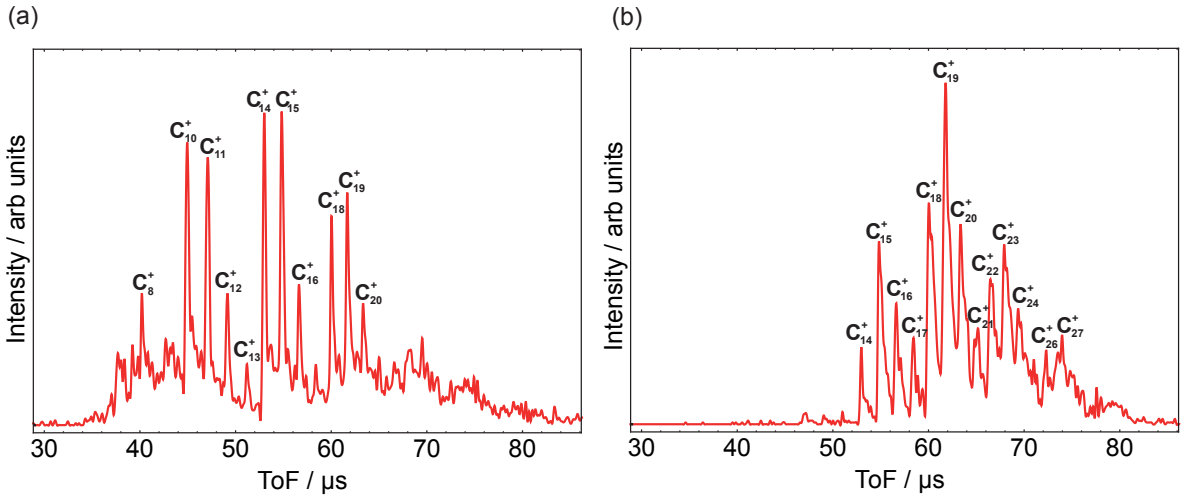

Figure 4.9: Time-of-flight spectrum of carbon cluster ions from the laser ablation ion source to a detector in front of the superconducting magnet with cooling in the mini RFQ. When U_{dc} is kept the same for all four rods, the transmission of the heavy clusters is suppressed (a). A potential difference at neighboring rods, while opposing rods are kept on the same potential favors transmission of heavy clusters (b).

beam splitter (Thorlabs PRM1Z8) the beam energy is reliably controllable. The actual energy measurement is done by a pyroelectric sensor (Thorlabs ES111C) to which 11 % of the laser beam are directed by a beam splitter. With a motorized lens having a focal length of 450 mm in front of the vacuum chamber the remaining laser beam is focused onto the target, reaching maximum power densities of $1.9 \times 10^{10}\,\mathrm{W/cm^2}$. A few microseconds after the ionization, the back plate as well as the target potential are increased from 47 V to 90 V to confine the ions inside the miniature radiofrequency quadrupole (mini RFQ). Here, rear and front electrodes have only a DC potential for axial confinement, whereas the non-segmented rods are set to a superposition of 60 V_{dc} and 800 $V_{rf,pp}$ potentials for radial confinement[2]. During the 5 ms the ions are stored inside the Mini RFQ their energy spread is reduced by collisions with helium atoms at gas pressures of about 10^{-3} mbar. For extraction, the front plate of the Mini RFQ is pulsed down to -20 V. The bunch is extracted by an electrode in Pierce geometry [Pie49] and subsequently focused and centered on the 90° deflector, guiding the beam towards the ion traps.

With the old ion source concept it was not possible to distinguish different carbon clusters based on their time of flight to an MCP detector in front of the superconducting magnet, about 2 m downstream (see Fig. 4.8). The resolution was tremendously improved by the installation of the Mini RFQ demonstrated in Fig. 4.9. Depending on the dc voltage applied at the rods, different mass regimes are stored. Applying the same voltage at all four rods favors the storage of cluster ions C_n^+ with $8 \leq n \leq 20$ (Fig. 4.9(a)). Heavier cluster ions can be stored when a potential difference between neighboring rods is introduced,

[2]The phase of U_{rf} on neighboring rods is shifted by 180°.

while opposing rods are kept at the same potential. This increases the maximum storable mass and simultaneously suppresses the storage of light ions (Fig. 4.9(b)). The heaviest ion which is clearly distinguishable in the time-of-flight spectrum is C_{27}^+, whereas even heavier cluster ions are hidden in the continuous part of the spectrum at 80 μs and above (4.9 b). The implementation of the Mini RFQ enables the clear selection of one carbon cluster ion species with C_n^+ with $8 \leq n \leq 27$ already before they reach the trap by a beam gate. This is important for the resolving power of the purification trap, depending on the total number of ions in the trap.

Presently the carbon cluster ions are produced from a Sigradur[3] plate, a glassy carbon. Usually Sigradur is favored due to its good electric conductance, which defines the ion energy during its creation.

Analogously, foils of the elements Pd, Cd, Sm, Gd, W, Au were already used [Ket10a, Smo12], where the atomic as well as the molecular oxide ions were observed. Latter are created due to the oxidization of the foil surface. With a different approach a few mg of powder are sufficient as for measurements on enriched ^{180}W and ^{184}Os. The target is then produced by mixing the enriched sample with silver powder, using its adhesive force to create mechanically stable targets, and pressing the mixture to a pellet with a pressure of about 35 kg/mm^2 [Smo12].

Even smaller amounts of a sample require a more efficient use of the material. In case of transuranium elements the usual limit of available material is about 10^{16} atoms or less. Gadolinium, being the chemical homologue of transuranium elements, has been used for several tests. Here, the sample was solved in 0.1 molar nitric acid in different concentrations. This solution was placed on a Sigradur backing in a drop of 10 μl and subsequently dried. Then only the solved material remains on the surface and ions of the deposited material were produced using laser intensities around 400 μJ. This was already done with samples of Gd, Eu, Lu and Hf where it was determined that at least 10^{15} atoms are required to determine a cyclotron frequency containing a few hundred events with the ToF-ICR technique[4]. Also ^{241}Am was tested, but no mass measurement was performed [Ket10a, Smo12]. Since the sample material is directly deposited on the Sigradur, carbon cluster ions are always present and have to be cleaned away in the purification trap by mass-selective buffer gas cooling.

This method was also used for the mass measurement performed within this work, using concentrations of 10^{14} atoms per μl. Thanks to the Mini RFQ the material was used more efficiently since the ions are captured and cooled in situ, in contrast to the previous setup. As benefit of the cooling, not more than one neighboring carbon cluster ion specimen reaches the trap while the others are blocked by the beam gate. Additionally it is secured that all sample ions are captured in the purification trap due to their lower energy spread. In summary it was possible to perform an entire mass measurement with the TOF-ICR technique, consisting of 15 to 23 recorded cyclotron resonances of the ion of interest containing each at least 500 ions, with only 10^{15} atoms on the target.

[3] Trademark of HTW Hochtemperatur Werkstoffe GmbH

[4] Remarkably, only oxide ions were detected so far with this method.

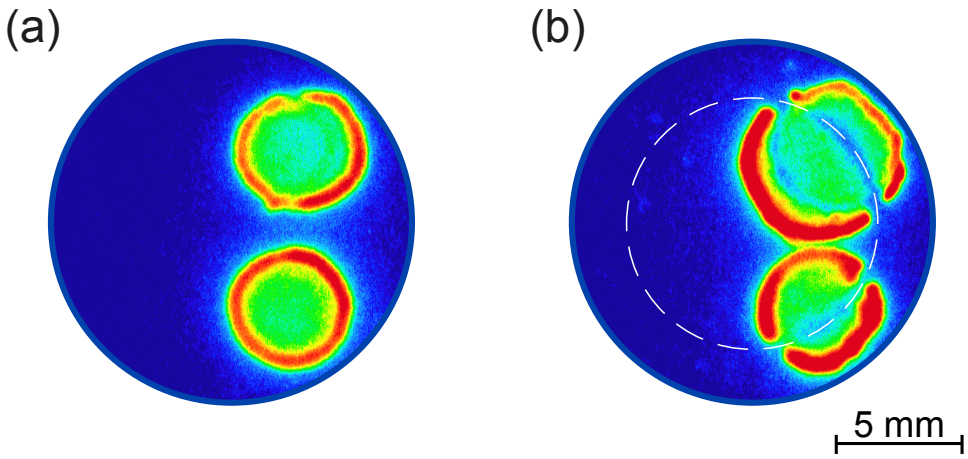

Figure 4.10: Radiographic image of an unused (a) and a used (b) target. The blue circle represents the circumference of the target, while the dashed line is the laser track. Each of the spots contains 10^{15} atoms of ^{249}Cf. The color is a measure for the radioactivity, ranging from red representing high activity to blue where no activity was detected.

Drying a drop on a surface with contact angles below 90° always results in creation of rings in which the majority of the solved material is deposited in a circular [But03] as shown in Fig. 4.10. These images were obtained by irradiation of a photo-plate by the radiation from the the radioactive material and subsequent analysis using a position sensitive imager (Fujifilm FLA 7000). The circle represents the circumference of the Sigradur plate, the dashed line is the laser path on the target. Obviously most of the radioactive material is presently not reachable with the laser. Analysis showed that more than 90 % of the material remains on the target.
By minimizing the size of the wetted region and simultaneously eliminating the ring, the material can be used more efficiently. The outward flow which occurs during the evaporation process as well as the wetting depend on the angle between liquid and backing material, the so-called contact angle. Increasing the angle to more than 150° decreases the wetted surface and simultaneously eliminates the ring [But03]. Tests on several backing materials were already performed showing an increased yield [Ren12]. Further mass measurements on transuranium nuclides with comparably short half-life and less abundance will require the application of this method.

4.3 Ion transport

Ions, either produced in one of the off-line ion sources or coming from the on-line ion source, are transported by an ion optical system to the superconducting magnet. As indicated in Figs. 4.1 and 4.11 the laser ablation as well as the surface ion source are mounted perpendicular to the beam line. Their ion beams are bent into the beam line towards

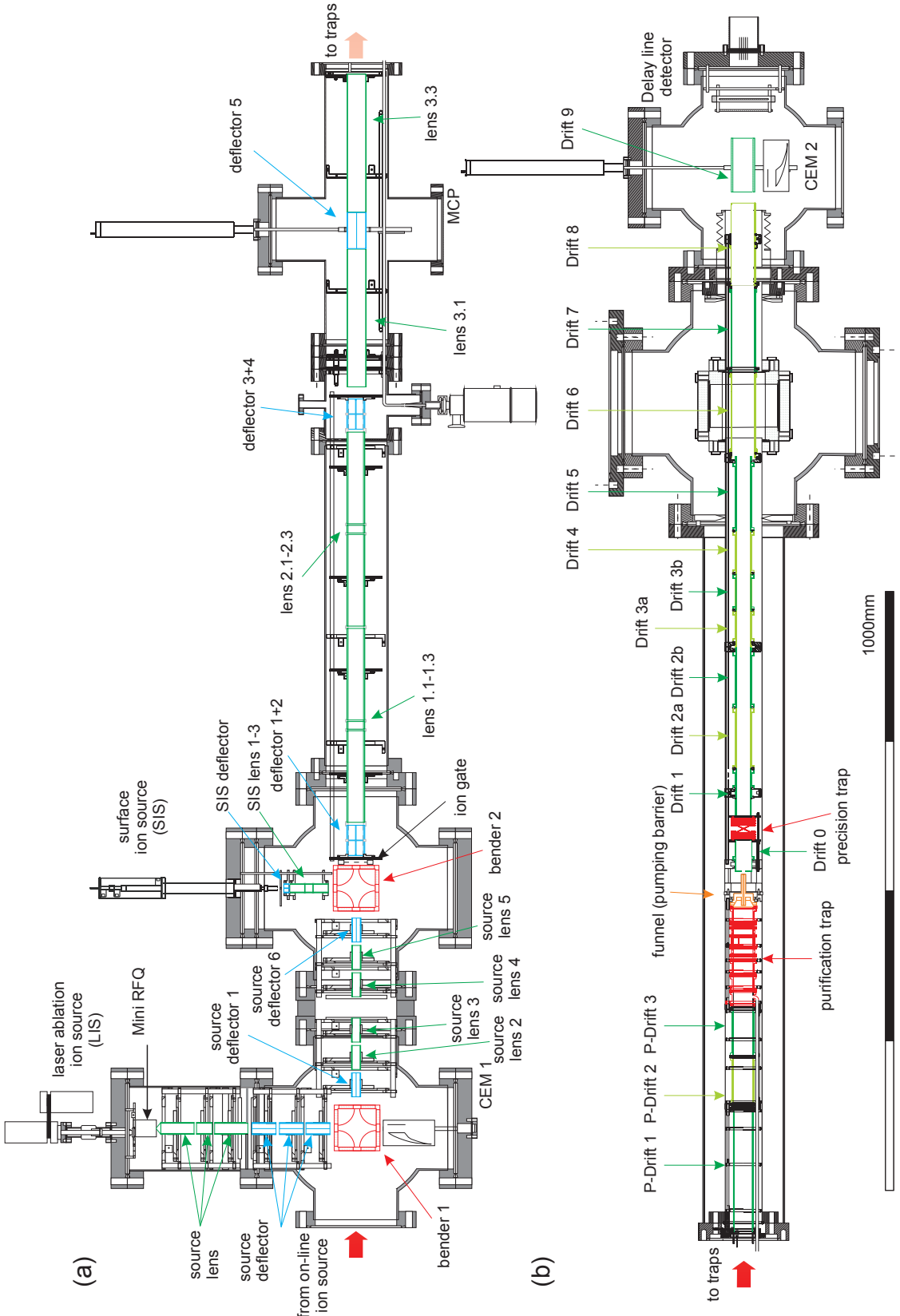

Figure 4.11: Illustration of the TRIGA-TRAP ion optics (adapted from [Smo12]). The transport section with the off-line ion sources (a) and the traps with the time-of-flight section (b) are shown. Drift tubes are colored green, deflectors blue and the 90° benders as well as the Penning traps are shown in red color. Ions are either produced in one of the off-line ion sources or delivered from the on-line ion source (from the left). Ion optics guide them further to the trap region inside the magnet and ToF section.

the Penning traps by electrostatic 90°-deflectors. Due to these ion source positions it is impossible for neutral atoms to reach the Penning trap, being very important in case of the laser ablation ion source. The exit of bender 2 is simultaneously an ion gate. It is used to either chop the continuous beam coming from the surface ion source for trapping or to block unwanted ions coming from the laser ion source. This is realized by a simple ion gate: A metallic grid is switched between 600 V to block the ions and 0 V for transmission. In order to achieve proper selection it is kept at high potential and pulsed down and up again very fast to allow only transmission of in principle one ion species [Ket10a, Smo12]. However, its present position is too close to the ion source, not allowing for the separation of neighboring isotopes.
Deflectors behind each ion source are used to correct possible misalignment. Afterwards, a parallel beam is prepared and focused into the magnetic field by the last einzel lens (lens 3.1, deflector 5, lens 3.3). Inside the magnetic field, the ions are slowed down by three drift tubes (P-Drift 1, 2, 3) from about 1 keV kinetic energy to about 100 eV, which allows trapping the ions in the purification trap. The subsequent precision trap is separated by a funnel with an inner diameter of 1.5 mm, which limits buffer gas atoms diffusing to it.
Behind the precision trap an additional drift section is installed, which is only necessary for the ToF-ICR technique. With the drift tubes inside the magnetic field gradient (1, 2, 3a, 3b) the ions are transported slowly. Especially the ion velocity at the position of Drift 3a has to be as low as possible to promote the adiabatic conversion from radial to axial motion. The actual detection is done by an MCP detector at the end of the beam line.

4.4 The double Penning-trap system

The heart of the TRIGA-TRAP experiment is the double Penning trap system inside the superconducting magnet. Being designed in [Web04], they are dedicated to TRIGA-TRAP since 2007 [Ket08]. The first trap, used for mass selective buffer gas cooling [Sav91] (see Sect. 3.3.2), has a cylindrical shape to achieve a high pumping cross section. It is also equipped with a low noise amplifier for broad band FT-ICR detection [Rep08, Knu09]. The second trap has a hyperbolical shape. This minimizes electric field imperfections at large radii, which is important for the narrow-band FT-ICR detection taking place here. Additionally the ions can be prepared in this trap for the TOF-ICR mass measurement technique.
Both Penning traps as well as a few ion optical elements in front and behind of them are mounted inside a vacuum tube, which can be cooled down to 77 K. Therefore, the tube is tripple-walled with the inner tube being surrounded by a liquid nitrogen reservoir. Both are decoupled from the outer tube by an isolation vacuum. This is usually used to improve the pressure in the traps, required for the narrow-band FT-ICR detection to decrease the thermal difference between resonator and trap. The electrodes inside the magnetic field from P-Drift 2 up to Drift 5 were manufactured out of oxygen free high purity copper (OFHC) with a purity of 99.99 %. Due to its high thermal and electric conductance as

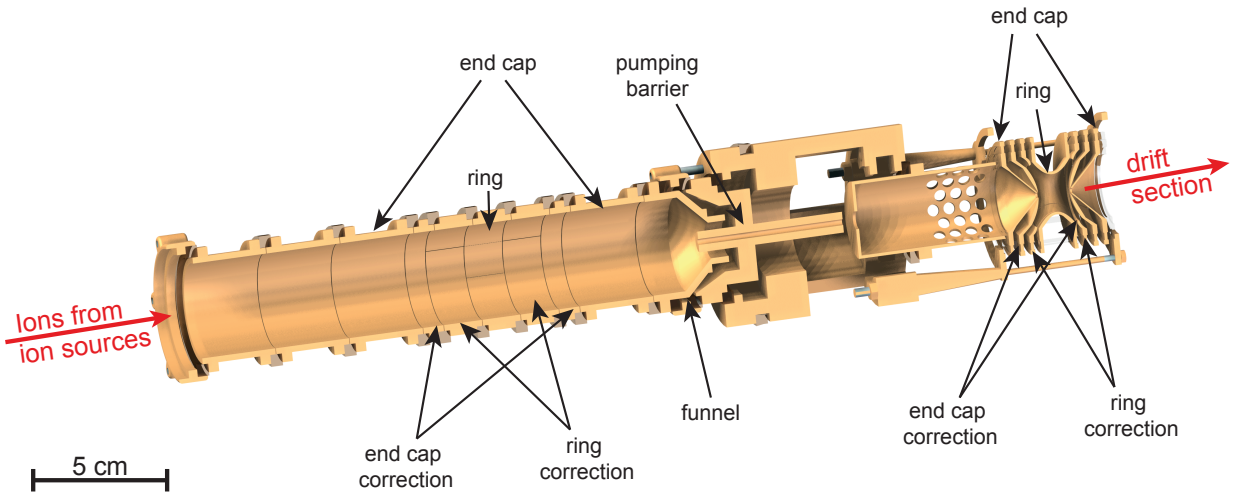

Figure 4.12: 3D sketch of the Penning traps at TRIGA-TRAP. The ions enter the cylindrical purification trap, consisting of seven partly segmented electrodes, from the left. While the actual trap potential is at 70 V the electrodes left and right of the end caps are additionally put on 200 V for a higher energy acceptance. All ions that are not centered by buffer gas cooling hit the funnel, whereas the desired ion species passes the pumping barrier. Inside the hyperbolic seven-pole trap the actual cyclotron frequency measurement is performed.

well as low magnetic susceptibility this material was considered to be perfect for the high magnetic field strength as well as thermal variations of more than 200 K inside the magnet.The electrodes, separated by aluminum oxide insulators, are mounted into two stacks for better alignment, which are separated by the pumping barrier in the center of the magnet. For the measurements presented in this work the trap tube was kept at room temperature.

As already mentioned the strong magnetic field needed for the Penning traps is created by a superconducting magnet, of a type being already in use at SHIPTRAP [Dil00], JYFLTRAP [Ero12] and MLL-TRAP [Kol08]. The traps are located 20 cm apart in homogeneous field regions with a strength around 7 T. Small inhomogeneities were detected here using an NMR probe with $B_2 = 1.05(6) \times 10^{-5}\,\mathrm{T/cm^2}$ at the purification trap and $B_2 = 5.3(2.0) \times 10^{-6}\,\mathrm{T/cm^2}$ at the precision trap position [Rep08].
Additional correction coils are implemented for enhanced temporal stability of the B-field by compensating the flux creep effect [And62]. After stabilization of magnet bore temperature and gas pressure in the liquid helium dewar [Smo12] the temporal stability improved to $-5.36(6.94) \times 10^{-11}$ /h. This was determined from cyclotron frequency measurements of $^{12}C^{+}_{21,22,23}$ over a complete month. Usually the correction coils are discharged every month resulting in a field jump of about $1.5 - 2\ \mu$T. This allows to calculate the magnetic field change without compensation of $-57.1(1.6)$ nT/d [Vie13]. For actual mass measurements this does not have a significant contribution to the uncertainty as they take place on a scale of hours.

Fig. 4.12 shows a detailed 3D drawing of the two Penning traps. The first one is the purification trap used to capture and cool an ion bunch including cleaning away unwanted ion species. It consists of a ring electrode and two end cap electrodes. For the improvement of the harmonicity of the electric potential additional correction electrodes are used.The ring electrode is fourfold segmented in two pieces covering 40° and two pieces covering 140°. The smaller segments are used for ion motion manipulation using dipolar and quadrupolar excitations while the larger segments are reserved for the narrow-band FT-ICR detection [Knu09, Ket10a]. In total the trap has a length of 212.5 mm with an inner diameter of 32 mm.
For the use of mass selective buffer gas cooling one of the end caps is equipped with a connector for a gas pipe. Through this pipe helium with rates of 10^{-5} mbar l/s is being leaked into the trap. Only the desired ion species is centered in the trap (for the principle see Sect. 3.3.2) while the remaining contaminants are kept at a large magnetron radius. After cooling, the whole ion cloud is ejected towards the precision trap. While ions with a too large magnetron radius are lost at the funnel, the cooled ions pass the pumping barrier and are captured in the precision trap. The second purpose of the pumping barrier, which has a length of 50 mm and an inner diameter of 1.5 mm, is the reduction of helium flow to the precision trap providing optimum conditions for mass measurements [Nei08]. Lateral helium flow is prevented by a TURCON Variseal, a PTFE ring around a metal spring.
Contrary to the purification trap, the precision trap has a hyperbolical shape. It was designed with minimal $C_4, C_6, ...$ to ensure a high electric field harmonicity at large radii. This is a consequence from the FT-ICR signal-to-noise ratio, increasing linearly with the ion motion radius [Web04]. However, the absolute size had to be kept small to ensure that the ions are always kept inside the homogeneous magnetic field region. Additionally the optimum ratio $\rho_0/z_0 \approx 1.16$ was chosen to create a trap, in which the eigenfrequencies are almost independent from their amplitudes [Gab83, Web04, Ket10a], being in particular important for FT-ICR detection.
Within these constrains the precision trap was designed, characterized by $r_0 = 6.38\,\text{mm}$ and $z_0 = 5.5\,\text{mm}$. The ring electrode is cut like in the purification trap in two 40° and two 140° segments, serving the same purposes. For ion injection and ejection holes with 1.8 mm diameter are drilled in the end caps.

4.5 Ion detection systems

Mass measurements are always carried out by the measurement of an observable. At TRIGA-TRAP in principle two different frequencies can be determined: the free cyclotron frequency from the conversion of magnetron into modified cyclotron motion, being used in the ToF-ICR technique, and the reduced cyclotron frequency used in the FT-ICR technique. While the principles of these techniques were discussed in Sect. 3.4, the technical details will be addressed in this section.

Destructive ion detection

The ToF-ICR technique requires time-of-flight measurements of ions to a detector after ejection from the precision trap as function of the quadrupolar excitation frequency (see Sect. 3.4.1). At TRIGA-TRAP single ion detection for the stop signal is carried out with two different electron multipliers: a microchannel plate detector (MCP)[5] and a Channeltron [Ket09a].
An MCP is composed of about 10^6 channels of typically a few μm diameter. During operation a potential difference of about 1 kV is applied across the channels. Thus, the impact of a particle releases an avalanche of secondary electrons with a gain of $10^3 - 10^4$. Even higher gains are achieved by adding a second plate rotated by 90° in the so-called Chevron configuration. They achieve usually ion detection efficiencies of 30-50 % with a time resolution of down to 100 ps for kinetic energies of 2 keV [Fer07]. Moreover, MCP detectors are not only used for time-of-flight measurements, but also for beam monitoring at several positions of the whole TRIGA-SPEC beam line. While the MCPs in the high energy part as well as the in TRIGA-LASER beam line are all equipped with additional phosphor screens for position sensitive detection the ones in the TRIGA-TRAP beamline miss this feature.
Although MCPs are widely in use, a more efficient ion detection may be desired for rarely produced nuclides in on-line beam facilities. This problem can be solved using a Channeltron detector. Here the ions are guided to a conversion dynode being mounted off-axis. Due to the ion impact electrons are emitted to a horn-shaped electron multiplier on the opposite side. This technique improves the overall efficiency to > 90 %.
Nevertheless, an MCP detector is commonly used at TRIGA-TRAP due to its 12.6 cm^2 active area, which is ten times larger than the one of a Channeltron. The large area is required since it is difficult to optimize the ion optics simultaneously for excited and non-excited ions. Additionally the ToF section is comparably long at TRIGA-TRAP due to the space needed for FT-ICR detection, which had to be placed sufficiently outside the magnetic field, resulting in an additional increase of the beam spot at the MCP.

Image current detection

Both Penning traps at TRIGA-TRAP are equipped with non-destructive detection electronics, allowing to read out the signals at both 140° ring electrode segments.
The purification trap will feature a system for broad band image current detection. This allows an analysis of the composition of the captured ion cloud and subsequent cleaning by increasing the motional amplitude of unwanted ion species using excitation of the modified cyclotron motion. For pre-amplification a cryogenic amplifier was adopted from the g-factor experiment in Mainz [Stu11]. It is attached directly to the trap to ensure short cables and lower parasitic capacitances, thus increasing the signal-to-noise ratio. Its usual

[5] The position sensitive delay line detector, mentioned in [Smo12], was removed.

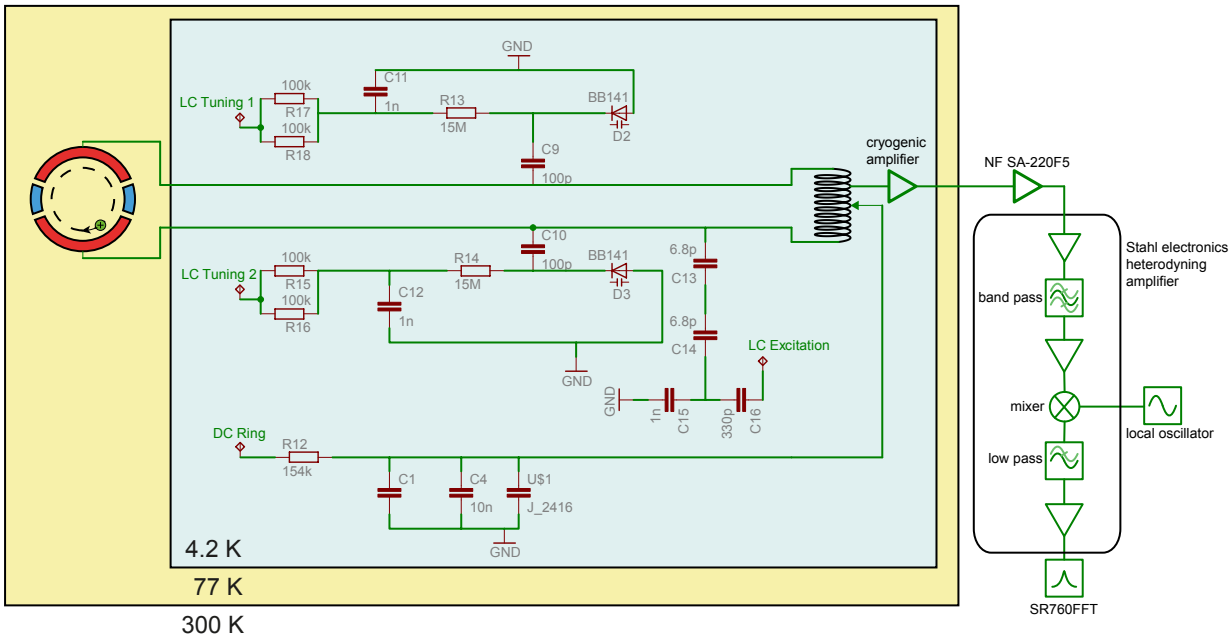

Figure 4.13: Sketch of the narrow-band FT-ICR detection circuit. The 140° ring electrode segments form a tank circuit together with the superconducting coil tuned to the modified ion-cyclotron frequency. Further processing of the signal is done by a cryogenic amplifier followed by two room temperature amplifiers. The last one provides additional filters for signal processing prior to the Fast Fourier Transformation.

operating temperature is 77 K with a second amplifier (NF SA-220F5) at room temperature. Further information on the installation of the system are given in [Knu09, Rep08]. The development of the second image current detection system started in [Ket06]. While the brad band detection system aims is designed for the detection of multiple ions, the system at the precision trap aims for the detection of single ions. This is achieved by increasing the effective parallel resistance (see Sect. 3.4.2). At TRIGA-TRAP this is realized using a helical resonator with a high quality factor forming a tank circuit with the trap. The coil is prepared in a way that the resonance frequency of the tank circuit fits exactly to the modified cyclotron frequency of the ion. Fig. 4.13 shows the detection scheme. The tank circuit consisting of trap and resonator is partly on 77 K and 4 K. Biasing of the ring segments is done via the center tap at the coil. In order to tune the resonance frequency exactly to the desired frequency a DC-voltage between 0 V and 10 V can be applied at *LC Tuning 1,2* changing the capacitance of the two capacitive diodes and lowering the resonance frequency. Functionality of the tank circuit can be verified by excitation at the proper frequency using *LC excitation*. The signal is extracted at a tap, located a few turns away from the center, amplified in the cryogenic low-noise amplifier supplying the NF SA-220F5 amplifier for further amplification. Afterwards the signal is processed by a heterodyning amplifier from Stahl electronics, which reduces noise with a free configurable band-pass filter and mixes the signal down. A low-pass filter secures that

no signals with higher frequency are transmitted to the FFT analyzer. The Fast Fourier Transformation itself is performed by a Stanford research system SR760FFT, providing two inputs at maximum 102.4 kHz. A broader frequency range can be covered by replacing the heterodyning amplifier and SR760FFT with an Agilent Spectrum Analyzer NI1996A. Further information on resonator and cryogenic amplifier design is provided in Chap. 5.

Chapter 5

Further development of the FT-ICR ion detection technique

The principle of the Fourier transform-ion cyclotron resonance (FT-ICR) technique was described in Sect. 3.4.2 as the detection of the image current induced in the ring electrode segments by ideally one single ion. The detection system as a whole, shown in Sect. 4.5, consists of a tank circuit composed of coil and trap electrodes, followed by a cryogenic amplifier and some filter stages (see Fig. 4.13). A similar installation was already used in a test setup, which was tuned to the cyclotron frequency of $^{85}Rb^{+}$ [Ket09a]. Several high-Q resonators were tested using superconducting NbTi as well as normal conducting copper wires [Ket06, Ket09b]. The following chapter summarizes further developments made within this work pointing out the differences to the formerly tested approaches including the cryogenic amplifier and displays their characteristic behavior.

5.1 The high-Q resonator

Image current detection is routinely used in FT-ICR spectrometers in analytical chemistry for the simultaneous detection of many ions employing a broadband amplifier [Com74]. In comparison it is more challenging to detect the image current of one singly charged ion, requiring an elaborate system for noise suppression and low-noise amplification. Similar systems are routinely used at other Penning-trap experiments, e.g. THe-TRAP, g-factor HCI, etc.. Since the tank circuit depicted in Fig. 3.9 acts as a band-pass filter, one key component of such a detection system is an inductance with a high quality factor. According to Eq. (3.65) this guarantees a high noise suppression at other frequencies than the reduced cyclotron frequency of the ion. Since the goal at TRIGA-TRAP is the implementation of an FT-ICR system to measure the mass of actinoide ions, a high inductance L is desired to obtain a resonance frequency around 500 kHz. (See Tab. 3.1 and Eq. (3.62)). This is achieved with a coil of 220 turns of 40 μm thick NbTi wire, insulated with *FORMVAR*, wound around a hollow PTFE core having an outer diameter of 42 mm and a wall thickness of 1.5 mm. One tap at 110 turns is used to bias the ring electrode segments with

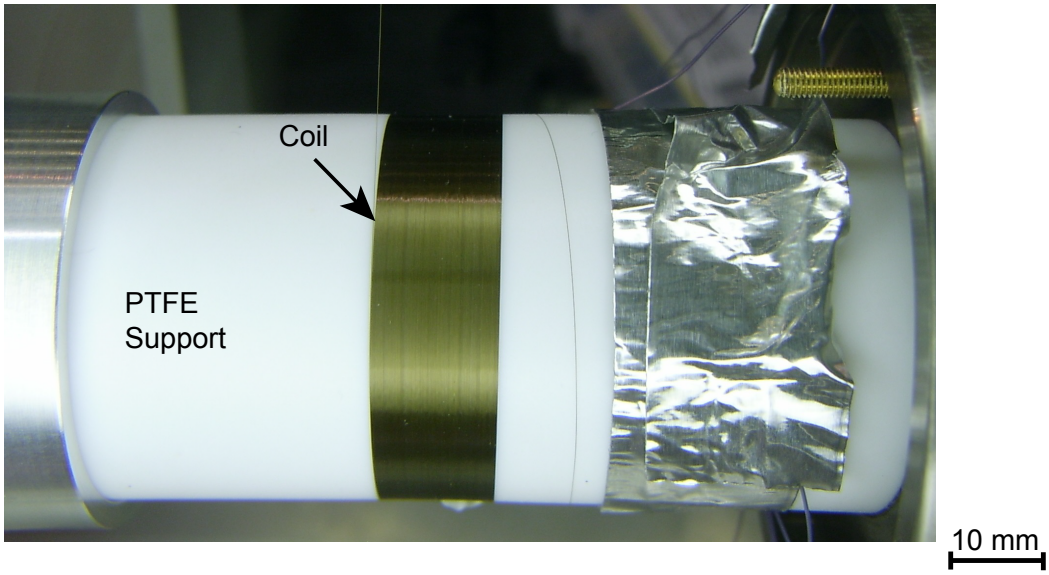

Figure 5.1: Photo of the superconducting coil during the manufacturing process. The 40 μm thick *FORMVAR* insulated wire is wound in 220 turns around a hollow PTFE cylinder. Connections between normally and superconducting wire are made with regular soldered connections.

-10 V and one at 75 turns to couple the signal to the cryogenic amplifier. A photo of the coil is shown in Fig. 5.1. Adopted from radio communications [Mac59], the coil is mounted inside a polished NbTi shield in a polished helical resonator geometry to increase the Q value further.

The properties of the so produced coil were determined in a test setup attached to a 4-K cryocooler. A well-known capacitor and the coil were connected to a tank circuit, which was excited with white noise. Via an antenna placed inside the resonator the signal of the tank circuit was picked up and its resonance frequency was determined. The result of one measurement is shown in Fig. 5.2. Here, the signal strength was obtained as function of the frequency. The resonance frequency as well as the Q value were obtained from a fit of Eq. (3.64) to the data. By repeating the measurement with a second capacitor of different value, the intrinsic capacitance as well as the inductance of the coil were determined using the equation system

$$\nu_i = \frac{1}{\sqrt{L_{\text{coil}}(C_{\text{coil}} + C_i)}} \text{ with } i = 1, 2 \ . \tag{5.1}$$

This includes the assumption that additional inductances are negligible. With the two capacitors $C_1 = 10\,\text{pF}$ and $C_2 = 15\,\text{pF}$ and the respective resonance frequencies $\nu_1 = 597992.1(6)\,\text{Hz}$ and $\nu_2 = 544297.3(3.4)\,\text{Hz}$ the coil properties were determined to be

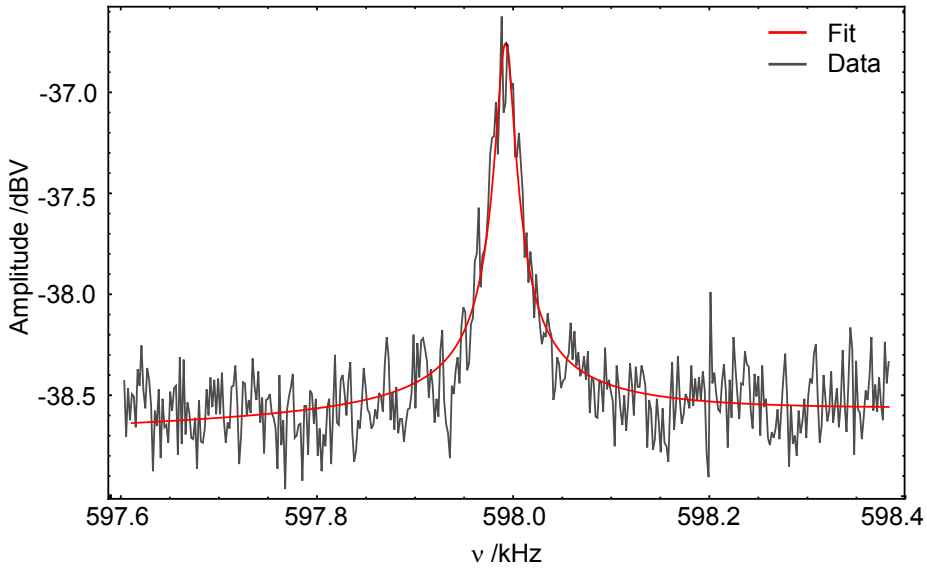

Figure 5.2: Resonance spectrum of the superconducting helical resonator. The unloaded quality factor $Q = 27(2) \times 10^3$ as well as the resonance frequency $\nu_{\mathrm{LC}} = 597992.1(6)\,\mathrm{Hz}$ were obtained from a fit (red) using Eq. (3.65) resulting in a 3 db width of 22 Hz. The data points are connected to guide the eye.

$$L_{\mathrm{coil}} = 2.9(5)\,\mathrm{mH} \tag{5.2}$$

$$C_{\mathrm{coil}} = 14.1(4.6)\,\mathrm{pF}\ . \tag{5.3}$$

The Q value of the unloaded tank circuit obtained from the measurements is $Q = 27(2) \times 10^3$. This can be regarded as an upper limit since the Q value will be further limited due to the connected trap electrode.
On the basis of the here obtained values, the serial resistance of the superconducting resonator can be calculated with Eq. (3.57) yielding $R_{\mathrm{s}} = 0.404(76)\,\Omega$, resulting in a specific resistance of $1.75(33) \times 10^{11}\,\Omega\mathrm{m}$. In this calculation the skin effect as well as the errors of cable length and diameter were neglected. Contributions from the short copper connections were not considered as well.
This value for the specific resistance is in the same order of magnitude as a value obtained from a susceptibility measurement but two orders of magnitude higher than the one obtained from a Q-value measurement with a similar resonator [Ket06]. This is likely due to an optimized coil production procedure.

5.2 The new TRIGA-TRAP cryogenic amplifier

Ultimately high signal-to-noise ratios require low temperatures as pointed out in Eq. (3.70). Thus, an amplifier, originally designed for the g-factor experiment and optimized for oper-

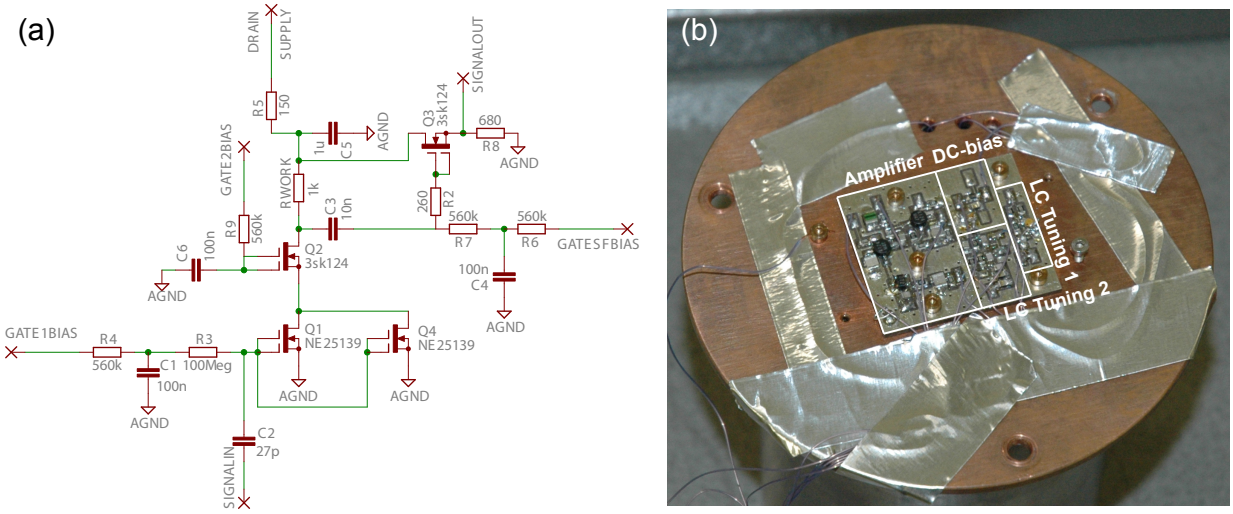

Figure 5.3: Schematics (a) of the cryogenic amplifier [Stu11] and photo of the final board (b), which includes also the electronics shown in Fig. 4.13. On the backside of the Cu disc, the superconducting resonator is attached.

$U_{\text{Gate 1}}$	$-0.95\,\text{V}$
$U_{\text{Gate 2}}$	$-0.4\,\text{V}$
$U_{\text{Gate 3}}$	$-0.2\,\text{V}$
U_{Drain}	$4.0\,\text{V}$

Table 5.1: Settings for one working point of the cryogenic amplifier. With these settings an amplification of 7.8(3) is reached at $T = 4.2$ K.

ation at liquid helium temperature [Stu11], was adopted at TRIGA-TRAP as the second key part of a single ion detection system. For the operation at TRIGA-TRAP especially the frequency response and the noise at frequencies below 1 MHz are important, as operation in this regime was not foreseen in the original design [Stu11].

In order to minimize the overall cable length before the signal is amplified, the amplifier is mounted on the backside of the resonator, which is anyhow cooled down to $T = 4.2$ K. Fig. 5.3 shows the connection diagram of the amplifier (a) and a photograph of the final device (b). The working point with the gate and drain voltages listed in Tab. 5.1 was chosen for all further tests. It provides an amplification factor of 7.8(3) at liquid helium temperature. The error is defined as the standard deviation of several measurements.

TRIGA-TRAP attempts for mass measurements ranging from iron to californium. On top of that the actinoides are routinely produced as singly charged monoxides while it is expected that the new on-line ion source makes doubly charged ions available [Sch15]. Thus, ions with q/m ratios ranging over almost one order of magnitude resulting in cyclotron frequencies between 400 kHz and 3.6 MHz are created at TRIGA-TRAP. Therefore, it is important that the frequency response of the amplifier is frequency independent in a broad range.

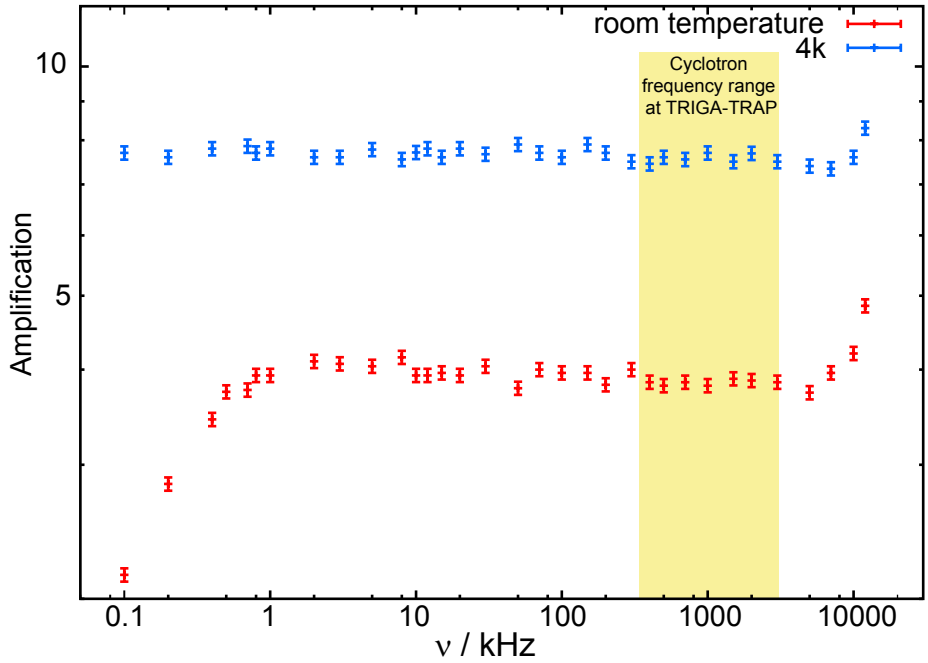

Figure 5.4: Frequency response of the cryogenic amplifier at $T = 4.2$ K and at room temperature. Even at room temperature the amplification as function of the frequency of the signal is constant between 1 kHz and 10 MHz.

The **frequency response** was measured at room temperature and at $T = 4.2$ K. The result of this test, displayed in Fig. 5.4, shows that the amplification as function of the frequency is constant in the desired range from 400 kHz to 3.6 MHz and even beyond at both. At liquid helium temperature, the amplification is about twice as high as at room temperature using the same working point.

The second important parameter is the **voltage noise** created by the amplifier itself. It has to be extremely low since it has an important influence on the signal-to-noise ratio as pointed out by Eq. (3.70). Thus, the intrinsic noise of the cryogenic amplifier determines the upper limit of the overall sensitivity of the FT-ICR detection system. Noise measurements of devices with a very low intrinsic noise require special low noise equipment with a precisely known voltage noise level. It was performed by first measuring the intrinsic voltage noise of the Agilent N1996A-506 spectrum analyzer with a short to ground at the input to prohibit external signals from coupling into the device. Since its white noise is at a level of about $25\,\mathrm{nV}/\sqrt{\mathrm{Hz}}$ the room temperature amplifier NF SA-220F5 is used as intermediate stage for the actual noise measurement of the cryogenic amplifier. For its complete characterization the reader is referred to [Rep08]. It shall only be mentioned that its high gain of $G = 200$ in combination with a low intrinsic voltage noise density of $0.5\,\mathrm{nV}/\sqrt{\mathrm{Hz}}$ amplifies the expected low noise of the cryogenic amplifier without a significant contribution to the total noise. Nevertheless, its intrinsic noise spectrum is recorded

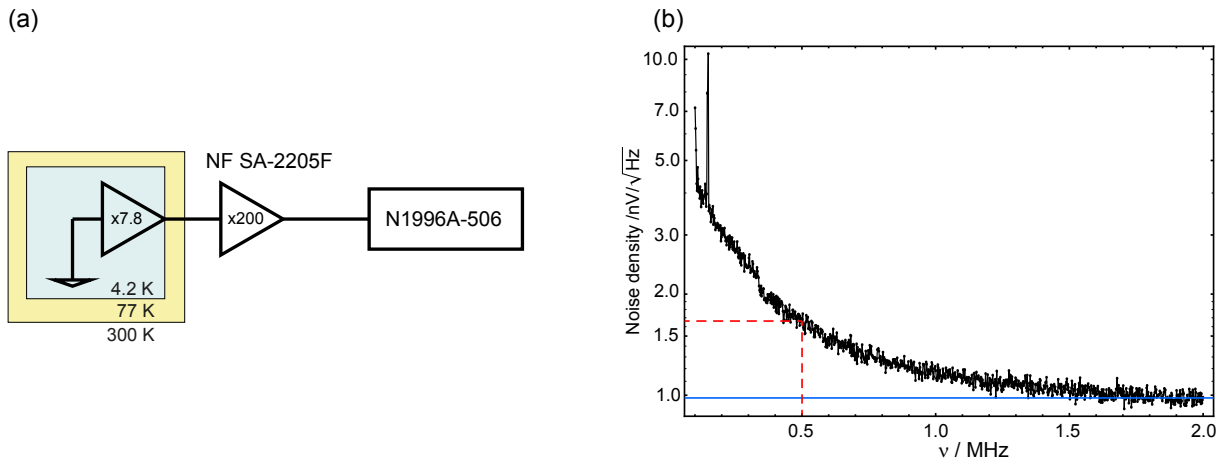

Figure 5.5: Setup of the voltage noise measurement (a) with shortened input at liquid helium temperature. The obtained voltage noise density spectrum (b) decreases to less than $1\,\mathrm{nV}/\sqrt{\mathrm{Hz}}$ in the white noise regime. For mass measurements on actinide nuclides the noise at 500 kHz with $1.66(5)\,\mathrm{nV}/\sqrt{\mathrm{Hz}}$ is important.

routinely before every noise measurement to ensure proper functionality.

With the setup shown in Fig. 5.5(a) the intrinsic noise density spectrum of the cryogenic amplifier displayed in Fig. 5.5(b) was determined. This requires knowledge of the intrinsic noise of all used components. Since the noise adds squared and can be amplified one has to employ

$$e_{\mathrm{cryo}} = \frac{\sqrt{\frac{e_{\mathrm{tot}}^2 - e_{\mathrm{SA}}^2}{G_{\mathrm{NF}}^2} - e_{\mathrm{NF}}^2}}{G_{\mathrm{C}}} \,. \tag{5.4}$$

Here, e_{cryo}, e_{NF}, e_{SA} and e_{tot} denote the noise densities of the cryogenic amplifier, the room temperature amplifier and the spectrum analyzer as well as the total noise density recorded at the end of this daisy chain. G_{NF} and G_{cryo} are the amplification factors of the amplifiers. While the white noise density level is well below $1\,\mathrm{nV}/\sqrt{\mathrm{Hz}}$ the noise density at 500 kHz is at $1.66(5)\,\mathrm{nV}/\sqrt{\mathrm{Hz}}$. The latter is especially interesting for mass measurements in the actinoide region with cyclotron frequencies around 500 kHz.

Moreover, it is desired that the **input capacitance** of the amplifier is very low since it adds to the parasitic capacitance of the tank circuit. Its measurement is straight forward using the impedance of a capacitor $Z = 1/(\mathrm{i}\omega C)$. A comparison of input and output voltages with an additional input resistance R simplifies to

$$\frac{U_a}{U_e} = \frac{1}{1 + i\omega CR} \,. \tag{5.5}$$

Introducing the cutoff frequency

$$\nu_{\mathrm{G}} = \frac{1}{2\pi CR} \tag{5.6}$$

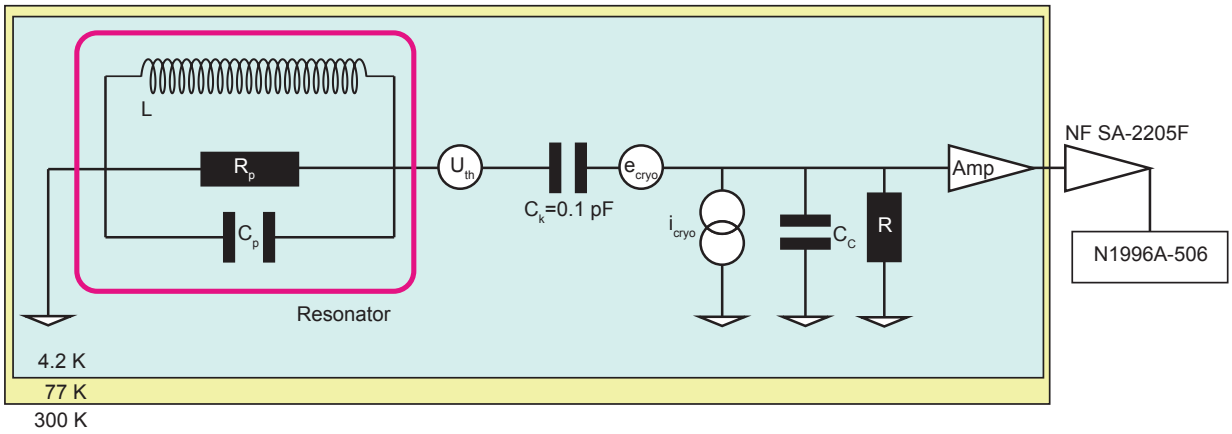

Figure 5.6: Circuit of the current noise measurement. The resonator is used as large resistor to detect the current noise. e_{cryo}, as well as i_{cryo}, C_{C} and R are intrinsic properties of the cryogenic amplifier and no actual parts or devices.

being the frequency at which the voltage drops to $1/\sqrt{2}$ the effective voltage drop is described by

$$\left|\frac{U_a}{U_e}\right| = \frac{1}{\sqrt{1+\left(\frac{\nu}{\nu_G}\right)^2}} \,. \tag{5.7}$$

Here, a resistor of 47.13(1) kΩ was connected in series with the input and white noise was applied by a function generator. This circuit is basically a low pass. With a fit of the output voltage from Eq. (5.7) to the data, the input capacitance was determined to $C_{\mathrm{C}} = 5.93(3)$ pF. This low value is of special interest for TRIGA-TRAP since the design of the experiment does not allow the amplifier and the resonator to be placed close to the trap. This requires cable lengths of several ten cm severely increasing the capacitance and by that limiting the resonance frequency.

The determination of the in general low **current noise** requires high resistances R to realize a measurable voltage drop. With the resonator a tool with a high parallel resistance is available. This requires cooling the entire set-up to liquid helium temperature, which additionally decreases the contribution of thermal noise. Considering that the thermal voltage noise is already created in the tank circuit the current noise calculated with Eq. (5.4) is

$$i_{\mathrm{cryo}} = \frac{\sqrt{\frac{e_{\mathrm{tot}}^2 - e_{\mathrm{SA}}^2}{G_{\mathrm{NF}}^2} - e_{\mathrm{NF}}^2}{G_{\mathrm{C}}^2} - 4kTR - e_{\mathrm{cryo}}^2}}{R} \,. \tag{5.8}$$

Fig. 5.6 displays the setup for the measurement. The resonator as well as the amplifier were cooled down to 4.2 K. In order not to limit the Q value the resonator was decoupled from

Working point	G	e_{cryo} / nv/$\sqrt{\mathrm{Hz}}$	i_{cryo} / fA/$\sqrt{\mathrm{Hz}}$
I	7.8(3)	1.66(5)	2.5(2.4)
II	8.3(3)	1.60(5)	2.6(2.4)
III	6.8(3)	1.69(5)	2.2(1.9)
IV	5.8(4)	1.86(6)	2.3(2.0)
V	4.7(5)	1.99(6)	2.3(1.8)

Table 5.2: Working point properties of the cryogenic amplifier. The voltage noise e_{cryo} as well as the current noise i_{cryo} for five different working points with different amplification G as described in Sect. 5.2 are listed. Working point I has been used for the described characterization.

the amplifier using a Johnson capacitor with C_k=0.1 pF. This capacitor, in combination with the input capacitance of the amplifier, can be treated as a voltage divider attenuating the thermal noise with

$$X \equiv \frac{U_{\mathrm{out}}}{U_{\mathrm{in}}} = \frac{C_k}{C_k + C_C} \ . \tag{5.9}$$

Thus, expressing the resistance with Eq. (3.58) changes Eq. (5.8) to

$$i_{\mathrm{cryo}} = \frac{\sqrt{\frac{e_{\mathrm{tot}}^2 - e_{\mathrm{SA}}^2}{G_{\mathrm{NF}}^2} - e_{\mathrm{NF}}^2}{G_{\mathrm{C}}^2} - 8\pi\nu kTQLX^2 - e_{\mathrm{cryo}}^2}}{2\pi\nu QL} \ . \tag{5.10}$$

The least precisely known parameter in this equation is T, since it is not possible to install a temperature sensor at the resonator while the current noise is determined. It is estimated from a preceding test carried out under identical conditions. However, since the coil became superconducting, it is secured that the temperature was well below 9.2 K. Also the amplification of the cryogenic amplifier G_{C} as well as the coil properties were extracted from other measurements. While the latter changes only due to mechanical changes, the temperature has slight effects on the G_{C}.
With these information and the measurement of a resonance the current noise at the working point I (see Tab. 5.2) was calculated to 2.5(24) fA/$\sqrt{\mathrm{Hz}}$. Despite the contribution of several uncertainties to the current noise error, it is mainly determined by the uncertainties of the background noise which is in the range of one percent.
Amplification, voltage and current noises were determined at five different working points of the amplifier with different settings for gate and drain voltages. The results are presented in Tab. 5.2. While the amplification can be changed over a wide range, mainly determined by the drain voltage, e_{cryo} does not change by more than 20 % and i_{cryo} remains the same. Due to a high drain-source current, a stable operation due to heating effects was almost impossible at working point II. Thus, working point I is considered for image current detection.
With all the properties of amplifier and resonator determined up to now, it is furthermore

possible to check whether the winding ratio between the complete coil and position of the coupling tap was chosen correctly or not. The winding ratio at which the noise minimizes is given by

$$\frac{N_1^2}{N_2^2} = \frac{R_\mathrm{p}}{R_\mathrm{opt}} \tag{5.11}$$

with the optimum resistance $R_\mathrm{opt} = e_\mathrm{cryo}/i_\mathrm{cryo}$ and the parallel resistance of the resonator R_p [Kra07]. With Eq. (3.58) the optimum position for the tap is

$$N_2 = \sqrt{\frac{e_\mathrm{cryo}}{i_\mathrm{cryo} \cdot Q\omega L}} N_1 \ . \tag{5.12}$$

Due to the design frequency of 500 kHz and the coupled Q value being limited to about 1500 the ideal position is at $N_2 = 49(28)$ turns. Thus, the present position at 75 turns is not perfect but still within the error, dominated by the current noise error. This leads to a large uncertainty of the ideal winding ratio. It directly affects the parallel resistance and thereby the Q value of the loaded tank circuit. In the worst case of $N_2 = 21$ the parallel resistance is decreased by a factor of 10 compared to the present one. However, the Q value reached within this work was improved compared to previous work [Ket06, Ket09b]. Nevertheless this result will be considered for the construction of a new coil.

5.3 Characterization of the new tank circuit

With the resonator and cryogenic amplifier being characterized, the detection circuit is set up as shown in Fig. 4.13 with one essential difference: The trap is not connected yet but represented by a 12 pF capacitor limiting the Q value in order to keep all connections as short as possible.
Since measurements with an ordinary tank circuit would be rather limited due to the fixed resonance frequency, two capacitive diodes are included. Biasing them with a voltage changes their capacitance and thereby the resonance frequency of the tank circuit. Fig. 5.7 shows that the frequency can be tuned over a range of about 80 kHz, which corresponds to a mass range of 149 u to 168 u. Simultaneously with the additional capacitances the Q value of the resonance gets lower favoring operation with as little bias as possible.
In its final position, shown in Fig. 5.8, the resonator is located at about 1.5 m distance from the trap requiring long cables contributing to the parasitic capacitance. This limits the quality of the resonance to values around $Q = 1400$. In addition the resonance frequency dropped to a lower value which can be tuned by the capacitive diodes from 464 kHz to 492 kHz corresponding to singly charged ions of masses between 231 and 218 amu at TRIGA-TRAP. Although the addressable ions are lighter than the routinely measured actinoide oxides (see Chap. 6), $^{12}C_{19}^+$, being produced in the cluster ion source, is available for first tests. Afterwards, the resonance frequency can be lowered by increasing the capacitance, e.g. by simply increasing the cable length between resonator and trap.

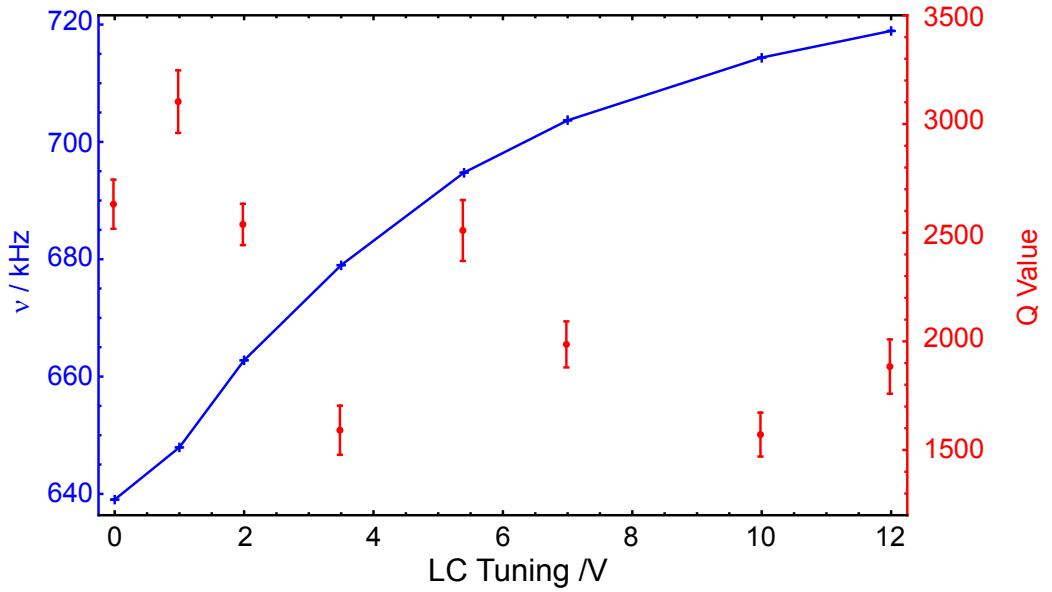

Figure 5.7: Influence of the *LC Tuning*. As function of the applied voltages the capacitances of the two capacitive diodes *MA46H206* can be changed, thus shifting the resonance to higher frequencies with increasing voltages (blue). Unfortunately this tuning simultaneously decreases the Q value (red).

5.4 Determination of environmental noise

The non-destructive image current detection of a single ion requires a tank circuit coupled to a low-noise cryogenic amplifier. These components are usually tested and characterized in an isolated test set up. When the actual detection is implemented it is also important to find and identify possible noise sources. If necessary, some components have to be insulated from the remaining set-up or entirely replaced. While these detection systems are mainly employed at relatively small experiments like the g-factor experiments in Mainz [Kra12,Stu13], TRIGA-TRAP being connected to the remaining TRIGA-SPEC experiment is comparably large. This enhances the number of possible noise sources.
It was determined that the noise detected at the ring electrode segments of the precision trap is extremely high. As pointed out in Fig. 5.9(a) the base line is not lower than 50 nV/$\sqrt{\text{Hz}}$ with peak intensities up to almost 10 μV/$\sqrt{\text{Hz}}$. This is a severe problem as the ion signal is not expected to be strong enough for detection. Even excitation of the tank circuit via *LC Excitation* did not reveal a resonance. The noise source was identified to be the switchable voltage sources (GSI HV-Switch Gen. I) being used at the precision trap for pulsing the end cap as well as correction electrodes. Thus, a new power supply was developed, which is very stable and rapidly switchable with a very low noise level [Ket09b, Ket14]. The noise contribution of the first prototype is displayed in Fig. 5.9(b) as the difference between the noise with and without the new voltage source. It is negligible up to 1.5 MHz. Below 600 kHz some of the noise seems to be short cut by

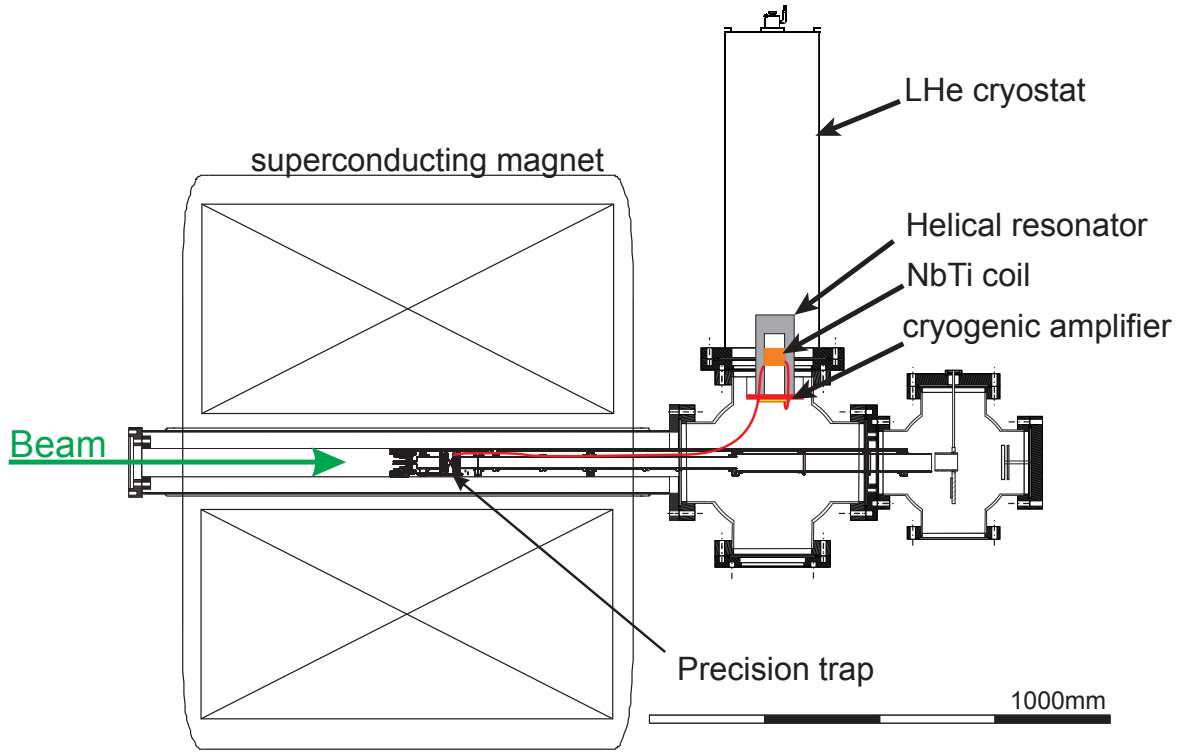

Figure 5.8: Schematics of the FT-ICR detection system. The precision trap is connected to the NbTi coil via long cables. Subsequently, the signal from the tank circuit is coupled out to the amplifier.

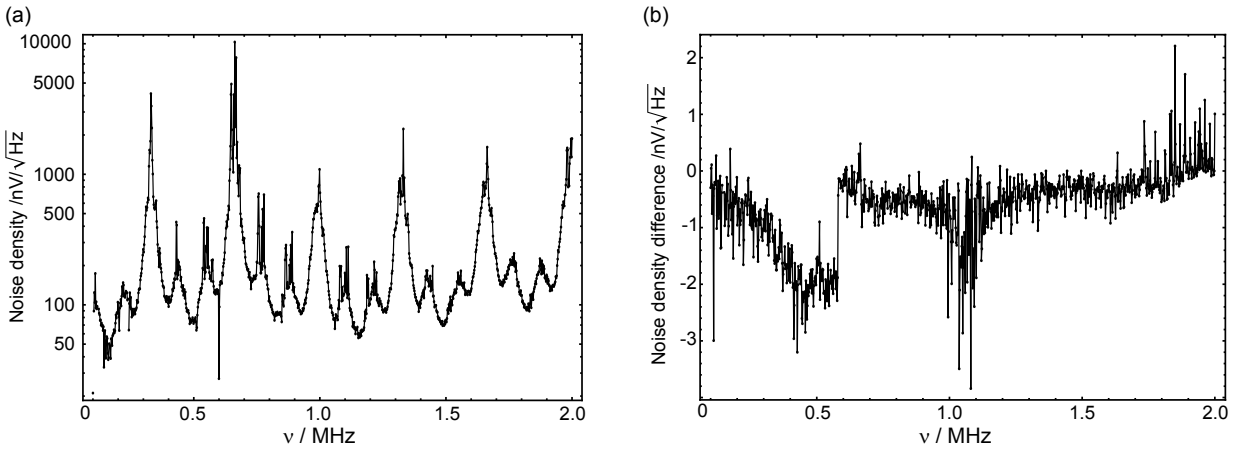

Figure 5.9: Impact of the switchable voltage sources to the noise density at TRIGA-TRAP. Presently they dominate the noise at TRIGA-TRAP (a) with peaks up to 10 $\mu V/\sqrt{Hz}$, which is by far too high for image current detection. The noise contribution of the first prototype of a newly developed voltage sources is almost negligible (b). Some of the noise is even short cut resulting in negative values.

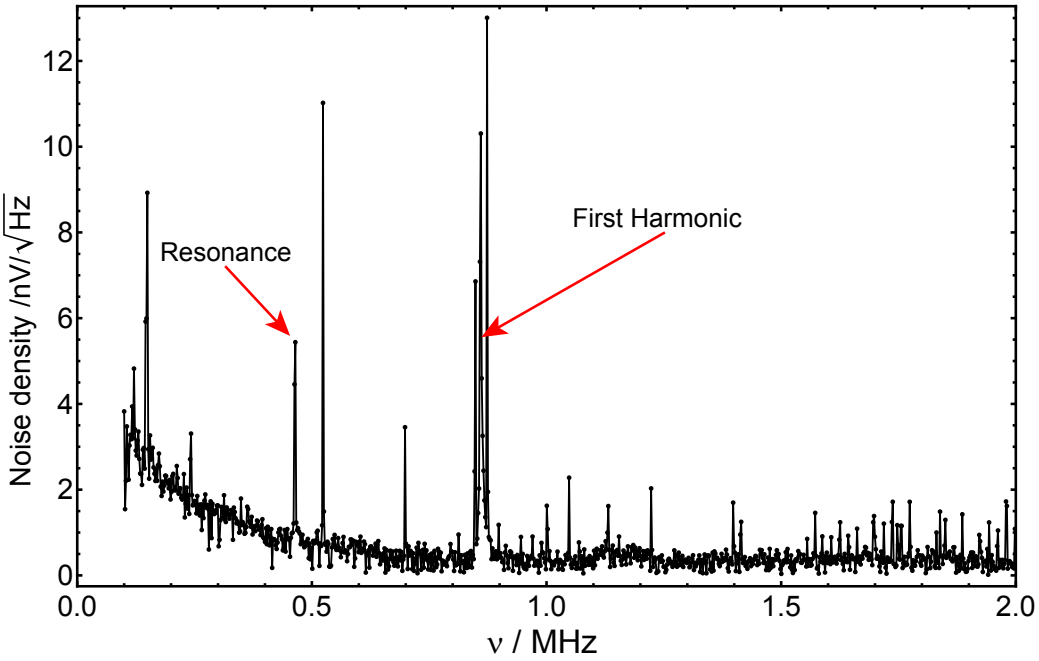

Figure 5.10: Noise spectrum at the ring electrode of the precision trap. With the prototype of the new switchable voltage source for the Penning traps the tank circuit resonance is observable with 1 mV external excitation.

the voltage source.

Further tests revealed that after all improvements the overall noise picked up by the detection circuit is very low as depicted in Fig. 5.10, except a few peaks whose origin remains unknown. However, already a weak excitation of the tank circuit revealed the resonance of the tank circuit as well as its first harmonic. Thus, it is very likely that first tests with ions can be carried out soon when the final version of the voltage source is produced.

Chapter 6

Results of first mass measurements of transuranium nuclides at TRIGA-TRAP

The main goal of the TRIGA-TRAP experiment (Chap. 4) is to perform mass measurements on neutron-rich nuclides. However, off-line mass measurements, have already been performed on several stable nuclides in the rare earth region [Ket10a, Smo12]. Within this work, after intensive studies of their chemical homologues, the first off-line mass measurements have been carried out on transuranium nuclides, using the newly implemented miniature RFQ upgrade of the laser ablation ion source (see Sect. 4.2). This upgrade enabled a more economic use of the target material, allowing a high-precision mass measurement with only 10^{15} atoms target material. The actual measurements were performed employing the TOF-ICR technique (Sect. 3.4.1).
Besides SHIPTRAP, where direct mass measurements on nobelium and lawrencium isotopes have been performed [Blo10, Dwo10, Ram12], TRIGA-TRAP is the only mass spectrometer worldwide performing direct mass measurements in the transuranium region. Nevertheless, providing such anchor points is important as no direct mass data exists in this region. Therefore the masses are mainly based on α decay spectroscopy, linking them to lighter nuclides.
Within this chapter the measurement as well as the evaluation procedure will be addressed (Sect. 6.1) and the impact of the new data in the transuranium region will be discussed (Sect. 6.2).

6.1 Measurement and evaluation procedure

The mass $M(N, Z)$ of an atom is measured at TRIGA-TRAP by the comparison of its cyclotron frequency to the cyclotron frequency of a reference ion of well-known mass. This is done by consecutive cyclotron frequency measurements of both species. The principle of this procedure is described in detail in [Kel03] with its actual application at TRIGA-TRAP

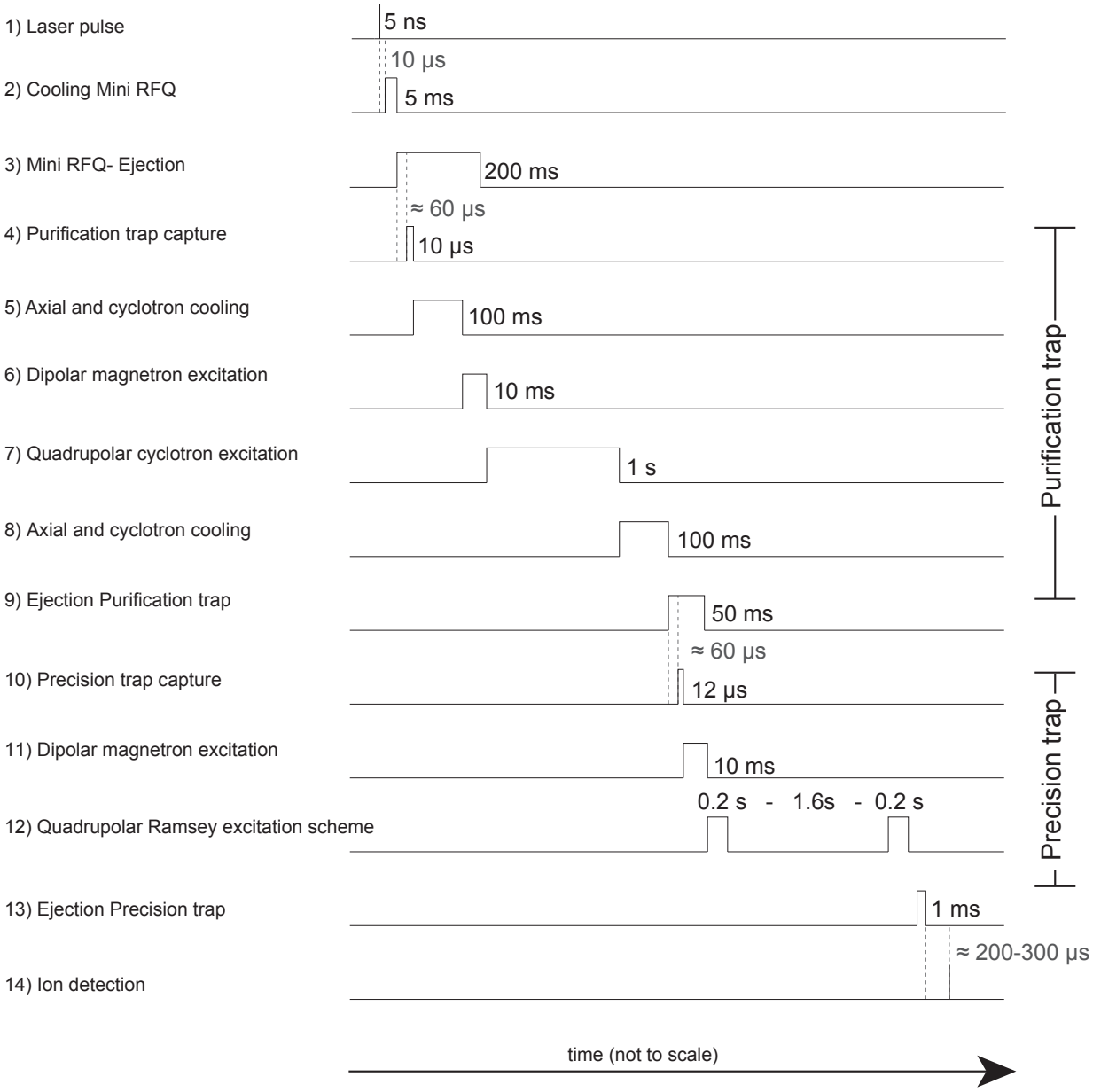

Figure 6.1: Measurement cycle for all measurements performed within this work. All approximate times scale with the mass of each ion specimen assuming $q = 1$. During a cyclotron frequency measurement, only the frequency of the excitation (11) is changed after each iteration. The length of the different time spans is not to scale.

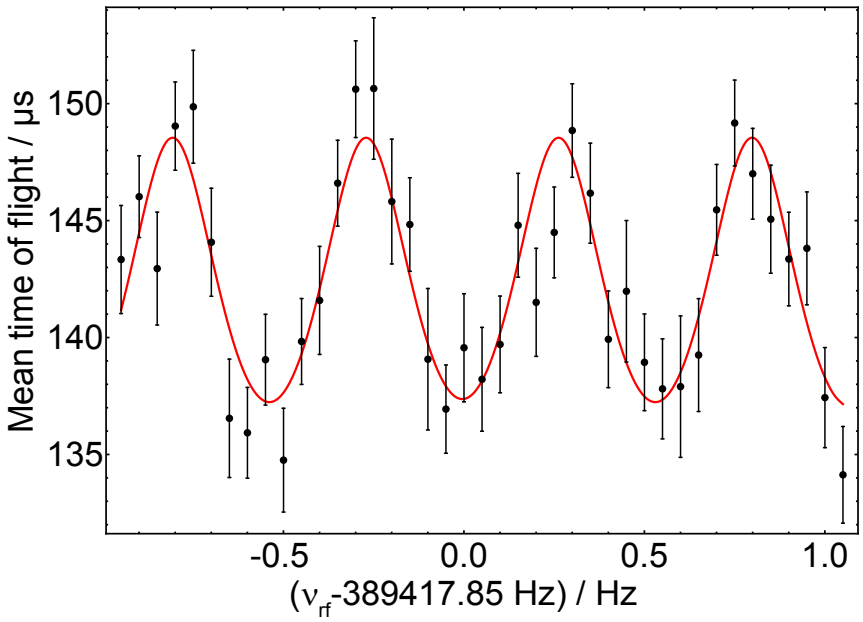

Figure 6.2: Ramsey time-of-flight ion cyclotron resonance of $^{12}C_{23}^{+}$ using an excitation pattern of 200 ms-1600 ms-200 ms. The mean time of flight is displayed as function of the quadrupolar excitation frequency in the precision trap driving the conversion from magnetron to modified cyclotron motion. The red line is the fit of the theoretical function [Kre07] to the data.

described in [Ket10b, Ket10a, Smo12].
The time frame of one measurement cycle from the ion production until its time-of-flight measurement is shown in Fig. 6.1. Here, it is assumed that the ions are produced in the laser ablation ion source (Sect. 4.2) as this was essential for the mass measurement discussed within this chapter. The ion production begins with a laser pulse of about 5 ns width (1). Shortly after this, when the ionization is finished and the ions are in the center of the mini RFQ, the potential of its back plate as well as the target is raised to ensure storage for the next 5 ms (2), during which the ion motions are cooled by interactions with the helium buffer gas. During this time either light or heavy ions can be selected by varying the dc-potential applied to the rods, already providing a very rough selection.

After cooling, the ions are extracted from the mini RFQ (3) by lowering the potential of its front electrode, and reach the purification trap after a flight time of about 60 μs. The trap is opened for 10 μs by lowering the potential of the left end cap and the corresponding correction electrode (4). In a first step, the ion cloud is just stored inside the trap without any active motion manipulation for 100 ms while the axial and modified cyclotron motions are cooled (5). Afterwards, the buffer gas cooling technique (Sect. 3.3.2) is employed starting with a 10 ms long simultaneous increase of the magnetron radius of all ion species by a dipolar excitation (6). One specific ion species is centered in the purification trap

by conversion of its magnetron motion to the reduced cyclotron motion, which is cooled very fast, applying a quadrupolar excitation (Sect. 3.3.1) for 1 s (7). In a final step, their remaining cyclotron excitation is cooled without any conversion (8) and they are subsequently ejected by lowering the potential of the right end cap and correction electrodes for 50 ms (9).
About 60 μs later the ions reach the precision trap and are captured again (10). A 10 ms long excitation of the magnetron motion (11) is followed by the conversion from magnetron to reduced cyclotron motion (12). For the measurements presented here, the two pulse Ramsey scheme was applied with 0.2 s long excitation pulses and 1.6 s waiting time in between. Practically reasonable times of the total Ramsey scheme can be applied between 100 ms and 4 s. For longer storage times damping due to residual gas limits the achievable precision. Finally, the ions are ejected from the precision trap (13) and guided to a detector (14), where the time difference between ejection and detection is measured. This cycle is repeated multiple times, varying the excitation frequency in (12) around the free cyclotron frequency ν_c of the trapped ion species. At TRIGA-TRAP, the frequency is changed in 41 steps around the expected value for ν_c, with the typical step size of one tenth of the inverse storage time, which was here 0.05 Hz. One iteration of 41 cycles is referred to as a scan.
A typical time-of-flight resonance of the carbon cluster ion $^{12}C_{23}^{+}$ with 22 scans containing in total 566 ions is displayed in Fig. 6.2. The mean time of flights are calculated for all ions recorded at the same frequency values. Then the theoretical line shape (red solid line) [Kre07] is fitted to the data with a least-squares determination, from which the cyclotron frequency at the time-of-flight minimum is obtained including its uncertainty. The cyclotron frequency is here determined to 389471.846(7) Hz. The theoretical background of the TOF-ICR technique is discussed in detail in Sect. 3.4.1.
For the consideration of contaminant ions an evaluation procedure dividing the time-of-flight resonance in count rate classes is well established [Kel03]. This would require a total ion number of a few thousand. Therefore, it could not be applied here. Instead the number of ions considered in the evaluation was limited to maximum triple ion events since no frequency shifts could be observed compared to single ion events with this restriction.
As given in Eq. (3.43), the mass of an atom is calculated from the cyclotron frequency ratio of the ion of interest and a reference mass. With the ToF-ICR technique it is not possible to measure two cyclotron frequencies simultaneously. This is compensated by linearly interpolating the reference frequency to the center time of the measurement of the ion of interest, which is used to calculate the frequency ratio r_i. Additional non-linear fluctuations of the magnetic field were investigated in [Ket10b] and are considered by quadratically adding the uncertainty of $6(2) \cdot 10^{-11}/\mathrm{min} \times \Delta t$ to the statistical uncertainties of the frequency ratios with the time difference between the two reference measurements Δt, being referred to as σ_i. The mean frequency ratio r is then calculated as the error weighted mean with

Cluster ion	Reference cluster	r	Δr / 10^{-9}	ΔME / keV	χ^2
$^{12}C_{22}^+$	$^{12}C_{21}^+$	1.0476191447(56)	6.6(5.6)	-1.6(1.3)	0.47
$^{12}C_{23}^+$	$^{12}C_{22}^+$	1.0454546446(64)	-4.7(6.4)	1.2(1.6)	0.81
$^{12}C_{23}^+$	$^{12}C_{21}^+$	1.0952383114(73)	-8.9(7.3)	2.1(1.7)	1.16

Table 6.1: Calibration measurements of carbon cluster ions. The deviation Δr of the measured cyclotron frequency ratio r from the theoretical value was determined. For clarity the mass excess, which is in theory zero, is given, as well as the χ^2 of the data distribution.

the internal and external errors σ_{int} and σ_{ext}:

$$r = \frac{\sum_i \frac{r_i}{\sigma_i^2}}{\sum_i \sigma_i^{-2}} \tag{6.1}$$

$$\sigma_{int} = \frac{1}{\sqrt{\sum_i \sigma_i^{-2}}} \tag{6.2}$$

$$\sigma_{ext} = \sqrt{\frac{1}{N-1}\sum_i \frac{(r_i - r)^2}{\sigma_i^{-2}}} \cdot \sigma_{int} \ . \tag{6.3}$$

The external error accounts for errors beyond the statistical fluctuations, represented by a reduced $\chi^2 > 1$. To be on the safe side, the maximum of σ_{int} and σ_{ext} is taken as the uncertainty δr of r.

Effects, like a trap misalignment in the magnetic field may cause small frequency shifts. These result in a shift in the calculated mass of the ion of interest, depending on the mass difference to the reference ion as pointed out in Eq. (3.45). Although carbon cluster ions provide a reference having a mass close to every ion of interest, this mass shift can be noticeable. Thus, carbon cluster ions are well-suited for the investigation of this effect. This has been done intensively around the heavy mass region in [Ket10b], but since the trap alignment was changed in the mean time, these measurements had to be repeated. As all nuclides investigated within this work populate a very limited mass region, this was done locally. All three possible frequency ratios between the carbon clusters $^{12}C_{21,22,23}^+$ were recorded and compared. The determined frequency ratios are shown in Tab. 6.1. Two of the recorded frequency ratios deviate slightly from the theoretical value, indicating a small mass dependent shift. The shift of r was calculated as the weighted mean per mass unit, obtained from each frequency ratio. This was found to be in agreement with zero:

$$\varepsilon_{shift} = -1.5(2.3) \cdot 10^{-10} \,/\mathrm{u} \ . \tag{6.4}$$

Nevertheless, it is still considered in the evaluation process.

Systematic effects due to a non-stabilized trap tube temperature as well as a non-stabilized pressure in the liquid helium dewar of the superconducting magnet were found in earlier work. They were eliminated by installing stabilization systems and are not considered here

Ion	r	$\delta r/r$ / 10^{-9}	ME^{atom}_{TT} / keV	$ME^{atom}_{AME2012}$ / keV	ΔME^{atom} / keV
$^{241}Am^{16}O^{+}$	0.9736807966(72)	7.4	52936.9(1.8)	52936.2(1.8)	0.7(2.5)
$^{243}Am^{16}O^{+}$	0.9812738087(56)	5.7	57176.2(1.4)	57176.3(2.3)	-0.1(2.7)
$^{244}Pu^{16}O^{+}$	0.9850723904(72)	7.3	59806.2(1.8)	59807(5)	-0.8(5.3)
$^{249}Cf^{16}O^{+}$	1.0040521297(52)	5.2	69718.1(1.3)	69726.0(2.2)	-7.9(2.5)

Table 6.2: Result of the mass measurements in the actinoide region. The ion chosen for the mass measurement is given, together with the frequency ratio to the reference ion $^{12}C^{+}_{22}$ and the relative measurement error $\delta r/r$. The mass excesses refer to the atom measured at TRIGA-TRAP and the value given in the AME2012 [Wan12] with their differences to the AME2012 $\Delta ME^{atom} = ME^{atom}_{TT} - ME^{atom}_{AME2012}$.

to be relevant any longer (See Sect. 3.2). For a detailed description of these systems, the reader is referred to [Smo12].
The final integration into the Atomic-Mass Evaluation is done by [Wan13] and is described briefly in the next section.

6.2 Evaluation results

All measurements have been performed with the ToF-resonance technique, using a Ramsey excitation scheme with two 0.2 s pulses and 1.6 s waiting time in between. For all mass measurements the carbon cluster $^{12}C^{+}_{22}$ was used as reference. The ion production took place in the laser ablation ion source as described in Sect. 4.2. During the entire measurement campaign, the pressure in the liquid helium reservoir as well as the temperature of the magnet bore were stabilized to ± 0.25 K and ± 0.5 mbar, respectively. During this time no severe deviations from the set values were observed. The result of the measurements obtained with the evaluation procedure introduced in Sect. 6.1 is presented in Tab. 6.2. It has to be noted, that only oxide ions were obtained from the target (see. Sect. 4.2). Nevertheless, this does not affect the measurement precision since the molecular binding energy is sufficiently below the uncertainty of the measurements, more precisely in the range of eV. Thus, the mass excess of the nuclide of interest could be calculated by subtractions of the mass excess of oxygen.

The masses of nuclides in this region of the nuclide chart are mainly determined by self consistent loops[1] with the absolute value being fixed via α decay spectroscopy to an absolute mass measurement below uranium. Here the dependencies are relatively simple as depicted in Fig. 6.3. In general the α decay chains (horizontal) are separate and just interconnected via nuclear reactions of uranium as well as plutonium isotopes. In most other cases connections exist, if a nucleus decays with an additional β transition. This

[1] A loop in the AME network (see Fig. 6.3) is created if two nuclides are connected via at least two different paths. The mass of all nuclides in a loop is overdetermined.

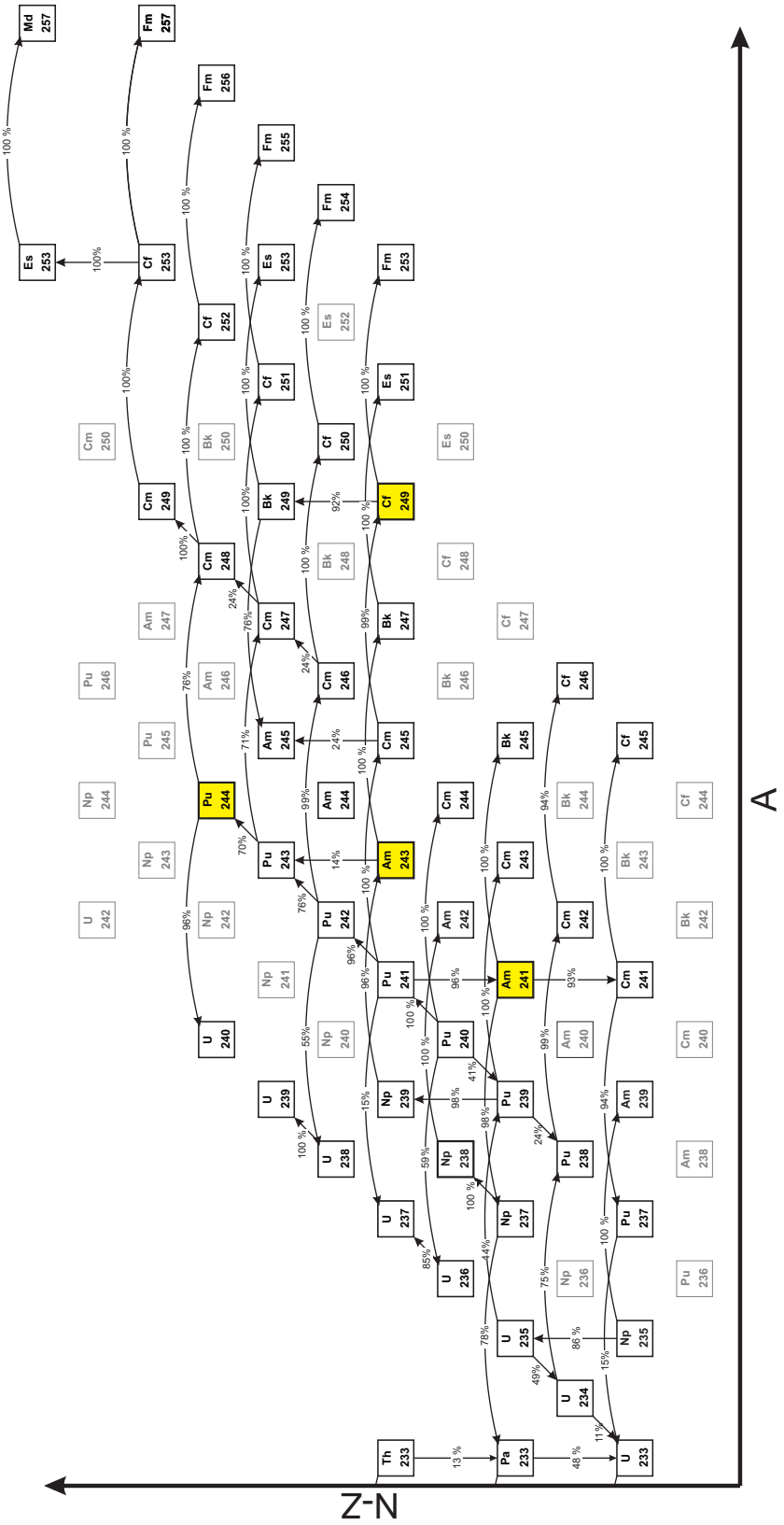

Figure 6.3: Mass links in the AME2012 system. The nuclides whose masses were measured within this work are marked in yellow. The arrows point in the direction of the strongest dependency with the relative contribution of this connection. However, one connection influences both nuclides. Links with a large uncertainty are not displayed as well. For a complete list of dependencies the reader is referred to [Aud12a, Wan12].

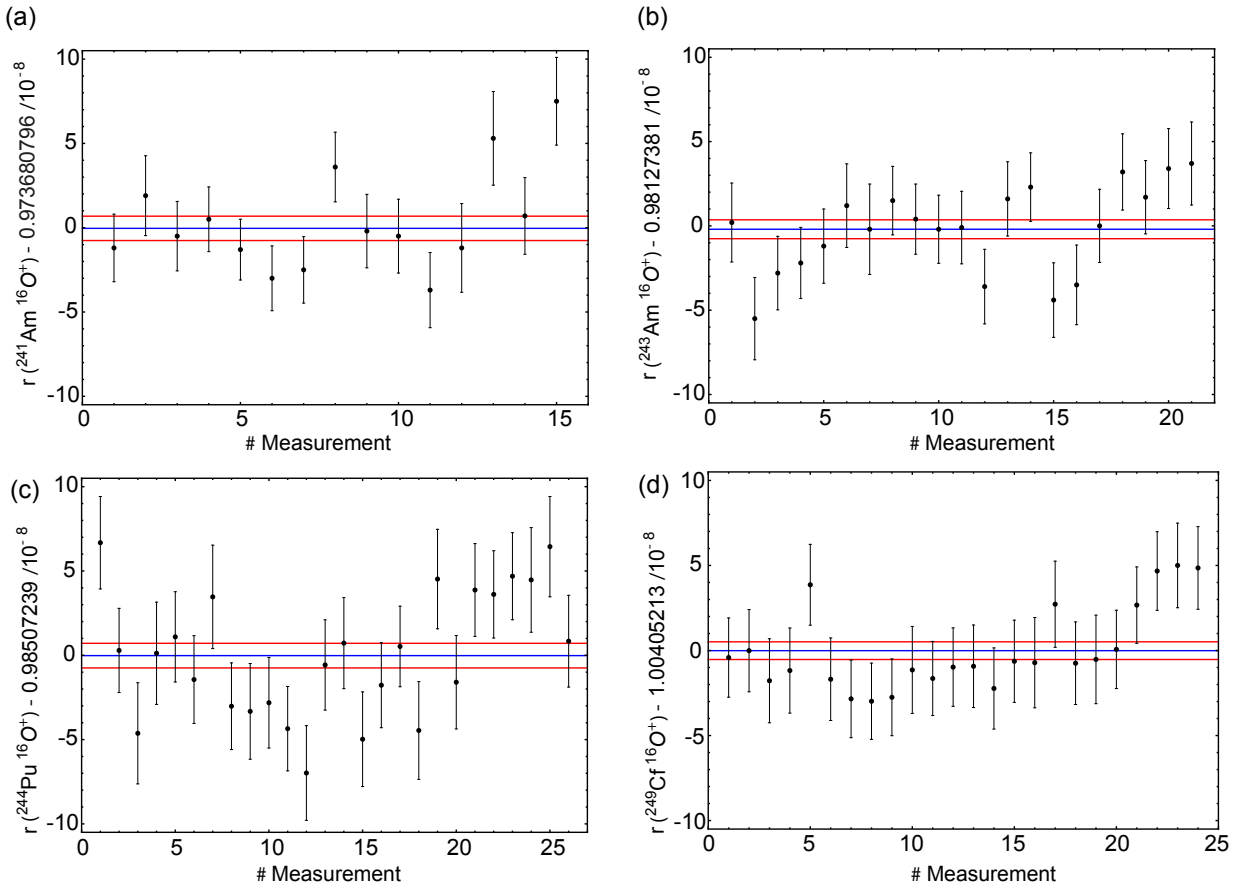

Figure 6.4: Frequency ratios measured in the actinoide region within this thesis. Here the recorded frequency ratios of the four nuclides are presented. In all cases $^{12}C_{22}^{+}$ was used as reference. The blue lines indicate the weighted mean with the according standard deviations (red lines). Note that the values are not corrected by the mass dependent shift.

region was rarely studied with (n,γ) or similar reactions.

For the first measurement ^{241}Am was chosen in order to have a direct comparison to the measurement from 2010 [Ket10a]. At that time the ionization efficiency was very low, and the mass measurement, performed with a relative uncertainty of $\delta m/m = 2.5 \times 10^{-7}$, deviated -79(59) keV from the mass published in the AME2003. Another advantage of this first candidate in the actinoide region is the comparably long half-life of 432.2 y, making it easy to handle, in combination with the large availability due to its application in industry. It turned out that the ion production efficiency improved by more than one order of magnitude so that it was possible to record 15 resonances with in total 8738 ions of ^{241}Am^{16}O. In Fig. 6.4 (a) the measured frequency ratios are presented together with their mean (blue) and standard deviations (red). The value, corrected by the mass-dependent shift from Eq. (6.4), is shown in Tab. 6.2. From this the mass excess of ME_{TT} = 52936.9(1.8) keV

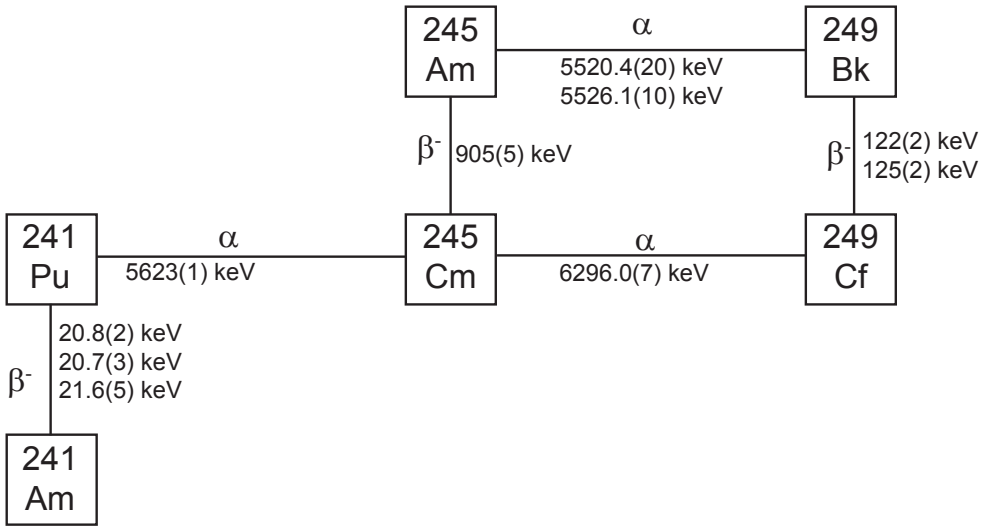

Figure 6.5: Transitions linked to ^{249}Cf including their energies. The energies are taken from [Wan12].

could be calculated, which is well in agreement with the value $ME_{AME} = 52936.2(1.8)$ keV published in the AME2012 [Wan12].

The mass of ^{243}Am was determined since it allows to obtain information on the deformed shell closure at $N = 152$. It is used as an anchor point providing additional confidence to the mass measurements of ^{241}Am and ^{244}Pu, to which it is connected via four and two links, respectively. In total 9789 ions were recorded (see Fig. 6.4 (b)). This resulted in a mass excess of $ME_{TT} = 57176.2(1.4)$ keV, with a smaller uncertainty than in the AME2012 where $ME_{AME} = 57176.3(2.3)$ keV was published.

^{244}Pu was chosen, as its mass excess with $ME_{AME} = 59807(5)$ keV, mainly determined by the transition ^{244}Pu(d,t)^{243}Pu, is not known very precisely. This comparably large uncertainty dominates the uncertainty of the ^{244}Pu α decay chain as well as the uncertainty of the ^{249}Cm α decay chain. Since both are also crossing $N = 152$ the improvement of these chains can also help to understand the deformed shell-closure. In addition ^{244}Pu is the nuclide with the largest neutron excess that can be used as target material in superheavy element research motivating the verification of the absolute mass. Thus, a measurement series with 26 frequency ratios containing 16299 ions was performed (see Fig. 6.4 (c)), yielding $ME_{TT} = 59806.2(1.8)$ keV, which is an improvement by more than a factor of 2.5 compared to the literature value.

The fourth investigated nuclide, ^{249}Cf, is the closest one to the magic neutron number $N = 152$. Here 24 resonances with 13818 ions were recorded (see Fig. 6.4 (d)). A comparison of $ME_{AME} = 69726.0(2.2)$ keV and the measured $ME_{TT} = 69718.1(1.3)$ keV shows a significant deviation of 7.9 keV, i.e. more than 3σ. As ^{249}Cf is connected to ^{241}Am via

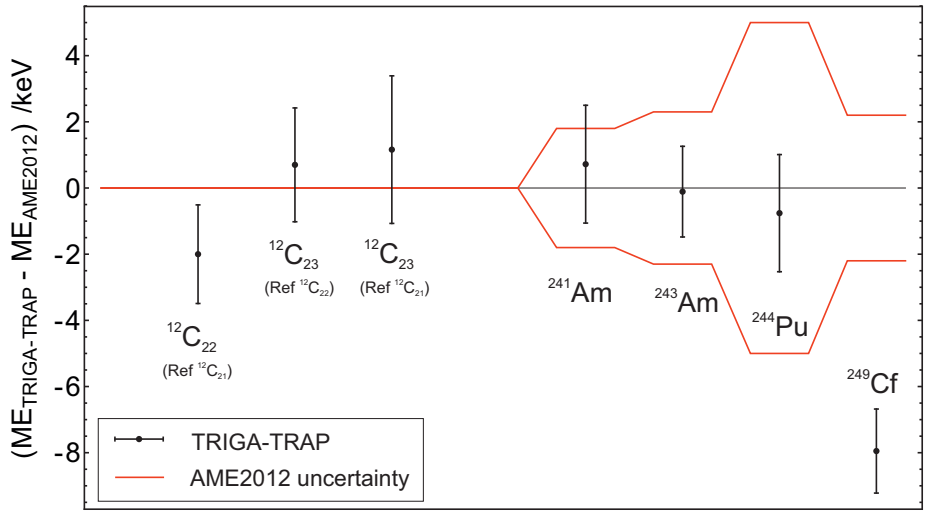

Figure 6.6: Illustration of the results from Tabs. 6.1 and 6.2. The latter are corrected by the mass dependent shift from Eq. (6.4). The solid red lines mark the 1σ error.

three decays, this indicates that either one of the α decay energies or the β^- decay energy is wrong. Additionally, the nuclides ^{245}Cm, ^{245}Am and ^{249}Bk create a loop with ^{249}Cf, (see Fig. 6.5) whose consistency is affected as well. A detailed description of the occurring discrepancies as well as their treatment is given later.
These final results are shown in Fig. 6.6 relative to the values published in the AME2012 [Wan12]. The solid red lines mark the 1σ error and the zero line the AME2012 values.

Although a relatively small number of transitions exists in the network displayed in Fig. 6.3 every nuclide, which is part of a loop is overdetermined. This is usually not the case for heavy nuclides in the α decay chains due to a lack of experimental data. However, all nuclides examined within this work are part of a loop. Only ^{244}Pu can be regarded as relatively decoupled since the uncertainties of the transitions connecting its decay chain to the remaining nuclides are large compared to the measurement performed at TRIGA-TRAP. All connections are considered in the evaluation by performing a least-squares fit to the experimentally determined mass data. This is done by representing an overdetermined system by a set of linear equations

$$\sum_{\mu=1}^{M} k_i^{\mu} m_{\mu} = q_i \pm \delta q_i \ . \tag{6.5}$$

Here, a number of M different masses m_{μ} of the nuclides μ are multiplied with a constant k_i^{μ} of the linking transition. q_i with the uncertainty δq_i denote the experimental data [Aud12b]. Computational effort is minimized, as before the evaluation process is started, all equations with only one parameter are excluded, until each parameter occurs

at least twice. This is usually applicable for the heavy parts of the α decay chains as shown partly in Fig. 6.3. Thus, only the over-determined nuclides remain in the evaluation process, being called primary nuclides. The other nuclides are called secondary, tertiary, etc.. Their absolute masses are determined considering their link to a primary, secondary, etc. nuclide [Aud12b].

6.2.1 Influence on the Atomic Mass Evaluation

Over-determination is obviously not problematic, if the improved mass value and the AME value agree. However, in the case of ^{249}Cf this seems to become challenging and may only be resolved by removing at least one transition within this loop. Nevertheless, in a first evaluation approach, the data from TRIGA-TRAP was included regularly into the AME2012 and all measurement data was trusted equally. This resulted in the mass shifts as displayed in Fig. 6.7 (a). The mass difference of ^{249}Cf caused a shift of the mass of 234 nuclides, mostly in the range of -2 keV to -3 keV. Two α decay chains (red boxes) including ^{249}Cf are shifted by -5 keV. This is already not acceptable, since the absolute mass of ^{249}Cf in the new AME2012*[2] disagrees with the mass measured at TRIGA-TRAP. In addition the χ^2 of the loop formed by ^{245}Cm, ^{245}Am, ^{249}Bk and ^{249}Cf (see Fig. 6.5) increased by 26 compared to the AME2012 [Wan13].
Finding the origin of this discrepancy is rather challenging. Since the mass of ^{241}Am was confirmed within this work and the β^- decay energy of ^{241}Pu has been confirmed by several different groups, also this mass is secured. Now it is questionable, whether ^{245}Cm$(\alpha)^{241}$Pu is correct or not. If not, it would shift the entire loop. It is astonishing that for ^{249}Bk$(\alpha)^{245}$Am two different decay energies with a significant deviation of 5.7 keV were measured. In particular, since the group that measured the higher value also determined the decay energy of ^{249}Cf$(\alpha)^{245}$Cm and ^{245}Cm$(\alpha)^{241}$Pu, all three involved α decay energies should be questioned. Regarding the β^- energies at least the decay ^{249}Cf$(\beta^-)^{249}$Bk was confirmed independently by two groups, while ^{245}Cm$(\beta^-)^{245}$Am was only investigated by one group with a comparably large uncertainty of 5 keV [Bro55].
Since one can not be certain on, which part of this loop is wrong, a second approach is based on a decoupling of ^{249}Cf from the remaining nuclides. This is achieved by increasing the uncertainty of the three questionable α decays to 6 keV. The result of a subsequent mass evaluation is shown in Fig. 6.7 (b). Now the masses of the nuclides in the two α decay chains (red) are shifted by 8 keV. Here, including ^{245}Am and ^{245}Cm, the masses of 20 nuclides are changed, while the remaining nuclides are unaffected. Without measuring more masses within this loop, this approach is favored, since the χ^2 obtained in this evaluation keeps unchanged with respect to the AME2012.
In addition the recent mass measurement had an effect on the uncertainty of some nuclides as depicted in Fig. 6.8, where the relative change of the mass uncertainty is displayed. In total the masses of 84 nuclides were improved. Only the uncertainty of ^{245}Cm became larger

[2] The evaluation of the AME2012 including the TRIGA-TRAP data is being referred to as AME2012*

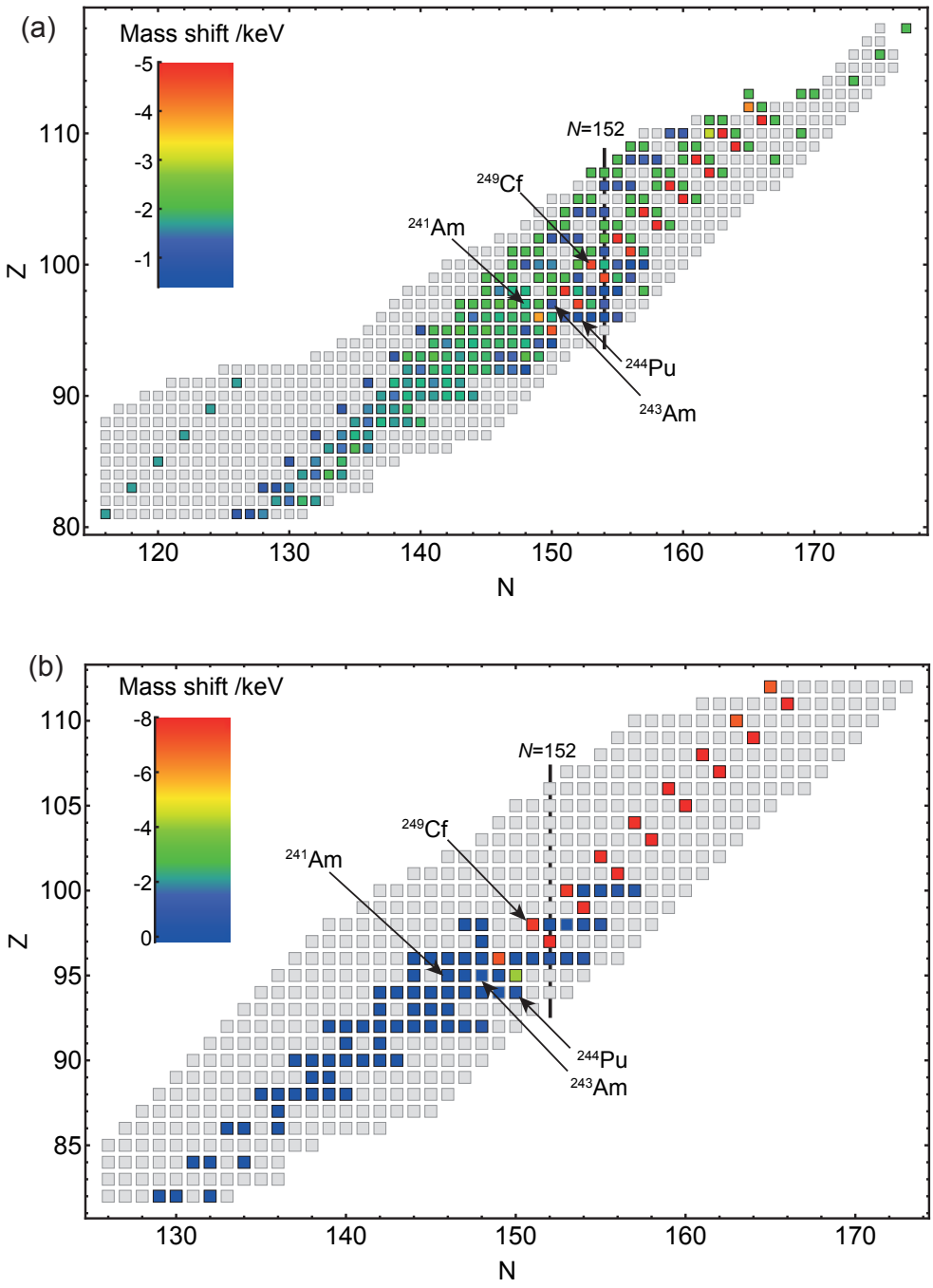

Figure 6.7: Mass shift of all nuclides influenced by the latest mass measurements at TRIGA-TRAP during integration into the AME2012 [Wan12]. Due to a mass deviation found in the case of ^{249}Cf, two different approaches have been used, with an either equal treatment of all nuclides (a) or a decoupling of ^{249}Cf from the remaining nuclides. The integration into the AME was done by [Wan13].

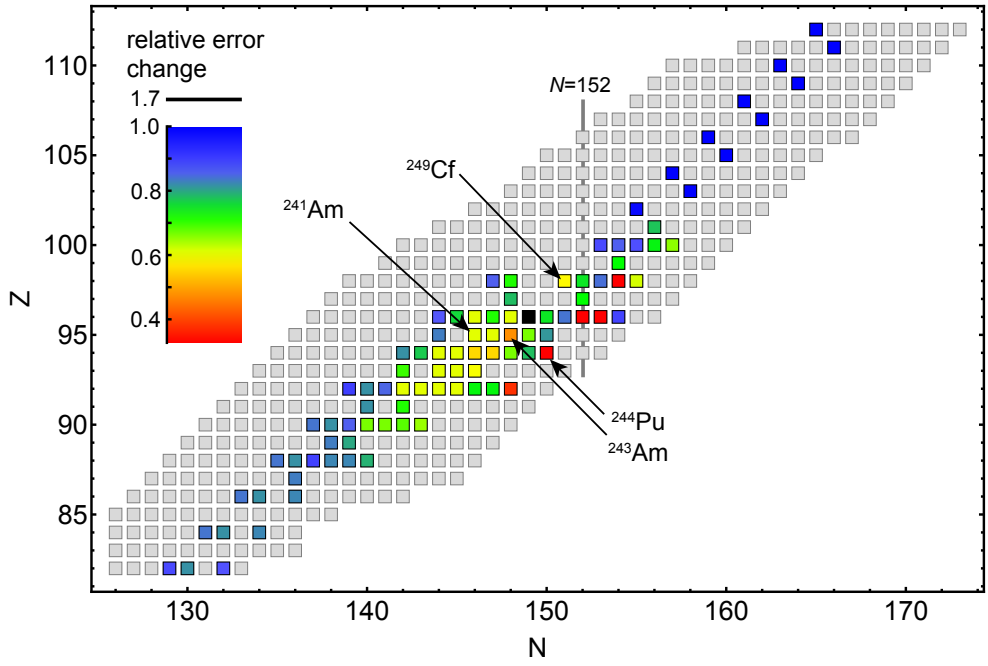

Figure 6.8: Relative change in the mass uncertainty by including the recent mass measurement data into the AME2012. Due to the decoupling procedure the uncertainty of ^{245}Cm is increased.

by a factor of 1.7 due to the decoupling procedure. The largest improvement was achieved for all nuclides in the α decay chain of ^{244}Pu as well as their strongly coupled neighbors, as shown in Fig. 6.3. While the uncertainties of the closest neighbors are changed by at least a factor of 0.4, the decrease propagates up to ^{257}Fm. Although, the mass measurements on ^{241,243}Am did not have a tremendously better uncertainty than the AME2012, their contribution influenced several nuclides with respect to their error bars.
The implementation of this new data changed the links in the AME2012*, as shown in Fig. 6.9. Compared to the links in the AME2012 (see Fig. 6.3) new connections between the measured nuclides and ^{12}C were established (blue) with a relative influence between 35% and 98%. This also changed the contribution of at least 45 other links, of which 17 were changed by more than 20 percentage points [Wan13].

6.2.2 Discussion of the new mass values

A comparison of the masses of the investigated nuclides and the predictions of three mass models is provided in Fig. 6.10. The mass excesses obtained from the finite range droplet model (FRDM95) [Möl95], the Duflo-Zuker mass model (DUZU95) [Duf95] and the Hartree-Fock-Bogoliubov model HFB-21 [Gor10] were used. The model by Duflo and Zuker predicts the mass data excellently with an σ_{rms} below 100 keV for these four masses.

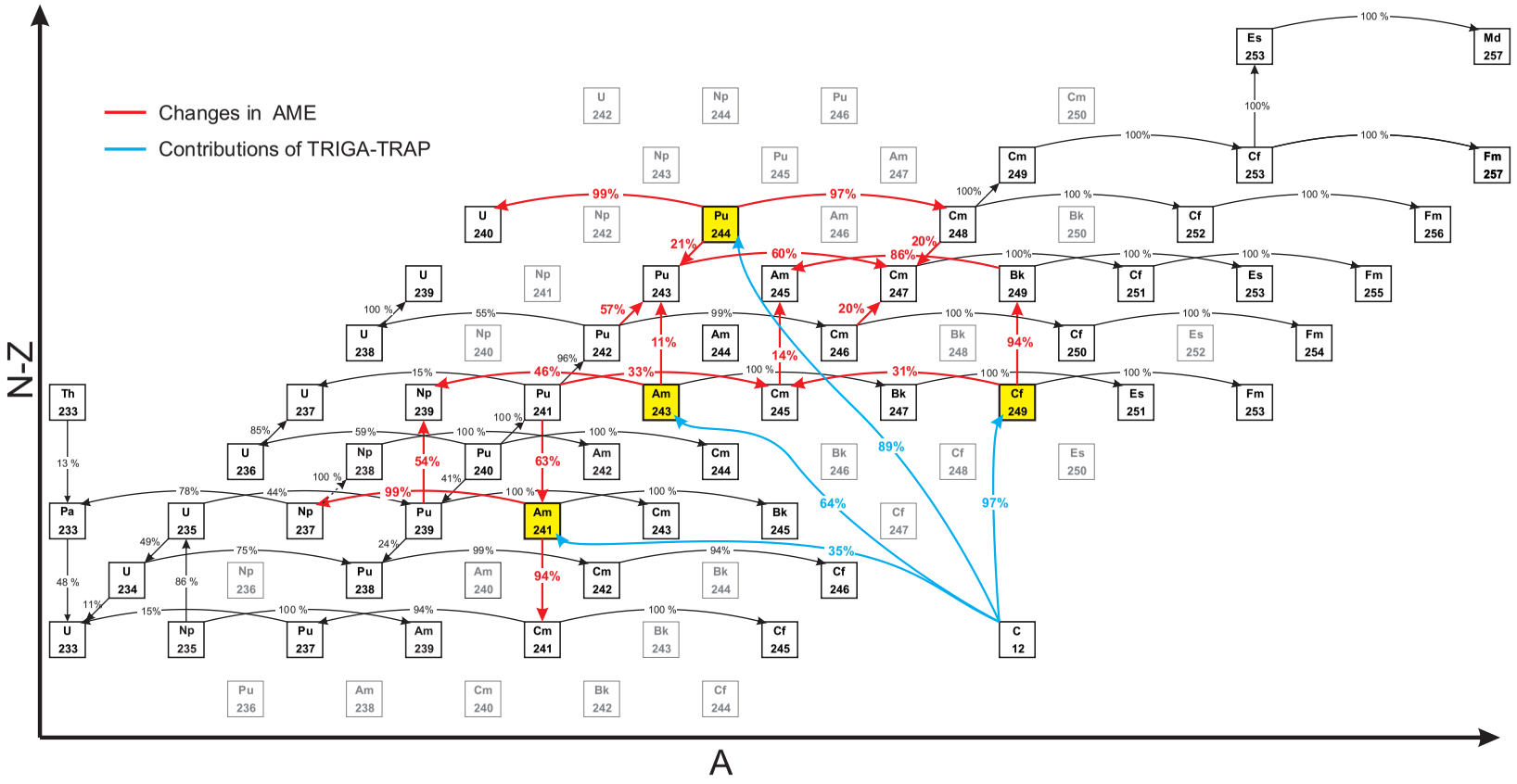

Figure 6.9: Links in the AME2012* system. The mass measurements at TRIGA-TRAP established four new connections, each to ^{12}C, which affected other contributions as well. Here only the major contributions are displayed.

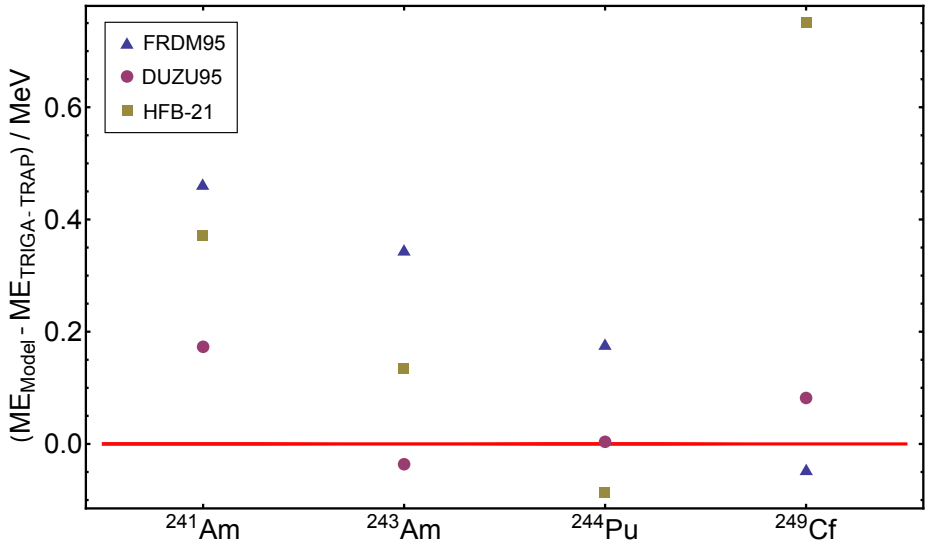

Figure 6.10: Comparison of the measured masses with mass model predictions. The red horizontal line denotes the TRIGA-TRAP masses, with error bars being too small to be visible on this scale.

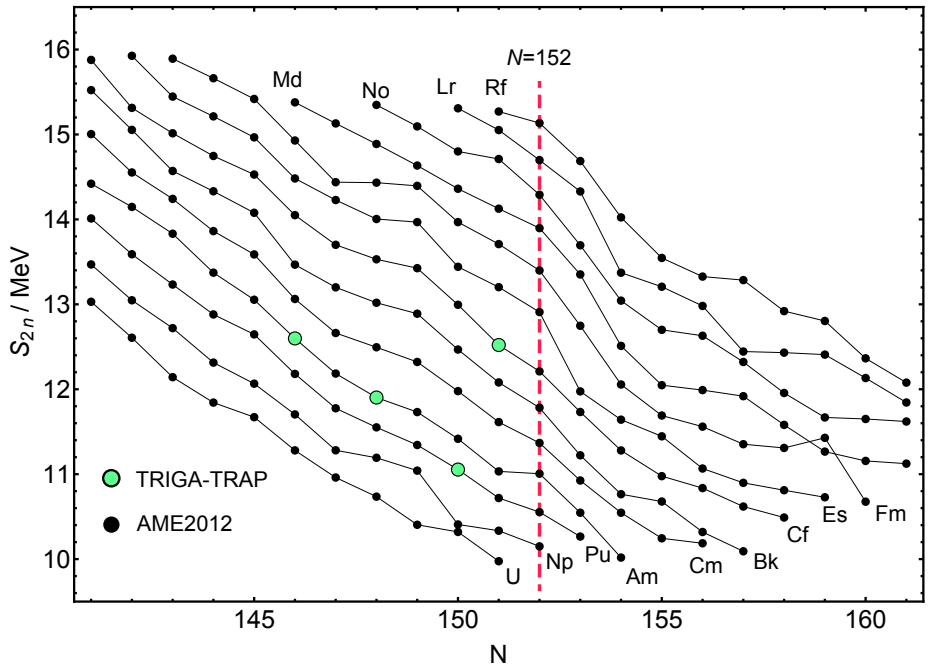

Figure 6.11: Two-neutron separation energy S_{2n} as function of the neutron number N in the realm of the deformed shell closure $N = 152$. The nuclides measured at TRIGA-TRAP are marked in green. The S_{2n} calculation is based on the AME2012*.

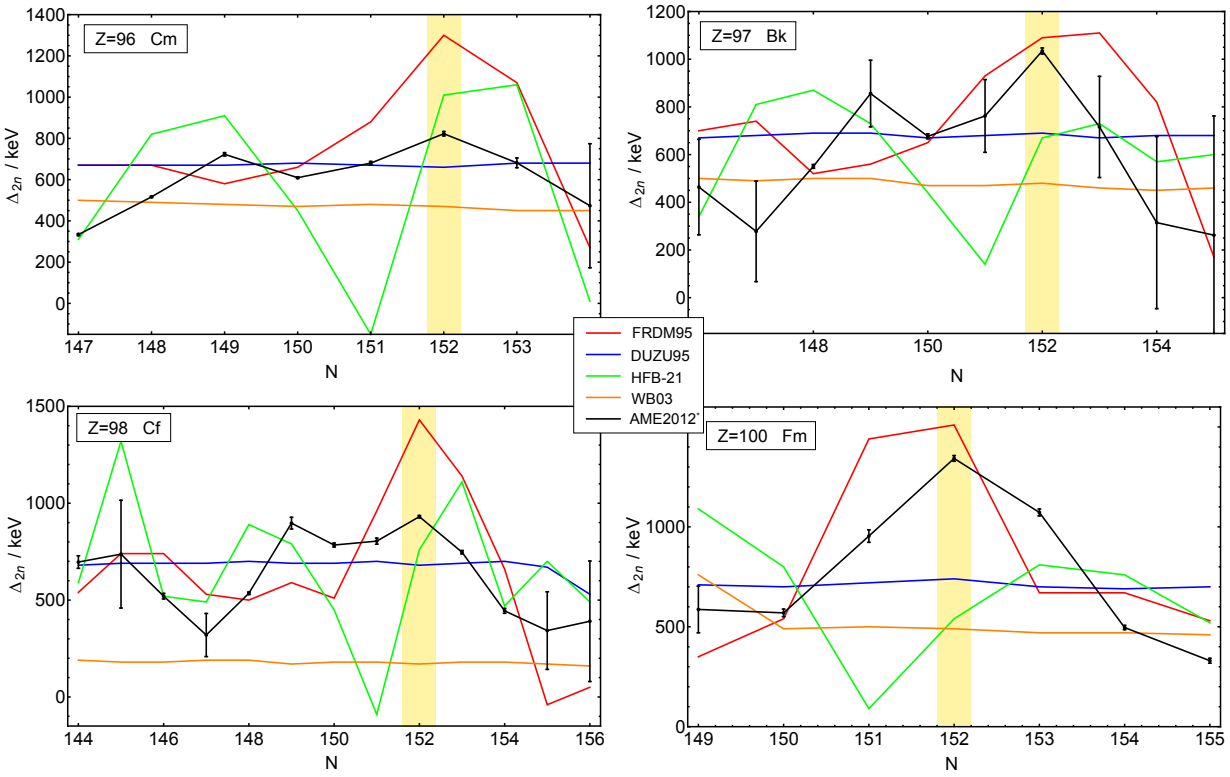

Figure 6.12: Shell gap parameter Δ_{2n} calculated from Eq. (2.5). Together with the experimental data from AME2012*(black) Δ_{2n} obtained from several mass models is displayed.

FRDM95 as well as HFB-21 have a significantly less precise predictive power for these four nuclides. In general both overestimate the mass excess.
The results from the Bethe-Weizsäcker mass formula are not displayed here, as it underestimates the first three nuclides by 3 MeV to 5 MeV and completely fails for ^{249}Cf.
Precise knowledge of nuclear masses can provide information about nuclear structure. Here, the calculation of the two-neutron separation energies S_{2n} employing Eq. (2.3) is used to display the shell closure at the magic neutron number $N = 152$. S_{2n} is shown in Fig. 6.11 as function of the neutron number, with the latest mass measurements performed at TRIGA-TRAP marked in green. The shell closure manifests as a drop in S_{2n} at $N = 152$ being clearly visible for higher Z elements. This effect seems to vanish for lower Z and to blend into the global linear trend apart the shell closure.

Such effects can be displayed easier using the shell gap parameter Δ_{2n} introduced in Eq. (2.5). Shell closures are here reproduced as a pronounced maximum. In Fig. 6.12 this is shown for the Cm, Bk, Cf and Fm isotopic chains since their mass value was affected most by the latest TRIGA-TRAP mass measurements. The experimental values (black) were taken from the AME2012 including the TRIGA-TRAP data (referred to as AME2012*). It shows a global maximum at $N = 152$ for all four elements, which increases only for Fm above 1.3 MeV. Surprisingly, the shell gap parameter features a second maximum for the

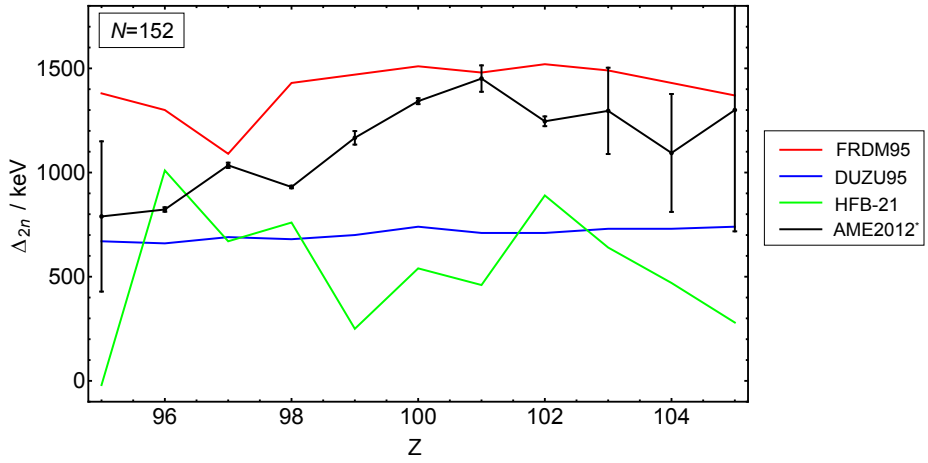

Figure 6.13: Shell gap parameter Δ_{2n} calculated from Eq. (2.5) of experimental and theoretical data at N=152 as function of the proton number. Due to the lack of experimental mass data, the shell gap parameters are partly based on extrapolations.

remaining three elements at $N = 149$ and is less pronounced for the lower Z elements as indicated in Fig. 6.11.
For comparison the shell gap parameters obtained from model calculations from the FRDM95 (red) [Möl95], the DUZU95 (blue) [Duf95], the HFB-21 (green) [Gor10] as well as the Bethe-Weizsäcker mass formula WB03 (orange) are calculated. DUZU95 and WB03 do not reproduce the shell gap at all. HFB-21 predicts the global maximum with an offset at $N = 153$ next to a very strong global minimum at $N = 151$. Nevertheless, it is the only mass model from these examples being capable to reproduce the second maximum, which is shifted in the model by one neutron number down to $N = 148$. The FRDM95 is the only model from the selection, which predicts the global maximum at the correct neutron number, except for Bk. Fig. 6.12 shows that not only the absolute prediction of nuclear masses but also their difference is not perfect. Moreover, the actual existing deformed shell gap is not reproduced at the correct neutron number. This is most likely due to intrinsic assumptions of the models that also causes their predictions for the next spherical shell closure to deviate.
It is also expected that the two-neutron separation energies as well as other nuclear properties change as function of the proton number Z. The properties of the deformed shell gap at $N = 152$ are not understood, especially at lower Z [Mak07]. This is indicated in Fig. 6.13 for Δ_{2n} as function of the proton number. The experimental mass data, partly based on extrapolations, features a maximum of Δ_{2n} at $Z = 101$. The FRDM95 model reproduces a somewhat similar trend, while the other two models fail completely. For a detailed understanding, more experimental data as well as theoretical work are required.

Chapter 7

Conclusions and Outlook

Within this work, shell structure effect studies were initiated in the heavy element region with the Penning-trap mass spectrometer TRIGA-TRAP. The masses of four transuranium nuclides have been directly measured relative to ^{12}C for the first time. This was enabled by an improvement of the existing laser ablation ion source. The second part of this work was the implementation of a non-destructive ion detection, employing the Fourier transform ion cyclotron resonance (FT-ICR) technique for mass measurements with ultimately a single ion. A low-noise amplifier, operating at liquid helium temperatures, has been adapted to the needs of the TRIGA-TRAP experiment. Its capability to equally amplify signals between 1 kHz and 10 MHz was demonstrated. This covers the entire cyclotron frequency range from 400 kHz to 3.6 MHz resulting from the large q/m range being studied at TRIGA TRAP. It has been demonstrated that even at low frequencies the voltage noise density remains low, i.e. 1.66(5) nV/$\sqrt{\text{Hz}}$ at 500 kHz, while it does not exceed 1 nV/$\sqrt{\text{Hz}}$ in the white noise regime. The current noise of the amplifier was determined to 2.5(2.4) fA/$\sqrt{\text{Hz}}$. This is sufficient for the amplification of a voltage signal, from a tank circuit of high quality formed of two trap electrode segments and a resonator together acting as a band-pass filter. The high-Q resonator was built, and tuned for cyclotron frequency measurements in the transuranium region. In an unloaded set up, it provides a Q-value of $27(2) \times 10^3$. However, when it is connected to the trap, this drops to values between 1500 and 3000. The resonance frequency can be shifted over a range of about 80 kHz using capacitive diodes. Thereby almost all transuranium ions available off-line would be reachable for FT-ICR mass measurements. However, it turned out that the noise caused by switchable voltage sources for the trap electrodes is several orders of magnitude higher than the induced ion signals. To this end, a new voltage source was developed [Ket14], whose prototype delivered promising data.

Furthermore, the existing laser ablation ion source was improved by the development and set up of a miniature RFQ. The ions are produced on the target surface inside the RFQ where they are subsequently stored and buffer-gas cooled before sending them to the trap. This development enabled mass measurements with only 10^{15} atoms target material, which, solved in nitric acid, is placed on a roughened Sigradur surface, where the solvent is dried, yielding mainly the oxide ions. Compared to earlier work this is an efficiency increase of

more than an order of magnitude. This enabled TRIGA-TRAP to extend its area of reachable nuclides into the transuranium region in which so far only SHIPTRAP had performed direct mass measurements.
The masses of the radioactive nuclides ^{241,243}Am, ^{244}Pu and ^{249}Cf with half-lives between 432.2 years and $8{\cdot}10^7$ years were measured employing the time-of-flight ion-cyclotron-resonance (ToF-ICR) technique. Mass uncertainties as low as 2 keV/c^2 have been demonstrated allowing for an improvement of the ^{244}Pu mass error by more than a factor of 2.5. While the masses of the Am isotopes were found to be in good agreement with the AME2012, the mass of ^{249}Cf deviates by 7.9(2.5) keV. The implementation into the existing AME2012 data for this nuclide was only possible by decoupling it from the remaining nuclides. Thus, only the masses of 20 nuclides comprised in two α decay chains were shifted by 8 keV, while the mass uncertainty of 84 nuclides was improved due to the remaining three mass measurements. Additionally, the influence of 45 connections among the nuclides were changed.
These measurements demonstrated that in the realm of the deformed shell closure at $N = 152$ the absolute masses of several nuclides have to be questioned and re-investigated. It is indicated by the existing mass data that the effect of the shell-closure is weaker for lower Z. For a detailed understanding of the Z-dependance new mass measurements in this region are necessary. It is planned that the deformed shell closure is mapped at TRIGA-TRAP for curium ($Z = 96$), berkelium ($Z = 97$) as well as californium ($Z = 99$), similar to the measurements performed for nobelium ($Z = 102$) and lawrencium ($Z = 103$), in order to address this question.
The main goal of the TRIGA-SPEC experiment is its coupling to the research reactor to measure the masses of neutron-rich nuclides, which can be used to test the predictive power of mass models used for r-process nucleosynthesis studies. The radionuclides, produced in thermal neutron-induced fission, are guided to a skimmer system on a high-voltage platform by an aerosol gas-jet, where the carrier gas is removed. The efficiency of this process is going to be improved by the use of an aerodynamic lens, where the aerosol particles are focused at the skimmer opening [Gru14]. The ions are then ionized in a hot surface ion source [Ren14], delivering radioactive alkali metal ions. This is going to be replaced in the future by a plasma ion source in order to access the entire spectrum of fission products [Sch15].
This is all part of a long-lasting preparation phase to develop techniques, which are going to be used at the FAIR facility. TRIGA-TRAP is embedded in the MATS experiment serving now as a test bench. Although the new facilities are supposed to provide ion beams with higher yields than at any other facility, especially techniques like the FT-ICR detection are desired to push the limit of well-known ions further towards the r-process path.

Bibliography

[Alt93] G. D. Alton, Ion sources for accelerators in materials research, *Nucl. Instr. Meth. B*, **73**, 221 (1993).

[And62] P. W. Anderson, Theory of Flux Creep in Hard Superconductors, *Phys. Rev. Lett.*, **9**, 309 (1962).

[Ast27] F. W. Aston, Bakerian Lecture: A new mass-Spectrograph and the whole number Rule, *Proc. R. Soc. Lond. A*, **115**, 487 (1927).

[Aud03] G. Audi, A. H. Wapstra, C. Thibault, The AME2003 Atomic Mass Evaluation (II). Tables, Graphs and References, *Nucl. Phys. A*, **729**, 337 (2003).

[Aud12a] G. Audi, *et al.*, The Nubase2012 evaluation of nuclear properties, *Chinese Phys C*, **36**, 1157 (2012).

[Aud12b] G. Audi, *et al.*, The Ame2012 atomic mass evaluation (I), *Chinese Phys C*, **36**, 1287 (2012).

[Bar57] J. Bardeen, L. N. Cooper, J. R. Schrieffer, Theory of Superconductivity, *Phys. Rev.*, **108**, 1175 (1957).

[Bar08] J. Barea, *et al.*, Garvey-Kelson relations and the new nuclear mass tables, *Phys. Rev. C*, **77**, 041304 (2008).

[Ben03] M. Bender, P.-H. Heenen, P.-G. Reinhard, Self-consistent mean-field models for nuclear structure, *Rev. Mod. Phys.*, **75**, 121 (2003).

[Ber02] I. Bergström, *et al.*, SMILETRAP: A Penning trap facility for precision mass measurements using highly charged ions, *Nucl. Instr. Meth. A*, **487**, 618 (2002).

[Bla02] K. Blaum, *et al.*, Carbon clusters for absolute mass measurements at ISOLTRAP, *Eur. Phys. J. A*, **15**, 245 (2002).

[Bla03a] K. Blaum, *et al.*, Masses of ^{32}Ar and ^{33}Ar for Fundamental Tests, *Phys. Rev. Lett.*, **91**, 260801 (2003).

[Bla03b] K. Blaum, *et al.*, Recent developments at ISOLTRAP: towards a relative mass accuracy of exotic nuclei below 10^{-8}, *J. Phys. B*, **36**, 921 (2003).

[Bla06] K. Blaum, High-accuracy mass spectrometry with stored ions, *Phys. Rep.*, **425**, 1 (2006).

[Blo10] M. Block, *et al.*, Direct mass measurements above uranium bridge the gap to the island of stability, *Nature*, **463**, 785 (2010).

[Boh39] N. Bohr, J. A. Wheeler, The mechanism of nuclear fission, *Phys. Rev.*, **56**, 426 (1939).

[Bol92a] G. Bollen, *et al.*, Resolution of nuclear ground and isomeric states by a Penning trap mass spectrometer, *Phys. Rev. C*, **46**, R2140 (1992).

[Bol92b] G. Bollen, *et al.*, Ramsey technique applied in a Penning trap mass spectrometer, *Nucl. Instr. Meth. B*, **70**, 490 (1992).

[Bol96] G. Bollen, *et al.*, ISOLTRAP: a tandem Penning trap system for accurate on-line mass determination of short-lived isotopes, *Nucl. Instr. Meth. A*, **368**, 675 (1996).

[Bro55] C. Browne, *et al.*, The decay chain ^{245}Pu - ^{245}Am - ^{245}Cm, *J. Inorg. Nucl. Chem.*, **1**, 254 (1955).

[Bro86] L. S. Brown, G. Gabrielse, Geonium theory: Physics of a single electron or ion in a Penning trap, *Rev. Mod. Phys.*, **58**, 233 (1986).

[Brü79] M. Brügger, *Ankopplung eines Gasjettransportsystems an einen Massenseparator und Abtrennung neutronenreicher Nuklide aus dem Spaltproduktgemisch*, Diploma thesis, Johannes Gutenberg-Universität Mainz (1979).

[Brü83] M. Brügger, *Entwicklung einer Hochtemperaturoberflächenionenquelle für den Heliumjet Massenseparator HELIOS und Zerfallsstudien an massengetrennten neutronenreichen Praseodymisotopen*, PhD thesis, Johannes Gutenberg-Universität Mainz (1983).

[Brü85] M. Brügger, *et al.*, Operation of a high temperature ion source at the helium-jet on-line isotope separator facility HELIOS, *Nucl. Instr. Meth. A*, **234**, 218 (1985).

[But03] H. Butt, K. Graf, M. Kappl, *Physics and chemistry of interfaces*, Wiley-Vch Weinheim (2003).

[Cam84] R. Campargue, Progress in overexpanded supersonic jets and skimmed molecular beams in free-jet zones of silence, *J. Phys. Chem. US*, **88**, 4466 (1984).

[Com74] M. B. Comisarow, A. G. Marshall, Fourier transform ion cyclotron resonance spectroscopy, *Chem. Phys. Lett.*, **25**, 282 (1974).

[Com78] M. B. Comisarow, Signal modeling for ion cyclotron resonance, *J. Chem. Phys.*, **69**, 4097 (1978).

[Dec80] J. Dechargé, D. Gogny, Hartree-Fock-Bogolyubov calculations with the $D1$ effective interaction on spherical nuclei, *Phys. Rev. C*, **21**, 1568 (1980).

[Deh90] H. Dehmelt, Experiments with an isolated subatomic particle at rest, *Rev. Mod. Phys.*, **62**, 525 (1990).

[Dil00] J. Dilling, *et al.*, The SHIPTRAP project: A capture and storage facility at GSI for heavy radionuclides from SHIP, *Hyperfine Interact.*, **127**, 491 (2000).

[Dob84] J. Dobaczewski, H. Flocard, J. Treiner, Hartree-Fock-Bogolyubov description of nuclei near the neutron-drip line, *Nucl. Phys. A*, **422**, 103 (1984).

[Duf94] J. Duflo, Phenomenological calculation for nuclear masses and charge radii, *Nucl. Phys. A*, **576**, 29 (1994).

[Duf95] J. Duflo, A. P. Zuker, Microscopic mass formulas, *Phys. Rev. C*, **52**, R23 (1995).

[Dwo09] M. Dworschak, *First direct mass measurements on nobelium and lawrencium with the Penning trap mass spectrometer SHIPTRAP*, PhD thesis, Johannes Gutenberg-Universität Mainz (2009).

[Dwo10] M. Dworschak, *et al.*, Penning trap mass measurements on nobelium isotopes, *Phys. Rev. C*, **81**, 064312 (2010).

[Ebe00] K. Eberhardt, A. Kronenberg, The research reactor TRIGA Mainz: A neutron source for versatile applications in research and education, *Kerntechnik*, **65**, 269 (2000).

[Eib09] M. Eibach, *Characterization of a carbon aerosol generator in a helium gas-jet for the extraction of fission products from the research reactor TRIGA Mainz*, Diploma thesis, Johannes Gutenberg-Universität Mainz (2009).

[Eib10a] M. Eibach, *et al.*, Transport of fission products with a helium gas-jet at TRIGA-SPEC, *Nucl. Instr. Meth. A*, **613**, 226 (2010).

[Eib10b] M. Eibach, *et al.*, First investigation of phase-shifted Ramsey excitation in Penning trap mass spectrometry, *Int. J. Mass Spectrom.*, **303**, 27 (2010).

[Eli11] S. Eliseev, *et al.*, Octupolar-Excitation Penning-Trap Mass Spectrometry for Q-Value Measurement of Double-Electron Capture in ^{164}Er, *Phys. Rev. Lett.*, **107**, 152501 (2011).

[Eng94] T. R. England, B. F. Rider. Evaluation and compilation of fission product yields 1993. Technical report, Los Alamos National Lab. (1994).

[Ero12] T. Eronen, *et al.*, JYFLTRAP: a Penning trap for precision mass spectroscopy and isobaric purification, *Eur. Phys. J. A*, **48**, 1 (2012).

[Fer07] R. Ferrer, *et al.*, Development of a Fourier-Transform Ion-Cyclotron-Resonance detection for short-lived radionuclides at SHIPTRAP, *Eur. Phys. J. Special Topics*, **150**, 347 (2007).

[Fin51] B. Finkle, *et al.*, *Radiochemical Studies: The fission products*, McGraw-Hill Book Company, Inc. (1951).

[Gab83] G. Gabrielse, Relaxation calculation of the electrostatic properties of compensated Penning traps with hyperbolic electrodes, *Phys. Rev. A*, **27**, 2277 (1983).

[Gab09] G. Gabrielse, The true cyclotron frequency for particles and ions in a Penning trap, *Int. J. Mass Spectrom.*, **279**, 107 (2009).

[Gar66] G. T. Garvey, I. Kelson, New Nuclidic Mass Relationship, *Phys. Rev. Lett.*, **16**, 197 (1966).

[Gar69] G. T. Garvey, Nuclear Mass Relations, *Annu. Rev. Nucl. Sci.*, **19**, 433 (1969).

[Geo07] S. George, *et al.*, The Ramsey method in high-precision mass spectrometry with Penning traps: Experimental results, *Int. J. Mass Spectrom.*, **264**, 110 (2007).

[Ger90] C. Gerz, D. Wilsdorf, G. Werth, Measurement of the ^{4}He-D_2 mass difference, *Z. Phys. D*, **17**, 119 (1990).

[Gor00] S. Goriely, Nuclear inputs for astrophysics applications, *AIP Conference Proceedings*, **529**, 287 (2000).

[Gor10] S. Goriely, N. Chamel, J. M. Pearson, Further explorations of Skyrme-Hartree-Fock-Bogoliubov mass formulas. XII. Stiffness and stability of neutron-star matter, *Phys. Rev. C*, **82**, 035804 (2010).

[Gor13] S. Goriely, N. Chamel, J. M. Pearson, Further explorations of Skyrme-Hartree-Fock-Bogoliubov mass formulas. XIII. The 2012 atomic mass evaluation and the symmetry coefficient, *Phys. Rev. C*, **88**, 024308 (2013).

[Grä80] G. Gräff, H. Kalinowsky, J. Traut, A direct determination of the proton electron mass ratio, *Z. Phys. A*, **297**, 35 (1980).

[Gro91] P. B. Grosshans, P. J. Shields, A. G. Marshall, Comprehensive theory of the Fourier transform ion cyclotron resonance signal for all ion trap geometries, *J. Chem. Phys.*, **94**, 5341 (1991).

[Gru14] J. Grund, *Entwicklung einer aerodynamischen Linse für TRIGA-SPEC*, Diploma thesis, Johannes Gutenberg-Universität Mainz, to be published (2014).

[Gün93] R. Günther, *Charakterisierung der Eigenschaften der KCl-Aerosolpartikel eines He-Gasjets*, Diploma thesis, Johannes Gutenberg-Universität Mainz (1993).

[Ham06] G. Hampel, K. Eberhardt, N. Trautmann, The research reactor TRIGA Mainz, *ATW-Int. Z. Kernenergie*, **51**, 328 (2006).

[He13] Z. He, *et al.*, New features of the Garvey-Kelson mass relations, *Phys. Rev. C*, **87**, 057304 (2013).

[Her03] F. Herfurth, Segmented linear RFQ traps for nuclear physics, *Nucl. Instr. Meth. B*, **204**, 587 (2003).

[Jän88] J. Jänecke, P. Masson, Mass predictions from the Garvey-Kelson mass relations, *Atom. Data Nucl. Data*, **39**, 265 (1988).

[Joh28] J. B. Johnson, Thermal Agitation of Electricity in Conductors, *Phys. Rev.*, **32**, 97 (1928).

[Kel03] A. Kellerbauer, *et al.*, From direct to absolute mass measurements: A study of the accuracy of ISOLTRAP, *Eur. Phys. J. D*, **22**, 53 (2003).

[Ket06] J. Ketelaer, *Developement of a non-destructive Fourier Transform-Ion Cyclotron Resonance detection system for singly charged ions in a cryogenic Penning trap*, Master's thesis, Johannes Gutenberg-Universität Mainz (2006).

[Ket08] J. Ketelaer, *et al.*, TRIGA-SPEC: A setup for mass spectrometry and laser spectroscopy at the research reactor TRIGA Mainz, *Nucl. Instr. Meth. A*, **594**, 162 (2008).

[Ket09a] J. Ketelaer, *et al.*, Recent developments in ion detection techniques for Penning trap mass spectrometry at TRIGA-TRAP, *Eur. Phys. J. A*, **42**, 311 (2009).

[Ket09b] J. Ketter, *Verbesserungen der Ionennachweissysteme des Präzisions-Penningfallen-Massenspektrometers TRIGA-TRAP*, Diploma thesis, Johannes Gutenberg-Universität Mainz (2009).

[Ket10a] J. Ketelaer, *The construction of TRIGA-TRAP and direct high-precision Penning trap mass measurements on rare-earth elements and americium*, PhD thesis, Johannes Gutenberg-Universität (2010).

[Ket10b] J. Ketelaer, *et al.*, Accuracy studies with carbon clusters at the Penning trap mass spectrometer TRIGA-TRAP, *Eur. Phys. J. D*, **58**, 47 (2010).

[Ket14] J. Ketter, PhD thesis, Ruprecht-Karls-Universität Heidelberg, to be published (2014).

[Klu03] H.-J. Kluge, W. Nörtershäuser, Lasers for nuclear physics, *Spectrochim. Acta B*, **58**, 1031 (2003).

[Knu09] K. Knuth, *Aufbau eines breitbandigen FT-ICR-Nachweissystems für TRIGA-TRAP*, Diploma thesis, Johannes Gutenberg-Universität Mainz (2009).

[Kol08] V. Kolhinen, *et al.*, MLLTRAP: A Penning trap facility for high-accuracy mass measurements, *Nucl. Instr. Meth. B*, **266**, 4547 (2008).

[Kön95] M. König, *et al.*, Quadrupole excitation of stored ion motion at the true cyclotron frequency, *Int. J. Mass Spectrom. Ion Processes*, **142**, 95 (1995).

[Kra07] H. Kracke, *Entwicklung der kryogenen Nachweis-Elektronik zur Bestimmung der axialen Frequenz des Protons in einer Penning-Falle*, Diploma thesis, Johannes Gutenber-Universität Mainz (2007).

[Kra12] H. Kracke, *Detection of individual spin transitions of a single proton confined in a cryogenic Penning trap*, PhD thesis, Johannes Gutenber-Universität Mainz (2012).

[Kre91] M. Kretzschmar, Particle motion in a Penning trap, *Eur. J. Phys.*, **12**, 240 (1991).

[Kre92] M. Kretzschmar, Single particle motion in a Penning trap: description in the classical canonical formalism, *Phys. Scripta*, **46**, 544 (1992).

[Kre07] M. Kretzschmar, The Ramsey method in high-precision mass spectrometry with Penning traps: Theoretical foundations, *Int. J. Mass Spectrom.*, **264**, 122 (2007).

[Kre08a] M. Kretzschmar, Calculating damping effects for the ion motion in a Penning trap, *Eur. Phys. J. D*, **48**, 313 (2008).

[Kre08b] M. Kretzschmar, Theory of the elliptical Penning trap, *Int. J. Mass Spectrom.*, **275**, 21 (2008).

[Lan25] I. Langmuir, K. H. Kingdon, Thermionic Effects Caused by Vapours of Alkali Metals, *Proc. R. Soc. Lond. A.*, **107**, 61 (1925).

[LBN] LBNL, http://ie.lbl.gov/fission.html.

[Lin91] M. Lindinger, *et al.*, Cluster isobars for high-precision mass spectrometry, *Z. Phys. D.*, **20**, 441 (1991).

[Liu95a] P. Liu, *et al.*, Generating Particle Beams of Controlled Dimensions and Divergence: I. Theory of Particle Motion in Aerodynamic Lenses and Nozzle Expansions, *Aerosol Sci. Technol.*, **22**, 293 (1995).

[Liu95b] P. Liu, *et al.*, Generating Particle Beams of Controlled Dimensions and Divergence: II. Experimental Evaluation of Particle Motion in Aerodynamic Lenses and Nozzle Expansions, *Aerosol Sci. Technol.*, **22**, 314 (1995).

[Lun03] D. Lunney, J. M. Pearson, C. Thibault, Recent trends in the determination of nuclear masses, *Rev. Mod. Phys.*, **75**, 1021 (2003).

[Lun09] D. Lunney, *et al.*, COLETTE: A linear Paul-trap beam cooler for the on-line mass spectrometer MISTRAL, *Nucl. Instr. Meth. A*, **598**, 379 (2009).

[Mac59] W. W. Macalpine, R. O. Schildknecht, Coaxial Resonators with Helical Inner Conductor, *Proceedings of the IRE*, **47**, 2099 (1959).

[Mac69] R. D. Macfarlane, *et al.*, The helium-jet recoil transport method, *Nucl. Instr. Meth.*, **73**, 285 (1969).

[Maj05] F. Major, V. Gheorghe, G. Werth, *Charged Particle Traps*, Springer (2005).

[Mak07] H. Makii, *et al.*, Z dependence of the $N = 152$ deformed shell gap: In-beam γ-ray spectroscopy of neutron-rich ^{245,246}Pu, *Phys. Rev. C*, **76**, 061301 (2007).

[Mar69] P. Marinos, Fuzzy Logic and its Application to Switching Systems, *IEEE Trans. Comput.*, **18**, 343 (1969).

[Maz80] A. Mazumdar, *et al.*, The on-line isotope separation facility HELIOS at the Mainz reactor, *Nucl. Instr. Meth.*, **174**, 183 (1980).

[Men08] J. Mendoza-Temis, *et al.*, Testing the predictive power of nuclear mass models, *Nucl. Phys. A*, **812**, 28 (2008).

[Möl81] P. Möller, J. Nix, Nuclear mass formula with a Yukawa-plus-exponential macroscopic model and a folded-Yukawa single-particle potential, *Nucl. Phys. A*, **361**, 117 (1981).

[Möl88] P. Möller, J. Nix, Nuclear masses from a unified macroscopic-microscopic model, *Atom. Data Nucl. Data*, **39**, 213 (1988).

[Möl94] P. Möller, J. R. Nix, Stability of heavy and superheavy elements, *J. Phys. G*, **20**, 1681 (1994).

[Möl95] P. Möller, *et al.*, Nuclear Ground-State Masses and Deformations, *Atom. Data Nucl. Data*, **59**, 185 (1995).

[Möl12] P. Möller, *et al.*, New Finite-Range Droplet Mass Model and Equation-of-State Parameters, *Phys. Rev. Lett.*, **108**, 052501 (2012).

[Mye66] W. D. Myers, W. J. Swiatecki, Nuclear masses and deformations, *Nucl. Phys.*, **81**, 1 (1966).

[Mye69] W. D. Myers, W. J. Swiatecki, Average nuclear properties, *Ann. Phys.*, **55**, 395 (1969).

[Mye74] W. D. Myers, W. J. Swiatecki, The nuclear droplet model for arbitrary shapes, *Ann. Phys.*, **84**, 186 (1974).

[Nav00] P. Navrátil, J. P. Vary, B. R. Barrett, Properties of ^{12}C in the *Ab Initio* Nuclear Shell Model, *Phys. Rev. Lett.*, **84**, 5728 (2000).

[Nei08] D. Neidherr, *et al.*, Measurement and simulation of the pressure ratio between the two traps of double Penning trap mass spectrometers, *Nucl. Instr. Meth. B*, **266**, 4556 (2008).

[New61] H. W. Newson, Symmetric and Asymmetric Fission, *Phys. Rev.*, **122**, 1224 (1961).

[Nyq28] H. Nyquist, Thermal Agitation of Electric Charge in Conductors, *Phys. Rev.*, **32**, 110 (1928).

[Oga12] Y. T. Oganessian, *et al.*, Production and Decay of the Heaviest Nuclei ^{293,294}117 and ^{294}118, *Phys. Rev. Lett.*, **109**, 162501 (2012).

[Ott89] E. Otten, *Nuclear radii and moments of unstable isotopes*, Springer, New York (1989).

[Pau90] W. Paul, Electromagnetic traps for charged and neutral particles, *Rev. Mod. Phys.*, **62**, 531 (1990).

[Pen36] F. Penning, Die Glimmentladung bei niedrigem Druck zwischen koaxialen Zylindern in einem axialen Magnetfeld, *Physica*, **3**, 873 (1936).

[Pfe11] B. Pfeiffer, private communications (2011).

[Pie49] J. R. Pierce, *Theory and design of electron beams*, Van Nostrand Co. (1949).

[Pie10] J. Piekarewicz, *et al.*, Garvey-Kelson relations for nuclear charge radii, *Eur. Phys. J. A*, **46**, 379 (2010).

[Por01] J. V. Porto, Series solution for the image charge fields in arbitrary cylindrically symmetric Penning traps, *Phys. Rev. A*, **64**, 023403 (2001).

[Ram12] E. M. Ramirez, *et al.*, Direct Mapping of Nuclear Shell Effects in the Heaviest Elements, *Science*, **337**, 1207 (2012).

[Ren12] D. Renisch, *et al.*, Targets on superhydrophobic surfaces for laser ablation ion sources, *Nucl. Instr. Meth. A*, **676**, 84 (2012).

[Ren14] D. Renisch, *Developing of a high-temperature surface ion source for online coupling of TRIGA-SPEC to the TRIGA Mainz research reactor*, PhD thesis, Johannes Gutenberg-Universität Mainz, to be published (2014).

[Rep08] J. Repp, *Setup of a non-destructive ion detection system and magnetic field investigations for precision mass measurements at TRIGA-TRAP*, Diploma thesis, Johannes Gutenberg-Universität Mainz (2008).

[Rin07] R. Ringle, *et al.*, Octupolar excitation of ion motion in a Penning trap - A study performed at LEBIT, *Int. J. Mass Spectrom.*, **262**, 33 (2007).

[Rod10] D. Rodriguez, *et al.*, MATS and LaSpec: High-precision experiments using ion traps and lasers at FAIR, *Eur. Phys. J. Special Topics*, **183**, 1 (2010).

[Sav91] G. Savard, *et al.*, A new cooling technique for heavy ions in a Penning trap, *Phys. Lett. A*, **158**, 247 (1991).

[Sch15] F. Schneider, *Aufbau einer Resonanzionisationsquelle am Forschungsreaktor TRIGA Mainz*, PhD thesis, Johannes Gutenber-Universität Mainz, to be published (2015).

[Sco89] G. Scoles, *et al.*, *Atomic and Molecular Beam Methods, Vol. I*, Oxford University Press, Oxford (1989).

[Smo08] C. Smorra, *Setup of a carbon-cluster laser ion source for high-precision mass spectrometry*, Diploma thesis, Johannes Gutenberg-Universität Mainz (2008).

[Smo09] C. Smorra, *et al.*, A Carbon cluster laser ion source for TRIGA-TRAP, *J. Phys. B*, **42**, 154028 (2009).

[Smo12] C. Smorra, *High-precision Q-value and mass measurements for neutrino physics with TRIGA-TRAP and commissioning of an on-line ion source for TRIGA-SPEC*, PhD thesis, Ruprecht-Karls-Universität Heidelberg (2012).

[Str67] V. M. Strutinsky, Shell effects in nuclear masses and deformation energies, *Nucl. Phys. A*, **95**, 420 (1967).

[Str68] V. M. Strutinsky, Shells in deformed nuclei, *Nucl. Phys. A*, **122**, 1 (1968).

[Stu11] S. Sturm, *The g-factor of the electron bound in $^{28}Si^{13+}$: The most stringent test of bound-state quantum electrodynamics*, PhD thesis, Johannes Gutenberg-Universität (2011).

[Stu13] S. Sturm, *et al.*, *g*-factor measurement of hydrogenlike $^{28}Si^{13+}$ as a challenge to QED calculations, *Phys. Rev. A*, **87**, 030501 (2013).

[Tho13] J. J. Thomson, Bakerian Lecture: Rays of Positive Electricity, *Proc. R. Soc. Lond. A*, **89**, 1 (1913).

[Van89] R. S. Van Dyck, *et al.*, Number dependency in the compensated Penning trap, *Phys. Rev. A*, **40**, 6308 (1989).

[Vau72] D. Vautherin, D. M. Brink, Hartree-Fock Calculations with Skyrme's Interaction. I. Spherical Nuclei, *Phys. Rev. C*, **5**, 626 (1972).

[Vau73] D. Vautherin, Hartree-Fock Calculations with Skyrme's Interaction. II. Axially Deformed Nuclei, *Phys. Rev. C*, **7**, 296 (1973).

[Vie13] J. Vieten, *Präzisionsstudien des TRIGA-TRAP-Massenspektrometers durch Einsatz von Kohlenstoffclusterionen als Referenz*, Bachelor Thesis, Technische Universität München (2013).

[Wag12] A. Wagner, *Measurement of the g-factor of Li-like silicium*, PhD thesis, Ruprecht-Karls-Universität Heidelberg (2012).

[Wan12] M. Wang, *et al.*, The AME2012 atomic mass evaluation (II), *Chinese Phys C*, **36**, 1603 (2012).

[Wan13] M. Wang, private communications (2013).

[Web04] C. Weber, *Konzeption eines kryogenen Penningfallenaufbaus für SHIPTRAP und Massenbestimmungen von Radionukliden um den Z=82 - Schalenabschluss an ISOLTRAP*, PhD thesis, Ruprecht-Karls Universität Heidelberg (2004).

[Wei35] C. F. Weizsäcker, Zur Theorie der Kernmassen, *Z. Phys. A*, **96**, 431 (1935).

[Wei59] S. Weinberg, S. B. Treiman, Electromagnetic Corrections to Isotopic Spin Conservation, *Phys. Rev.*, **116**, 465 (1959).

[Xia93] X. Xiang, P. B. Grosshans, A. G. Marshall, Image charge-induced ion cyclotron orbital frequency shift for orthorhombic and cylindrical FT-ICR ion traps, *Int. J. Mass Spectrom.*, **125**, 33 (1993).

[Zud86] F. Zude, *Transportverhalten von Spaltprodukten in Gasjetsystemen*, Diploma thesis, Johannes Gutenberg-Universität Mainz (1986).

[Zuk94] A. P. Zuker, On the microscopic derivation of a mass formula, *Nucl. Phys. A*, **576**, 65 (1994).

[Zuk08] A. Zuker, Shell formation and nuclear masses, *Revista mexicana de fisica*, **54**, 129 (2008).

Acknowledgements

At this point I would like to thank all the people that supported me in the last four years work-related or private.
First I thank my supervisor Klaus Blaum giving me the opportunity to do research in his group. He already piqued my interest in Penning trap physics during his lectures years ago making the research in this field very interesting. I appreciate that he always supported me, whenever it was necessary but also let me find my own solutions. I am in particular thankful for the opportunities to represent TRIGA-TRAP on conferences.

I am also grateful to Yuri Litvinov for agreeing to be the second referee of my thesis and to Joerg Jaeckel and Wolfgang Schlegel for completing the examination committee.

I also thank all the members of the TRIGA-TRAP team for being an incredible support during the last years. Without them, my thesis would not have reached this successful end. Moreover, they became my friends in this time. These are especially Szilard Nagy, Jens Ketelaer, Christian Smorra, Thomas Beyer, Dennis Neidherr, Dennis Renisch, Fabian Schneider, Sebastian Klein and Jessica Grund. I also thank the entire TRIGA-SPEC collaboration supporting me with helpful discussions: Klaus Eberhardt, Norbert Wiehl, Chistoph Düllmann and Norbert Trautmann from the Nuclear Chemistry, Wilfried Nörtershäuser, Christopher Geppert, Andreas Krieger, Jörg Krämer, Michael Hammen, Simon Kaufmann, Christian Gorges, Elisa Will, and Nadia Frömmgen from the TRIGA-LASER experiment and Michael Block from GSI.

For the help with the FT-ICR system, in particular the cryogenic electronics I thank Stefan Ulmer, Sven Sturm and Jochen Ketter.
I am also indebted to Jens Ketelaer and Fabio Schwellnus for designing the ion source upgrade and for Klaus Wendt that he pushed the machining process in the physics workshop.

I thank in particular Jörg Runke and Christoph Mokry from the Nuclear Chemistry Institute for the chemical preparation of the different isotopes and for their help in the target production and of course, the staff of my home institute for always supporting me, when it was needed.

I am grateful to Meng Wang and Georges Audi for including my mass measurement data

into the Atomic-Mass Evaluation and for the great discussions during that time.

Thank you, also to Jens Dilling for letting me join his Penning trap experiment in Vancouver for three months and to all members of the TITAN group for making my stay extraordinary enjoyable.

Zu guter Letzt danke ich meinen Eltern und meinem Bruder, die mich immer unterstützt haben und natürlich auch bei meinen Verwandten und Freunden, die mich auch immer wieder inspirierten. Vor allem aber danke ich meiner Freundin Jennifer, die immer für mich da war, dass sie mich immer wieder aufgebaut hat, wenn es im Labor mal nicht gut lief, und verständnisvoll war, wenn die Arbeitstage mal wieder etwas länger waren.

Erklärung

Hiermit erkläre ich, Martin Eibach, dass ich diese Arbeit selbst verfasst habe und ausschließlich die angegebenen Quellen verwendet habe.

Heidelberg, den 23.09.2013

Martin Eibach